15

Spectroscopic Studies of Magnetic Cataclysmic Variables

by

Kurt Josias van der Heyden

Preface

In this thesis I present the results of optical spectroscopic analyses of four Polars and the spectra of five new systems. The results of four candidate magnetic cataclysmic variables, which were selected from the ROSAT Bright Survey, are also presented. Time resolved spectra are used for the dual purpose of conducting Doppler tomographical studies and searching for any evidence of cyclotron beaming. The first five chapters are introductory and background sections, including a review of all individual objects with magnetic field strengths determined by cyclotron spectroscopy. In Chapter 6 I discuss the observations, data reduction and analysis techniques while the results of individual objects are presented in Chapter 7. Results are presented for the two Polars HU Aqr and QS Tel, which were selected as test objects to confirm the techniques of Doppler tomography and cyclotron spectroscopy, respectively. Doppler maps, similar to those previously obtained, are produced for HU Aqr. Two cyclotron humps are also detected in the HU Aqr spectra corresponding to a magnetic field of 39 MG, again similar to values quoted in the literature. A complex cyclotron spectrum for QS Tel indicates that the second magnetic pole is more dominant than in previous studies. Spectra are presented for the new Polars RX J1313-32, RX J1141-64, RX J1610+03, RX J0153-59, RX J0501-03, RX J0512-72 and RX J0515+01. More extensive observations were made for RX J1313-32 and RX J1141-64, with Doppler maps derived for RX J1313-32 while the RX J1141-64 spectra show a rise in the spectral slope, indicative of cyclotron radiation. Four ROSAT Bright Survey sources, RBS 0324, RBS 0372, RBS 0490 & RBS 1969, were selected to search for any evidence of them being magnetic cataclysmic variables. More detailed spectroscopy and photometry was obtained for RBS 0324, the only RBS source which shows evidence of being a magnetic system. The other RBS systems are all probably dwarf novae in quiescence.

Acknowledgements

To my parents, whose teachings I'm only beginning to appreciate. And to the many who lost their lives in the pursuit of freedom in this country, without whose efforts I would not have been given the opportunity to even attempt this thesis.

Contents

List of Figures

v

vii

List of Tables

Chapter 1

Introduction

Cataclysmic variables are a class of semi-detached binary stars containing a mass-losing secondary star, usually a late type main sequence star, and a white dwarf as a compact primary star. Here 'primary' refers to the more massive star while the 'secondary' is the less massive star. The progenitors of cataclysmic variables are wide binaries with large orbital periods ($P_{orb} \geq 10$ d) consisting of a low-mass main sequence star and a more massive primary with $M_{prim} \simeq 1 - 10 M_\odot$. The massive primary evolves on its nuclear timescale into a giant and eventually fills its critical gravitational equipotential surface, known as the Roche-lobe surface, starting a dynamically unstable mass transfer which results in a common envelope, engulfing both stars. During that phase the binary system loses angular momentum due to frictional braking in the common envelope, reducing the distance between the two stars and ejecting the envelope of the giant from the system.

If the core of the giant (the future white dwarf) and the low-mass main sequence secondary do not merge during this process, a detached close binary emerges. In order to become a cataclysmic variable, the system has to further shrink in its orbit until the secondary fills its Roche-lobe surface, at which point it starts to lose mass to the white dwarf primary through the inner Lagrangian point (L_1). The conservation of angular momentum prevents the matter from falling directly onto the white dwarf surface. Instead the gas stream swings around the white dwarf, eventually intersecting itself, forming a ring of material with the same specific angular momentum that the gas had at the L_1 point. Viscous interactions in the accretion ring causes angular momentum to be transfered between gas orbiting at slightly different radii. This causes the ring to spread both outwards and inwards and results in a thin accretion disc forming around the white dwarf.

Cataclysmic variables are divided into several subgroups determined by critical parameters like period, mass and mass transfer rate. Among these are the magnetic cataclysmic variables (mCVs). Magnetic CVs are further divided into two classes: Polars (AM Herculis systems) and Intermediate Polars (IPs), also sometimes called DQ Herculis stars (Patterson 1994). In the former the spin of the white dwarf is synchronized, or very nearly so, to the orbital period of the system. In Polars the magnetic field (10 - 200 MG; Cropper 1990) of the white dwarf primary is sufficiently strong to prevent disc formation. As the material falls toward the white dwarf, it eventually encounters a magnetic density ($B^2/8\pi$) that locally exceeds the kinetic energy density (ρv^2) and the accreted material is forced to follow the field lines. The location where this energy exchange occurs is called the coupling region. The in-falling matter experiences an increasingly strong field as it is

accelerated down the accretion column, and eventually passes through a standing shock front which reduces the velocity from a supersonic to sub-sonic flow by a factor of four. In the post-shock region electrons spiral around the magnetic field lines, emitting highly polarized cyclotron radiation over a range of harmonics. Hard X-rays (typically $kT \sim 30$ keV), produced by thermal bremsstrahlung, are emitted further down in the post-shock region, but most of the X-rays are thermalised by the white dwarf photosphere and re-emitted as a pseudo-blackbody soft X-ray component ($kT_{bb} \sim 40$ eV) (Wickramasinghe 1988).

Intermediate Polars (IPs) generally have weaker fields and thus only the inner regions of the accretion disc are disrupted. IPs accrete via an accretion curtain as opposed to an accretion column as in Polars. This is because the gas is accreted from within the inner radius of the disc. IPs are also strong sources of hard X-rays, and the white dwarfs spin is not synchronized to the orbital period.

Magnetic cataclysmic variables are observationally interesting for a number of reasons. Their short orbital and spin periods, often manifested as multi-periodic variability, makes them ideal targets for time series studies. Much can be learned from studies using various observational disciplines: high-speed photometry, time resolved spectroscopy, polarimetry and X-ray photometry are the prime areas of investigation.

The ROSAT All-Sky Survey (RASS) presented a breakthrough for studies of magnetic CVs. Several dozen new Polars were identified in recent years as optical counterparts of bright soft X-ray/EUV emitters, most of them from X-ray sources found in the RASS. A total of about 60 Polars are known, more than three times the number of sources from the pre-ROSAT era (Schwope, Schwarz, & Greiner 1999). New interesting individual systems have emerged and systematic studies became possible concerning e.g. the period and magnetic field distribution.

For a completely different purpose other than to search for new CVs, namely to determine the X-ray luminosity function of X-ray emitting extragalactic sources, a major program of optical identifications of bright, high-galactic-latitude ($> 30°$) X-ray sources, termed the ROSAT Bright Survey (RBS), was started (e.g. Fischer et al. 1998). As a by-product of this a number of CVs were also recently found. These CVs are most probably magnetic in nature, since they show the typical high-excitation emission line spectrum and they are X-ray sources.

This thesis involves spectroscopic studies of magnetic CVs. It has the dual aims of investigating the velocity structures of the accreting gas and the presence of cyclotron beaming. This program is a new one to SAAO, which utilizes, for the first time, the enhanced red performance of the *SITe* CCD detector on the Cassegrain spectrograph. The improved sensitivity aids in the detection of red/near-IR cyclotron emission 'humps', as well as providing the additional capability of studying secondary star spectra, when they are present.

Recent developments in the field of Doppler tomographic imaging (Horne 1991) have led to the application of the method in the disc-less magnetic CVs, and in particular the synchronized Polars . With good phase coverage ($\Delta\phi \leq 0.025$) and high signal-to-noise spectra (S/N ≥ 50), it is possible to map the various velocity components of the emission lines onto a velocity 'image' of the binary system (e.g. Marsh & Horne 1988). This allows components like the accretion stream, secondary star and stream-magnetosphere coupling regions to be explicitly imaged.

In this project time resolved spectra of mCVs were utilized to provide data for tomo-

graphic analysis. Spectroscopic observations were obtained of two known Polars, HU Aqr and QS Tel. Observations of the recently discovered mCVs RX J1313-32, RX J1141-64, RX J1610+03, RX J0153-59, RX J0501-03, RX J0512-72 and RX J0515+01 are presented, with more detailed analyses given for RX J1313-32 and RX J1141-64. Four ROSAT Bright Survey sources, RBS 0324, RBS 0372, RBS 0490 and RBS 1969 were selected to search for any evidence of them being mCVs.

The advent of the *SITe* CCD detector on the Cassegrain spectrograph of the SAAO made it possible to attempt both wide-slit spectrophotometric observations, and observations at longer wavelengths (up to 9000 Å). This latter capability is important in studies of the secondaries and to investigate the presence of cyclotron beaming, which is the other aim of the program. Cyclotron lines provide a very sensitive method for the measurement of magnetic fields in mCVs. Through determining their positions, which often shift over the binary/spin period, it is possible to unambiguously determine magnetic field strengths and topologies, sometimes of both magnetic poles.

Chapter 2

The Magnetic Field

The accreted material in mCVs is partially ionized gas, i.e. a plasma of freely moving ions and electrons. Because the plasma consists of charged particles, its motion and physical state is strongly influenced by the presence of magnetic and electric fields. The strong magnetic fields in mCVs thus ensure a strong coupling of electromagnetic phenomena and fluid motions. Due to the lower magnetic field strength in IPs ($B{\sim}0.01 - 1{\times}10^7$ G; Patterson 1994), the magnetic field is not as easily detected as in the higher field strength present in Polars. For this reason my discussion concentrates on magnetic fields observable in Polars.

The extreme conditions in the accretion columns ($T \sim 10^8$ K and $B \sim 10^7 - 10^8$ G; Burwitz 1997) make Polars ideal plasma laboratories in which magnetohydrodynamical problems and radiation processes can be studied. Understanding these processes in mCVs assists in the general studies of plasma interactions with magnetic fields and consequent radiation processes.

2.1 Field Measurement

Tapia (1977) found both linear and circular polarization variations at optical wavelengths over the orbital cycle in AM Her, and thus concluded that the major source of optical emission was cyclotron radiation. Tapia (1977) reasoned, incorrectly, that for cyclotron radiation to be polarized in the optical, field strengths of the order $\sim 10^8$ G are required. This was because Tapia was not aware that the observed cyclotron radiation was emitted at the harmonics of the fundamental cyclotron frequency. His high field strength thus corresponded to the fundamental harmonic, and not the higher harmonics which are present in the optical/near IR. Subsequent investigations, where harmonics were identified, indicated field strengths of the order $\sim 10^7$ G (Cropper 1990). The strength of the magnetic field is one of the single most important parameters of a mCV. Determining the magnetic field characteristics has become a major goal and this has led to the development of more accurate techniques. These techniques are summarized in the following sections.

2.1.1 Zeeman Splitting

When the accretion rate in a Polar is low (i.e. a photometric 'low state') the photospheres of the two component stars are the major source of light from the system. During such
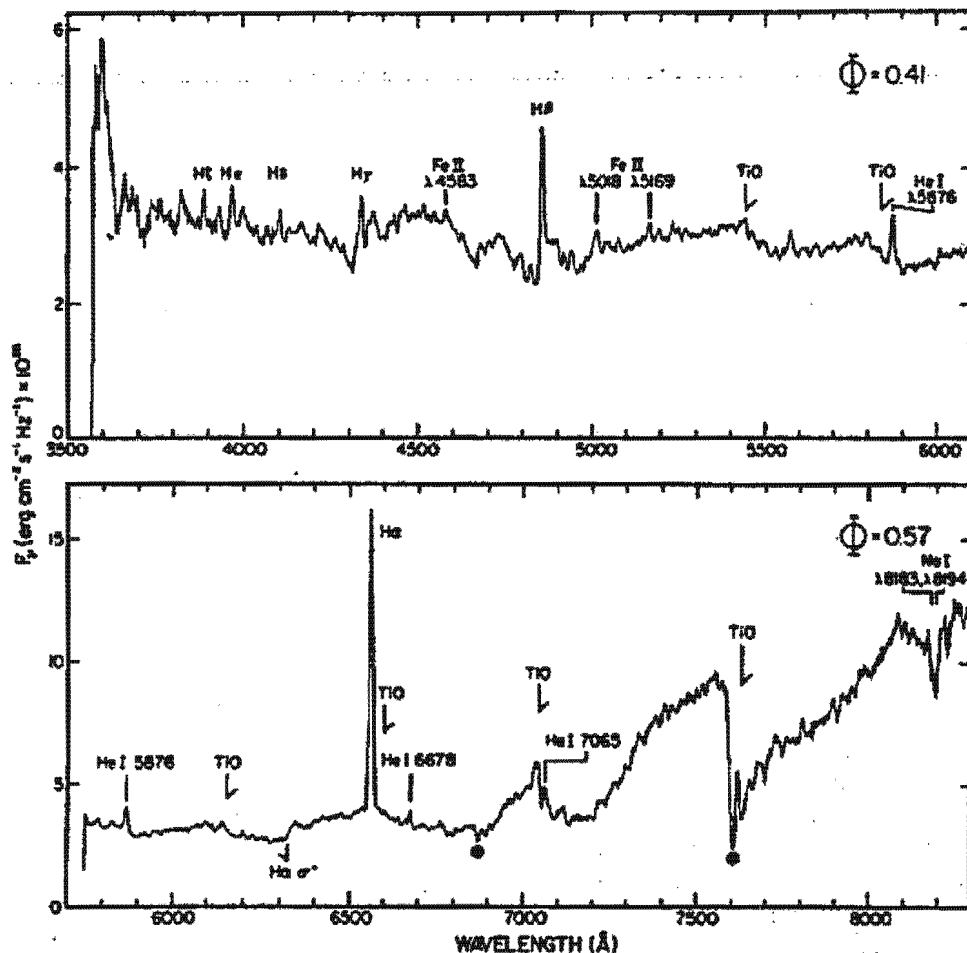
Figure 2.1: Spectra of AM Her in the low state showing Zeeman absorption features in the Balmer lines at the blue wavelengths and TiO absorptions in the red (Schmidt, Stockman, & Margon 1981).

a low state the Zeeman split spectral lines of the white dwarf can be observed directly, with some of the components separated by as much as a few hundred Ångstroms.

If one observes along magnetic lines (the longitudinal case), a spectral line is split into two components, σ_- and σ_+. The wavelength of σ_- is shortward (i.e. blue-shifted) of the original line λ_0, while that of σ_+ is longward (i.e. red-shifted) of λ_0. The wavelength shift with respect to λ_0 is $\Delta\lambda_B$, which is the magnitude of the Zeeman splitting. $\Delta\lambda_B$ is given by

$$\Delta\lambda_B = \frac{eB\lambda^2}{4\pi m_e c^2}. \tag{2.1}$$

When observed in a direction perpendicular to the magnetic field lines, a spectral line is split into three components (Shi-hui 1994). The central component (π) has its wavelength at that of original wavelength, λ_0, and the other two are at: $\lambda_0 \pm \Delta\lambda_B$. The π and σ components also have quite specific polarization properties. If the magnetic field is transverse to the line of sight of the observer, the π components (in emission) are linearly polarized parallel to the applied field, while the σ components are linearly polarized perpendicular to the field. If the magnetic field is parallel to the line of sight, the π components are not visible, and the two sets of σ components have opposite circular

5
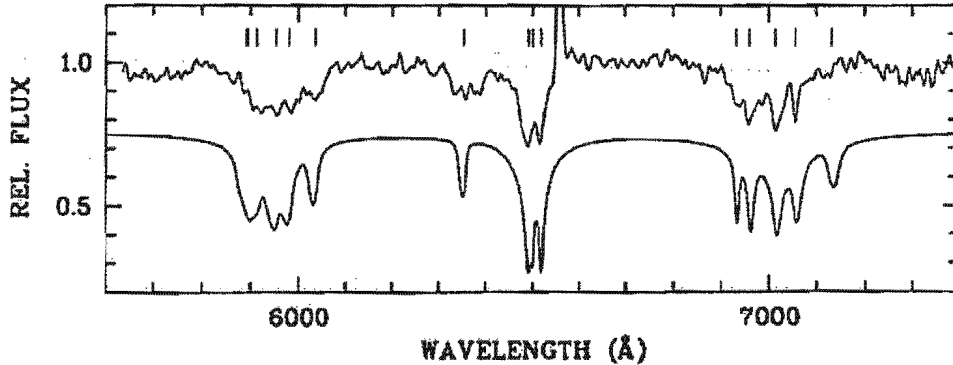
Figure 2.2: Normalized photospheric Zeeman spectrum of the white dwarf in MR Ser showing the structured Hα Zeeman triplet. The lower spectrum is a synthetic model spectrum (Schwope 1995).

polarizations (Landstreet 1992). Fig. 2.1 & 2.2 shows the Zeeman splitting in AM Her and MR Ser respectively.

Using Zeeman splitting to determine the magnetic field has two inherent difficulties. The first is that the system has to be in a low accretion state for observations to be possible, unless the geometry of the system is such that the main accreting pole is not visible and the accretion rate at the secondary pole is negligible (e.g. as in ST LMi). Scheduling of such observations is difficult because low states cannot be predicted and because telescopes of large aperture are required to obtain spectra with good signal-to-noise ratio. The second problem is that the measured Zeeman spectrum is a flux-weighted mean over the observable photosphere and thus assumptions have to be made about the field configuration and flux distribution over the photosphere in order to obtain the field in the accretion region. The field is often assumed to be dipolar, but evidence suggests that the field configuration might be more complicated (i.e. multi-polar; Wu & Wickramasinghe 1993). The field configuration is discussed in more detail in Section 2.2.

2.1.2 Cyclotron Harmonics

The optical continua of Polars in their high accretion states are often dominated by the strong cyclotron sources at the footprints of accreting field lines, in the post-shock region of the accretion stream. The ionized plasma is forced to emit electromagnetic radiation at the cyclotron fundamental and its harmonics. Resolvable cyclotron harmonics lie in the optical window between 3500 and 10000 Å (Wickramasinghe 1988). The cyclotron emission appears as broad humps in the spectra, as seen in Fig. 2.3. The magnetic field strength can be estimated from the spacings of the cyclotron humps. At non-relativistic energies the harmonics are equally spaced. In Polars the electron energies are mildly relativistic, in the range ~ 1 keV to several hundred keV (Bekefi 1966). The spacing of the humps depends not only on the magnetic field strength, but also on other parameters such as temperature and geometry of the magnetic field. The field strength, along with
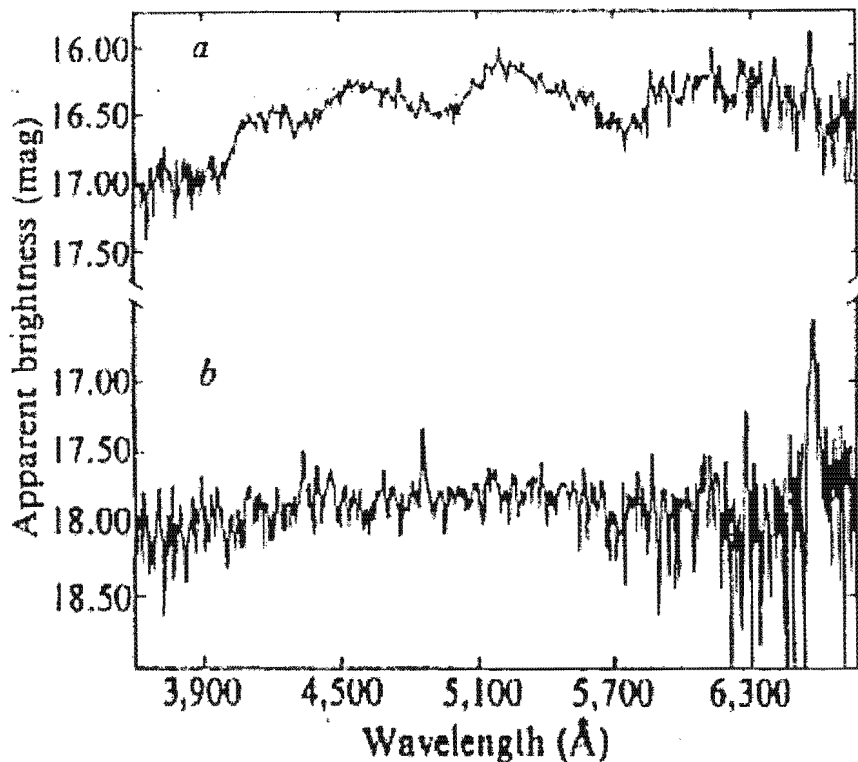
Figure 2.3: Spectrum of VV Pup showing broad cyclotron humps in the continua. The upper spectrum was taken when the accretion region was in view, while the lower spectrum was taken when the accretion was behind the white dwarf (Visvanathan & Wickramasinghe 1979).

the other parameters, can be estimated from

$$\frac{\omega}{\omega_c} = \frac{-1 + \sqrt{1 + 8n\sin^2\theta}}{4n\sin^2\theta/\mu}, \tag{2.2}$$

where $\mu = mc^2/kT$, ω_c is the cyclotron frequency of spiraling electrons, ω is the observed photon frequency, n is the harmonic number and θ is the angle between the direction of propagation of radiation and the field direction (Barrett & Chanmugam 1985).

More recently cyclotron models have become a more popular means of determining field strengths (see Section 3.2).

2.1.3 Polarization

Polars tend to show a high degree of modulated polarized radiation, hence their names. The polarized radiation is associated with the magnetic field of the white dwarf. Both Meggit & Wickramasinghe (1982) and Barrett & Chanmugam (1984) pointed out that the ratio of the linear to the circular polarization is given by :

$$q = \frac{Linear}{Circular} = \frac{\sin^2\theta}{2\cos\theta}\left(\frac{\omega_c}{\omega}\right). \tag{2.3}$$

If q is observed at frequency ω and the viewing angle to the field is deduced, then it is possible to measure the cyclotron frequency, ω_c, and hence the field strength, B. This

7

method of using the ratio of linear to circular polarization, however, has been hampered by the fact that Polars are so faint. In order to obtain good signal-to-noise ratios of polarizations, polarimetric observations have to be made in relatively broad bands which integrate over one or more harmonics. Nevertheless, since the result is independent of both the temperature and optical depth of the plasma, this technique promises to be a powerful tool in determining the magnetic field strength in future.

Broad band polarimetry of IPs has resulted in the detection of circular polarization in only three out of $\sim$20 systems: BG CMi (West, Berriman, & Schmidt 1987), PQ Gem (Piirola, Hakala, & Coyne 1993) and RX J1712.6-2414 (Buckley et al. 1995). RX J1712.6-2414 has the largest polarization yet detected in an IP.

2.2 Origin and Field Configuration

2.2.1 Origin of the Magnetic Field

The origin of the strong magnetic fields in mCVs is still poorly understood. One of the theories of their origin in isolated white dwarfs is that they are inherited from progenitors, thought to be Ap/Bp stars. If the total flux $\Phi_{tot} \sim \pi R^2 B$ passing through the magnetic equator of the star can be roughly conserved, then the expected typical field strength of the star should vary as

$$\frac{B}{B_{ms}} \sim (\frac{R_{ms}}{R})^2, \tag{2.4}$$

where ms refers to the main sequence (Landstreet 1992). This means that a magnetic field of 10^3 G on a main sequence star (typical Ap/Bp stars have field strengths ranging between $3{\times}10^2$ - $3{\times}10^4$ G) with $R \sim 10^9$ m could lead to a field of 10^7 G in a white dwarf ($R \sim 10^7$ m) or 10^{13} G in neutron stars ($R \sim 10^4$ m). However, the evolution of isolated white dwarfs and CVs is completely different. The common envelope phase in CVs, for example, may give rise to a magnetic dynamo capable of generating a larger magnetic field even if the core was not initially magnetic.

2.2.2 Field Configuration

Although Polars have been studied for years, many observable quantities, including the magnetic field geometry and characteristics, have not been adequately determined or explained. The field is usually assumed to be a centred dipole, but there is ample evidence in some systems (e.g. BY Cam) that suggests that the field might be an offset-dipole or even have a multi-polar configuration (Cropper 1988). During high accretion states some observed Polars exhibit two-pole accretion, with an angular separation of considerably less than 180° (Wu & Wickramasinghe 1993). This is not what is expected from models which assume a centred dipole field geometry and accretion onto foot points of closed field lines. The accretion pole which dominates the optical/IR luminosity typically has a field strength which is a factor of two less than the field at the secondary accretion pole (see Table 5.1). This has been interpreted as evidence for the deviation of field structure from that of a centred dipole. Zeeman spectroscopy of Polars often assumes models which require either an offset-dipole or a multi-pole field. The multi-pole is usually described by a dipole-quadrupole superposition. Figs. 2.5 & 2.6 illustrates the field line pattern for a

8
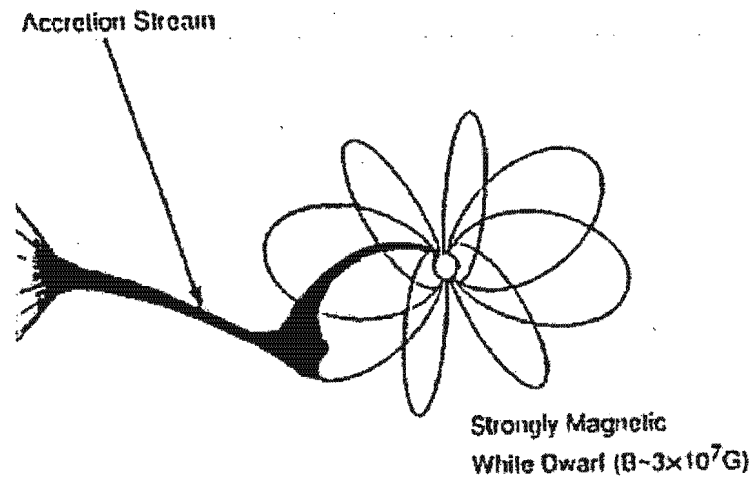
Figure 2.4: Accretion onto a magnetic white dwarf with a dipolar field (Cropper 1990).
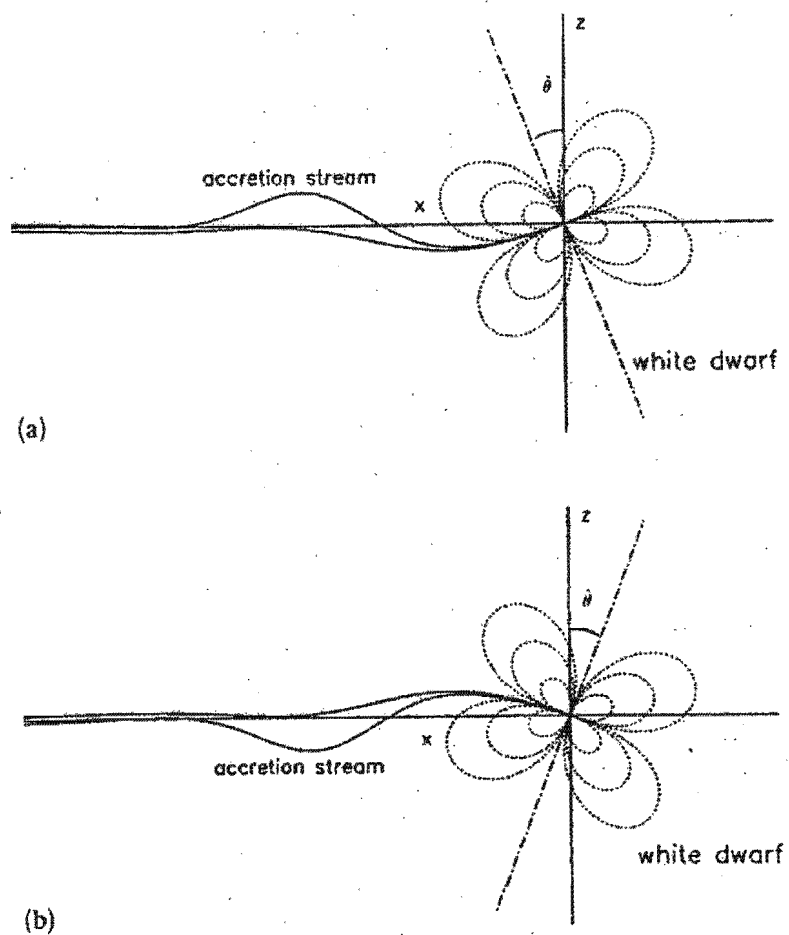
Figure 2.5: Accretion and field geometry in the dipole-quadrupole case with (a) a positive equitorial pole and (b) a negative equitorial pole (Wu & Wickramasinghe 1993).

9
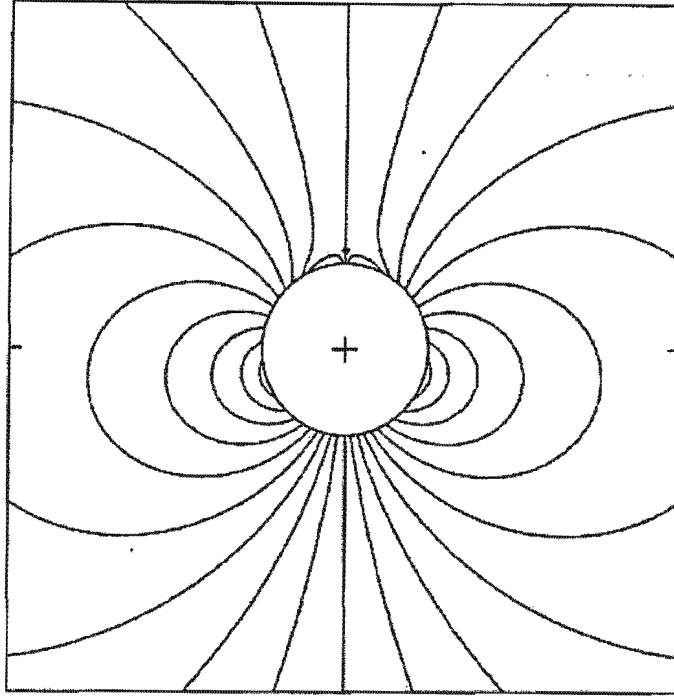
Figure 2.6: Example of a field line pattern for a dipole-quadrupole superposition (Schwope, Beuermann, & Jordan 1995).

dipole-quadrupole superposition. Some mathematical modeling of magnetic interaction of the different magnetic field configurations has been considered by various authors. More detailed descriptions can be found in Wu & Wickramasinghe (1993), for example.

Chapter 3

Cyclotron Spectroscopy

3.1 Cyclotron Emission from an Electron

A plasma subjected to a magnetic field radiates as the result of the acceleration of the charged particles gyrating around the magnetic field lines. The equation of motion of a particle of charge e and mass m, in a uniform magnetic field is given by:

$$\frac{d\mathbf{p}}{dt} = e(\mathbf{v} \otimes \mathbf{B_0}) \tag{3.1}$$

where

$$\mathbf{p} = \frac{E}{c^2}\mathbf{v}. \tag{3.2}$$

The solution of the equation of motion for the particle velocity $\mathbf{v}$ and displacement ρ gives :

$$\mathbf{v} = \hat{\mathbf{x}}\nu_\perp \cos\omega_0 t + \hat{\mathbf{y}}\nu_\perp \sin\omega_0 t + \hat{\mathbf{z}}\nu_\parallel \tag{3.3}$$

$$\rho = \hat{\mathbf{x}}\frac{\nu_\perp}{\omega_0 t}\sin\omega_0 t + \hat{\mathbf{x}}\frac{\nu_\perp}{\omega_0}\cos\omega_0 t + \hat{\mathbf{z}}\nu_\parallel t \tag{3.4}$$

where $\omega_0 = -\frac{eB_0}{\gamma m_0}\sqrt{1-\beta^2}$ is the cyclotron frequency taking into account the relativistic mass and γ is the Lorentz factor. The motion of an electron is illustrated in Fig. 3.1.

The energy emitted per unit solid angle per frequency $d\omega$ is given by:

$$W(\omega, \Omega) = \frac{e^2\omega^2}{16\pi\epsilon_0 c^3}\Big|\int_{-\infty}^{\infty} e^{-i\omega(t-\hat{\mathbf{q}}\cdot\rho/c)}[\hat{\mathbf{q}}\otimes(\hat{\mathbf{q}}\otimes\mathbf{v})]dt\Big|^2 \tag{3.5}$$

where $\hat{\mathbf{q}}$ is the propagation vector and, if assumed to lie in the x-z plane, is given by:

$$\hat{\mathbf{q}} = \hat{\mathbf{x}}\sin\theta + \hat{\mathbf{y}}(0) + \hat{\mathbf{z}}\cos\theta. \tag{3.6}$$

The solution of the integral in (3.5) is :

$$2\pi\sum_{-\infty}^{\infty}[J_n(x); -i\frac{dJ_n(x)}{dx}; \frac{1-\beta_\parallel\cos\theta}{\beta_\perp\sin\theta}J_n(x)]\delta(y). \tag{3.7}$$

The argument of the Bessel function J is

$$x = \frac{\omega}{\omega_0}\beta_\perp\sin\theta \tag{3.8}$$

11
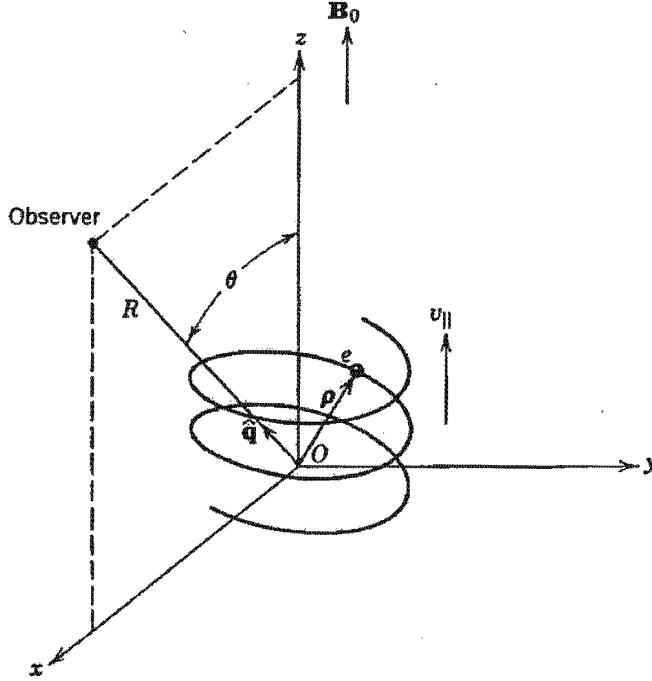
Figure 3.1: Vector diagram for an electron in helical motion in a uniform magnetic field (Bekefi 1966).

and the argument of the δ function is

$$y = n\omega_0 - \omega(1 - \beta_{\parallel}\cos\theta).$$ (3.9)

From this it can be calculated that the electron radiates at frequencies

$$\omega = \frac{\omega_c n}{\gamma(1 - \rho\beta\cos\theta)},$$ (3.10)

where $\beta = v/c, \rho$ is the pitch angle with $\rho = \tan^{-1}[\frac{2\pi v_{\parallel}}{r\omega_0}]$, $\gamma = \sqrt{1 - \beta^2}$, n is the harmonic number and $\omega_c(= \omega_0\gamma)$ is the fundamental cyclotron frequency for a spiraling, non-relativistic, electron in a magnetic field B (Bekefi 1966).

3.2 Application of cyclotron theory to Polars

Hirshfield, Baldwin, & Brown (1961) presented a temperature-dependent formula for the frequency of cyclotron lines:

$$\frac{\omega}{\omega_c} = n(1 - n/\mu),$$ (3.11)

where $\mu = mc^2/kT$. This formula was obtained by considering a two dimensional Maxwellian distribution of electrons and propagation of radiation perpendicular to the magnetic field. Barrett & Chanmugam (1985) generalized the equation of Hirshfield, Baldwin, & Brown (1961) by considering a three-dimensional distribution of electrons viewed at an angle θ to the magnetic field. They obtained:

$$\frac{\omega}{\omega_c} = \frac{-1 + \sqrt{1 + 8n\sin^2\theta}}{4n\sin^2\theta/\mu}.$$ (3.12)

12

This can be rewritten in terms of wavenumber as :

$$f_{n+i} = \frac{1.8675 \times 10^{-4}(n+i)B}{1 + \sqrt{1 + ((n+i)T\sin^2\theta/63.872)}}, \tag{3.13}$$

where n is the harmonic number of the reddest peak in the spectrum, f_{n+i} are the wavenumber of successive cyclotron peaks and B is in Gauss and T in keV. This equation is useful in determining the field strength and harmonic numbers. T and θ are not found independently, though, but only as the product $T\sin^2\theta$. At low temperatures, the position of the nth harmonic for a given field B and viewing angle $\theta = 90°$ is approximated by

$$\lambda_n = \frac{10710}{n}(\frac{10^8}{B}), \tag{3.14}$$

where λ_n is in Å and B given in G (Ferrario et al. 1994). More recently cyclotron models have become a more popular method for determining the magnetic field strengths. Models have been constructed assuming constant electron temperature, T_e, electron number density, N_e, and radial thickness above the white dwarf surface, s. The emission region is characterized by an optical depth parameter (Meggit & Wickramasinghe 1982). In the most simple case of a homogeneous isothermal plasma with large Faraday rotation, the radiative transfer equation becomes :

$$I_{\pm} = I_{RJ}[2 - e^{-\tau+} - e^{-\tau-}], \tag{3.15}$$

where $\pm$ refers to the two magneto-ionic modes (Barrett & Chanmugam 1985). I_{RJ} is the Rayleigh-Jeans intensity and optical depth $\tau_{\pm} = l\alpha_{\pm} = \Lambda\chi$ (l: geometrical path length, α: cyclotron absorption coefficient, χ: dimensionless absorption coefficient). The optical depth parameter is given by $\Lambda = l\frac{\omega_p^2}{c\omega_c} = 2\times10^5(\frac{l}{10^5 cm})(\frac{N_e}{10^{16}cm^{-3}})(\frac{30MG}{B})$ with the plasma frequency $\omega_p = (4\pi Ne^2/m)^2$, and the dimensionless absorption coefficient becomes a function of temperature, T, angle to the magnetic field, θ, and harmonic number, n. The cyclotron absorption coefficients, $\alpha_{\pm}$, can be calculated in a number of ways. Numerical calculations of cyclotron absorption coefficients have been extensively discussed in plasma physics (e.g. Tamor 1978) and astrophysics literature (e.g. Ramaty 1969). Because the numerical calculations can involve significant use of computer time, searches for analytical formulae have been made. A large number of analytical formulae for the cyclotron absorption coefficients exist. The two most important ones are the single particle method by Bekefi (1966) and the dielectric tensor method (e.g. Montgomery & Tidman 1964).

Most cyclotron calculations assume idealized emitting structures, e.g. point sources, but the shape of the accretion region is thought to be more complex and this can change the shape of the cyclotron spectrum. Wickramasinghe & Ferrario (1988) investigated the properties of cyclotron radiation taking into account the effects of field spread, density and temperature structure and geometrical extension, but taking all these into account increases the number of free parameters considerably. Ferrario & Wickramasinghe (1990) considered arc-shaped cyclotron emission regions. Their calculations were carried out by dividing the emitting region into sufficiently small sub-regions over which the magnetic field strength and the angle between the field direction and line of sight could be taken as a constant. The contribution of each emitting element was weighted according to the size of its area projected onto the plane of the sky.
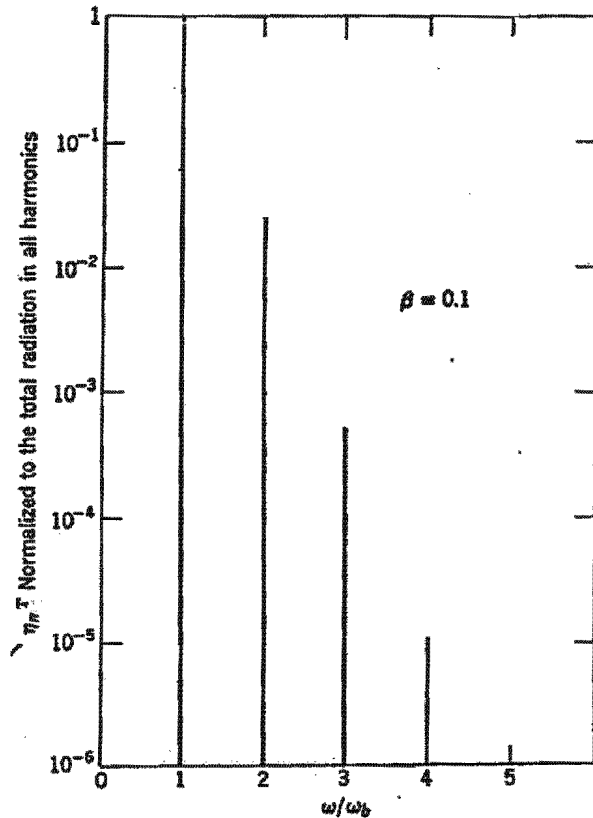
Figure 3.2: Sketch of the spectrum of the cyclotron radiation emitted by a nearly relativistic electron where $\beta = v/c$. η_n^T, the total radiation in harmonic n, is plotted versus $\frac{\omega}{\omega_c}$ (Bekefi 1966).

3.3 Emission Profile

The cyclotron radiation spectrum, in general, consists of spectral lines occurring at frequencies given by Equation 3.10. The relative distribution of power in the different harmonics depends on the energy of the electron. The total power radiated in harmonic n is obtained by dividing the emitted power $W(\omega, \Omega)$ by the "total time of radiation" and integrating the result over frequency ω and solid angle $d\Omega$ to give

$$\eta_n^T = \frac{e^2 \omega_c^2}{2\pi\epsilon_0 c} \frac{1 - \beta_0^2}{\beta_0} [n\beta_0^2 J_{2n}'(2n\beta_0) - n^2(1 - \beta_0^2) \int_0^{\beta_0} J_{2n}(2nt)dt], \tag{3.16}$$

where J is the Bessel function and J' its first derivative. At low temperature ($T_e \ll 0.1$ keV) virtually all power is radiated in the fundamental (see Fig. 3.2), whereas at $T_e = 50$ keV, for example, only a few percent is radiated in the fundamental (Wickramasinghe 1988). Fig. 3.2 illustrates the spectrum of cyclotron radiation emitted by a nearly relativistic electron ($v = 0.1c$).

Cyclotron emission is optically thick at low harmonics, but optically thin at higher ones where it can escape and be detected as polarized radiation (Wickramasinghe 1988). The emission from low harmonics, when the optical depth is high, is unpolarized, exhibiting a Rayleigh-Jeans spectrum ($I_\omega \propto \omega^2$) declining to lower frequencies. The transition between the optically thick and optically thin regions occurs over a narrow frequency range, near

14

$\frac{\omega}{\omega_c} \sim n^*$, where the energy distribution is relatively flat and strongly polarized. n^* is a strong function of Λ for a given T_e and θ. Fig. 3.3 illustrates the relationship between n^* and Λ, the optical depth parameter.

Another important property is the angular dependence of the emission. For $n > 1$ the radiation is beamed perpendicular to the magnetic field and the beaming becomes more pronounced at higher harmonics (see Fig. 3.4). For optically thin emission the FWHM of the beam is approximately (e.g. Wickramasinghe 1988)

$$\Psi \sim 80^o (\frac{\omega}{\omega_c})^{\frac{-1}{6}} (\frac{kT_e}{50keV})^{\frac{1}{3}} \qquad (3.17)$$

The width of the cyclotron emission depends on a number of broadening effects. These effects are summarized in (Bekefi 1966) :

(i) *Radiation Broadening.* This results because the electron loses energy and a finite length wave train cannot have a pure frequency.

(ii) *Collision Broadening.* An electron approaching a heavier particle (e.g. an atom) experiences appreciable acceleration only over a limited period of time.

(iii) *Doppler Broadening.* This results from the random motion of electrons along lines of force. The line width is of the order of $\omega(v_0/c)\cos\theta$ where v_0 is thermal velocity and θ is the angle between the direction of observation an the magnetic field.

(iv) *Relativistic Mass Change.* This comes from the fact that electrons of different energies have slightly different cyclotron frequencies.

(v) *Self Absorption of Radiation.* When the optical thickness at the line centre reaches unity the radiant energy effectively distributes itself over a wider frequency range.

(vi) *Plasma Dispersion Effects.* In a dense plasma the dispersive properties affect the line shape and width.

(vii) *Non-uniformity in the Magnetic Field.* Small non-uniformities in the magnetic field over a region of plasma from which the radiation is received cause line broadening of the order $\Delta\omega_c$.

In Polars the major contribution to broadening is Doppler broadening due to the electron temperature. The broadening also increases with harmonic number since the radiation comes preferentially from high energy electrons in a Maxwellian distribution. The emission profile of a given harmonic is asymmetric, exhibiting an extended wing towards lower frequencies. This is a consequence of the fact that the radiation of the more energetic electrons is weighted towards the higher harmonics. The harmonics in the spectrum of UZ For, HU Aqr and MR Ser (in Fig. 3.6) illustrate this fact quite nicely. In the presence of a low field or high electron temperature ($T_e > 20$ keV), or a combination of both, the harmonic humps are so close together that they are smeared into a quasi-continuum, as can be seen in the spectra of BL Hyi (bottom panel in Fig. 3.6). In such cases it might be necessary to observe in the red/near-infrared section of the spectrum to identify the harmonics.
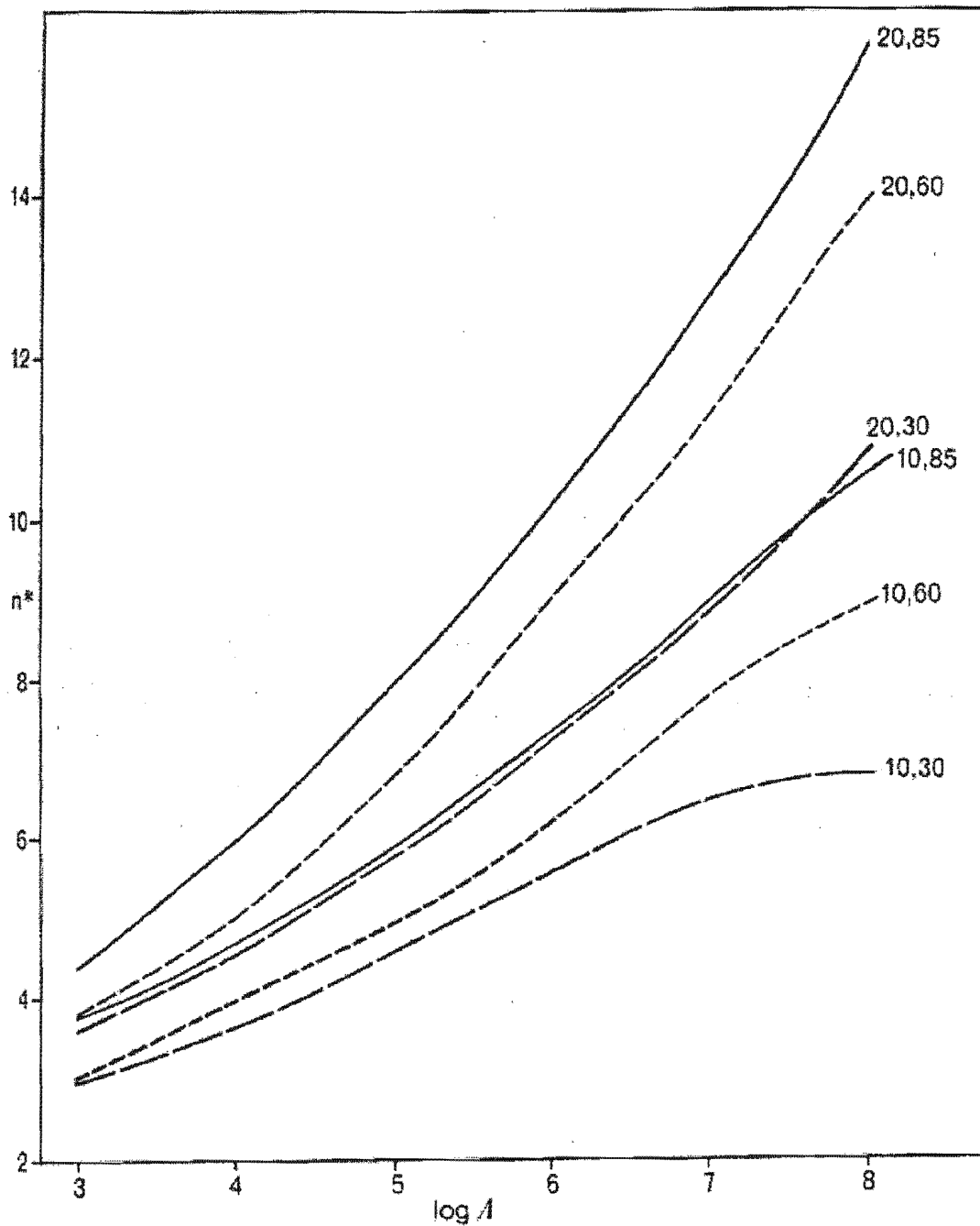
Figure 3.3: The dependence of the harmonic number n^*, where the emission region changes from being optically thin to thick, on Λ, T_e & θ for point source models. Curves are given for both $T_e = 20$ & 10 keV, with the solid curves for $\theta = 85°$, the short dashed curves for $\theta = 60°$, and the long dashed curves for $\theta = 30°$ (Wickramasinghe 1988).
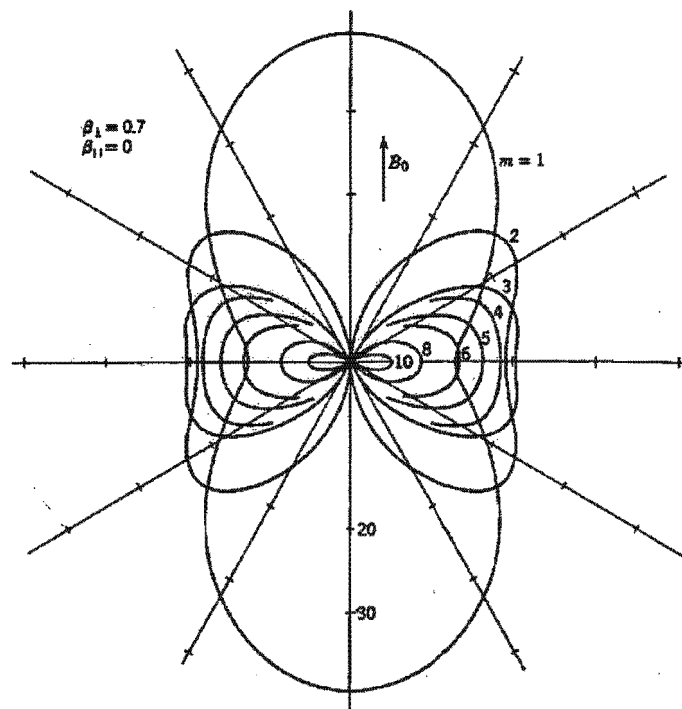
Figure 3.4: The angular distribution of cyclotron radiation beamed from a mildly relativistic electron where m refers to harmonic number (Bekefi 1966).
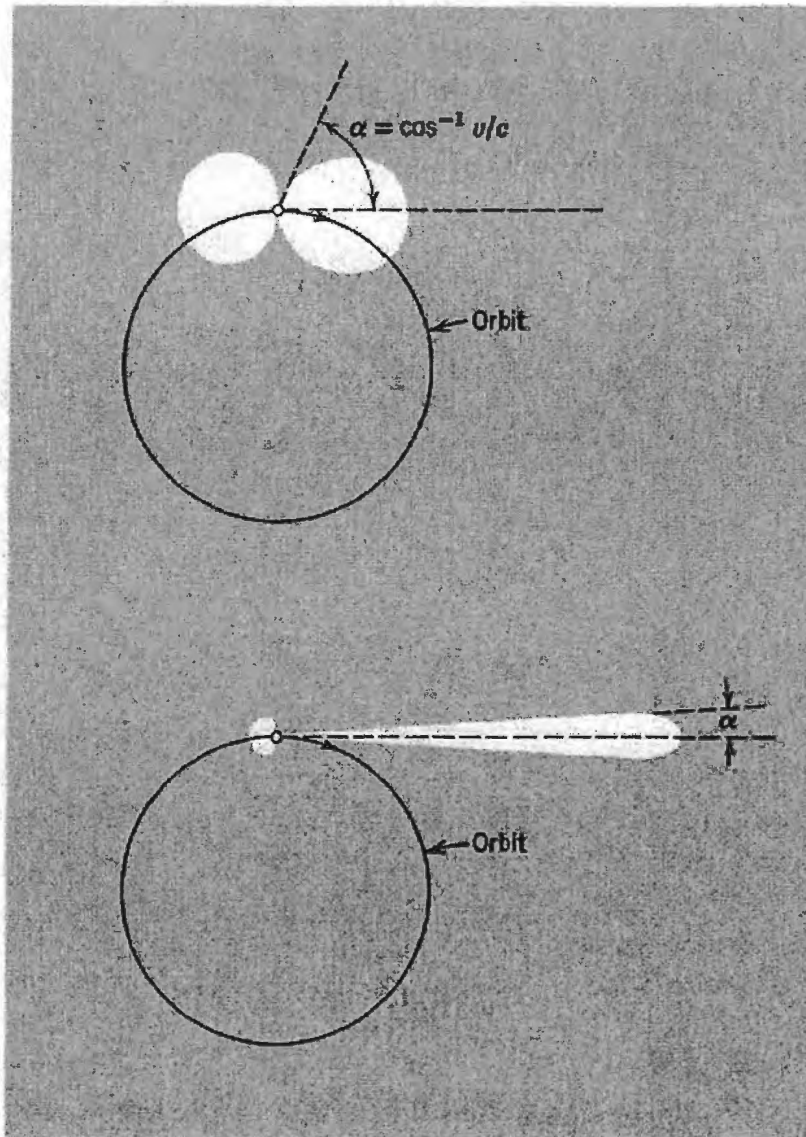
Figure 3.5: A sketch of the polar emission diagram of the instantaneous radiation intensity of a non-relativistic electron (above) and a highly relativistic electron (below) (Bekefi 1966).
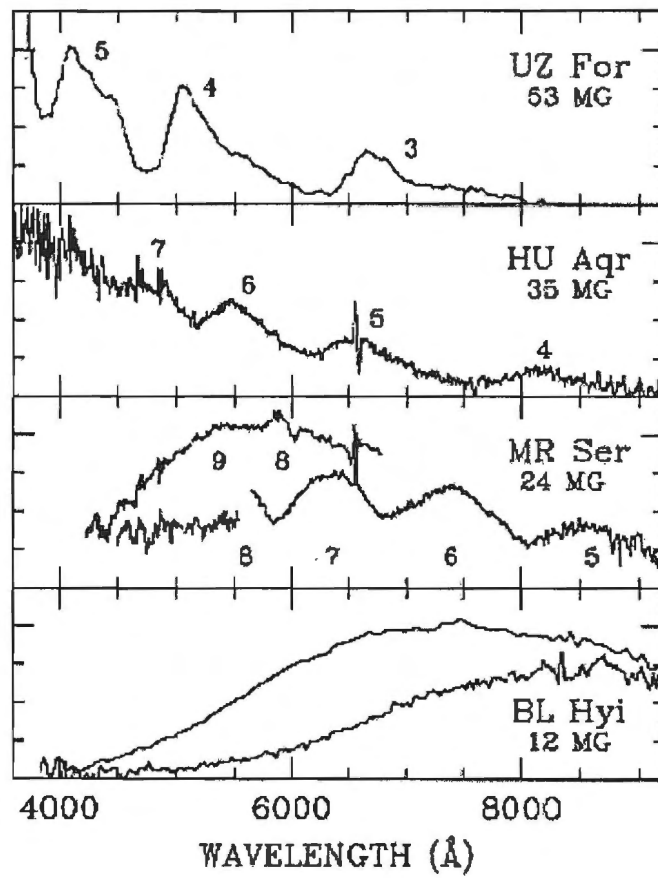
Figure 3.6: Cyclotron spectra of four Polars with different field strengths and with harmonic numbers indicated (Beuermann 1996).

Chapter 4

The Emission Region

4.1 Line spectrum

The spectra of mCVs in the UV, optical and infrared are rich in emission lines. High excitation lines such as HeII $\lambda4686$ and NV $\lambda1240$ are especially prominent, particularly in Polars (Cropper 1990). Phase resolved and high resolution spectral studies of these systems are usually limited to the optical, and reveal lines with multiple components, each with distinct radial velocity variations. These lines arise primarily in the accretion stream, the coupling region, the accretion funnel, the secondary star and disc (for an IP). By modeling the line parameter variations, the position of the emitting gas can be located. More recently, Doppler tomography has proved a popular tool in mapping the various velocity components present in the emission lines. Observations of optical emission lines have to satisfy the following criteria :

(i)They generally have to be obtained during a high state (when lines are seen). However, Doppler tomography has also been done on several Polars in a low state (e.g. QQ Vul; Schwope et al. 2000)
(ii)They must have sufficient time resolution and total duration to study the radial velocity variations, e.g. $\Delta\phi = 0.05$.

4.2 Line profiles

4.2.1 Polars

The first clear evidence for multiple structure of the emission lines in Polars was found by Cowley & Crampton (1977). These authors identified a broad "base" component, a narrow "peak" component and, at some phases, a very narrow component. Given sufficient signal-to-noise ratios, such components have been found in almost all Polars. It is now standard practice to look for a broad and a sharp component in all Polars. Higher quality observations have often revealed that the optical emission lines are more complex than the simple broad and sharp component structure. An example of the complex line profiles is the observations of V834 Cen by Rosen, Mason, & Cordova (1987). They found four components: the broad "base" component (BBC), a medium velocity component (MVC), a high velocity component (HVC) and a narrow component.

Initially the origins of such components in Polars were unclear. By 1980 Schneider
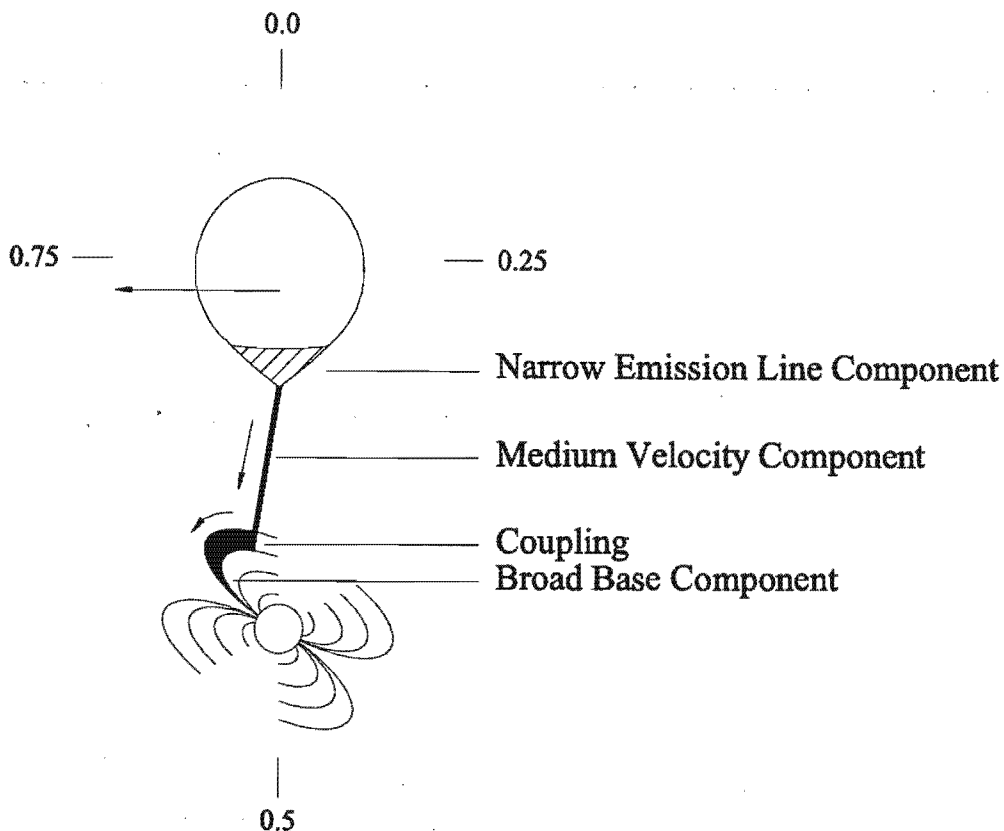
Figure 4.1: The emission sites for the various emission line components. The irradiated face of the secondary is indicated by the hatched section, while the accretion stream is indicated by the solid region. The two sets of arrows indicate the direction of motion of the secondary star and accretion material respectively. The phases are indicated for the systems rotating in an anticlockwise direction.

& Young (1980a) were modeling them assuming they arose from different parts of the stream: the BBC from the accretion column and the narrower "peak" components from further away in the stream. The narrowest component was associated with the heated face of the secondary, while the broadest components originate in the post-coupling region. Fig. 4.1 illustrates the emission sites where the different components originate.

Mukai (1988) estimates that a spectral resolution of 2.5 Å, or better, is needed to resolve all the components when observations are made in the blue (∼4000 − 5000 Å). There is at least one example where a high spectral resolution (2.1 Å) did not result in a clear distinction of line components (Schneider & Young 1980b). The problem was most probably due to the poor phase resolution ($\Delta\phi \sim 0.08$) of this particular data set, since longer exposure times smear out the line profiles. The need for high time resolution was also emphasized by Crampton, Hutchings, & Cowley (1980) and McCarthy, Clarke, & Bower (1986). McCarthy, Clarke, & Bower (1986) could resolve the line components using a resolution of 3.5 Å, but had a high phase resolution (0.035) in their favour. Mukai (1988) indicates that as a rough guide, a phase resolution of the order of 0.05 is desirable if the multiple line components are to be separated.

The emission line components show wavelength variations over the orbital cycle. These variations are due to the Doppler effect, which shifts the observed wavelengths as the

different line emitting regions are approaching or receding from the observer. The radial velocity measurements of the emission line can be fitted with sinusoids

$$v_r = (\frac{\lambda - \lambda_0}{\lambda_0}) \times c = \gamma + K \sin 2\pi(\phi - \phi_0), \qquad (4.1)$$

where λ_0 is the laboratory wavelength of the line, ϕ the binary phase, γ the systemic velocity of the system and K is the velocity amplitude (Schneider & Young 1980b). The broad base component, usually produced by gas falling down towards the accretion zone near the white dwarf, can have a velocity amplitude in excess of 1000 km s^{-1} (e.g. Warner 1995) and velocity dispersion almost as large. The γ-velocity of the broad line component could show changes at different epochs if there are variations in the accretion rate.

4.2.2 Intermediate Polars

Typically emission line profiles in IPs show components originating from the truncated disc and are far less complex than Polars. For IPs accreting near their equilibrium condition ($\omega_s \sim \omega_c = 0.97$) and $500 \leq P_{rot}(1) \leq 2000$ s, the disc emission-line profiles should have a full width at zero intensity (the wings of the emission line profile), FWZI $\sim 2000 \sin i$ km s^{-1} (Warner 1995). The equilibrium condition is when there is no net torque on the primary even though it is accreting. ω_s is the "fastness parameter" and ω_c is its critical value where the positive torque (material and magnetic torque) balances the spin-down torque. $P_{rot}(1)$ is the white dwarf rotational period. If we are able to see to the surface of the white dwarf there will be an additional source of line emission: namely, gas flowing down the accretion curtain, i.e. the same source that produces the broad component in Polars. In Polars this has a FWZI ~ 2000 km s^{-1} and a velocity amplitude up to 1000 km s^{-1} with orbital period P_{orb}. In the IPs we might expect a similar width and amplitude, but modulated with period $P_{rot}(1)$.

4.3 Doppler Tomography

The previous section discussed the origins of the emission line components. Doppler tomography is a way to test these ideas by looking at observable accretion features. Using phase-resolved spectroscopy allows one to map indirectly the accretion flows in interacting binaries, separating the different emission sites, e.g., the heated face of the secondary or the accretion stream.

Doppler emission line tomography of CVs was introduced by Marsh & Horne (1988). While these authors use a maximum entropy algorithm to process the data, the simpler back-projection algorithm (Russ 1992) is used in this project. Doppler tomography is similar to, and uses the same algorithms as, X-ray tomography used in the medical field (Kaitchuck et al. 1994). Unlike in the medical case, where a three dimensional image is built up, there is only one plane to be considered in the case of binary stars, i.e. the orbital plane. As the binary system rotates, giving a different viewing angle at each phase, emission sites have different projected radial velocities and thus Doppler shifts. Profiles of line flux versus velocity displacement from the line centre are built with the result being a distribution of emission in velocity space. Since velocity profiles are a convolution of the local emissivity and the velocity of each emitting "parcel" of gas, the direct translation

of line profiles to spatial distribution is not possible without making some assumptions about the velocity profile.

4.3.1 Image Reconstruction

The back-projection technique involves a transformation of the data from the trailed spectrogram format (i.e., a series of spectra stacked at equal time intervals) to velocity space. First, a coordinate system is defined which is fixed in the rotating frame of the stars. The coordinate system is illustrated in Fig. 4.2. The x-axis lies between the stars, the positive y-axis points in the direction of motion of the secondary and the z-axis is perpendicular to the orbital plane. The axes intersect at the centre of mass of the system (i.e., the origin). Any velocity vector (V_x, V_y) stationary in this coordinate system will have a corresponding curve in the trailed spectrum given by

$$V(\phi) = \gamma - K_x \sin 2\pi\phi + K_y \sin 2\pi\phi, \qquad (4.2)$$

where ϕ is the orbital phase (Marsh & Horne 1988). The curve in the trailed spectrum resembles an S-character and is often referred to as an S-wave (here an S-wave refers to any S shape in the trailed spectrogram and not to any specific region (e.g. hot spot) on the accretion disc). This vector can also be represented by a point in the Doppler map. It is therefore straightforward to produce a trailed spectrogram from a Doppler map. The reverse, however, is what is really required. What is needed is to derive the intensity distribution in the Doppler map from the trailed spectrogram. The simplest way to do this back projection is to trace all possible S-waves and calculate the average flux through that particular S-wave. Each radial velocity curve will correspond to a point on the Doppler map, with the average flux giving its intensity. The Doppler map can be pictured as being composed of a series of pixels like a CCD image. For each pixel the corresponding sinusoid through the data is found and the line flux is summed along the sinusoid. This process is repeated for each pixel and the result is a Doppler map. In this way one is only able to derive a phase-averaged distribution, since one only calculates the average flux. Doppler tomography thus assumes that each emission site is equally visible over all phases, which is not necessarily true (e.g. during an eclipse).

Most points in the Doppler map correspond to sinusoidal velocity curves with a different amplitude and phasing from the curve in the data. These points contain a small mean flux because the observed flux along their velocity curve is zero except for two small contributions from the phase intervals during which the velocity curve crosses the S-wave in the data. The Doppler map will, however, have a peak at the velocity coordinates whose S-wave matches exactly that of the data. Points close to the peak will have a velocity curve that slowly crosses the S-wave in the data, and will therefore have a higher average flux than those points further from the peak. This cross-over effect basically defines the point spread function of the algorithm. It has a Gaussian core and broad wings with a 1/V (1/velocity) profile. To sharpen the point spread function of the back-projection algorithm, a Fourier filter is applied to each spectrum before back projection. This is known as filtered back-projection (Horne 1991). The Fourier filter used has the form

$$G(\omega) = (\omega/\omega_N) exp[-(\frac{\omega}{\omega_c})^2/2], \qquad (4.3)$$

Doppler Coordinates

Position Coordinates
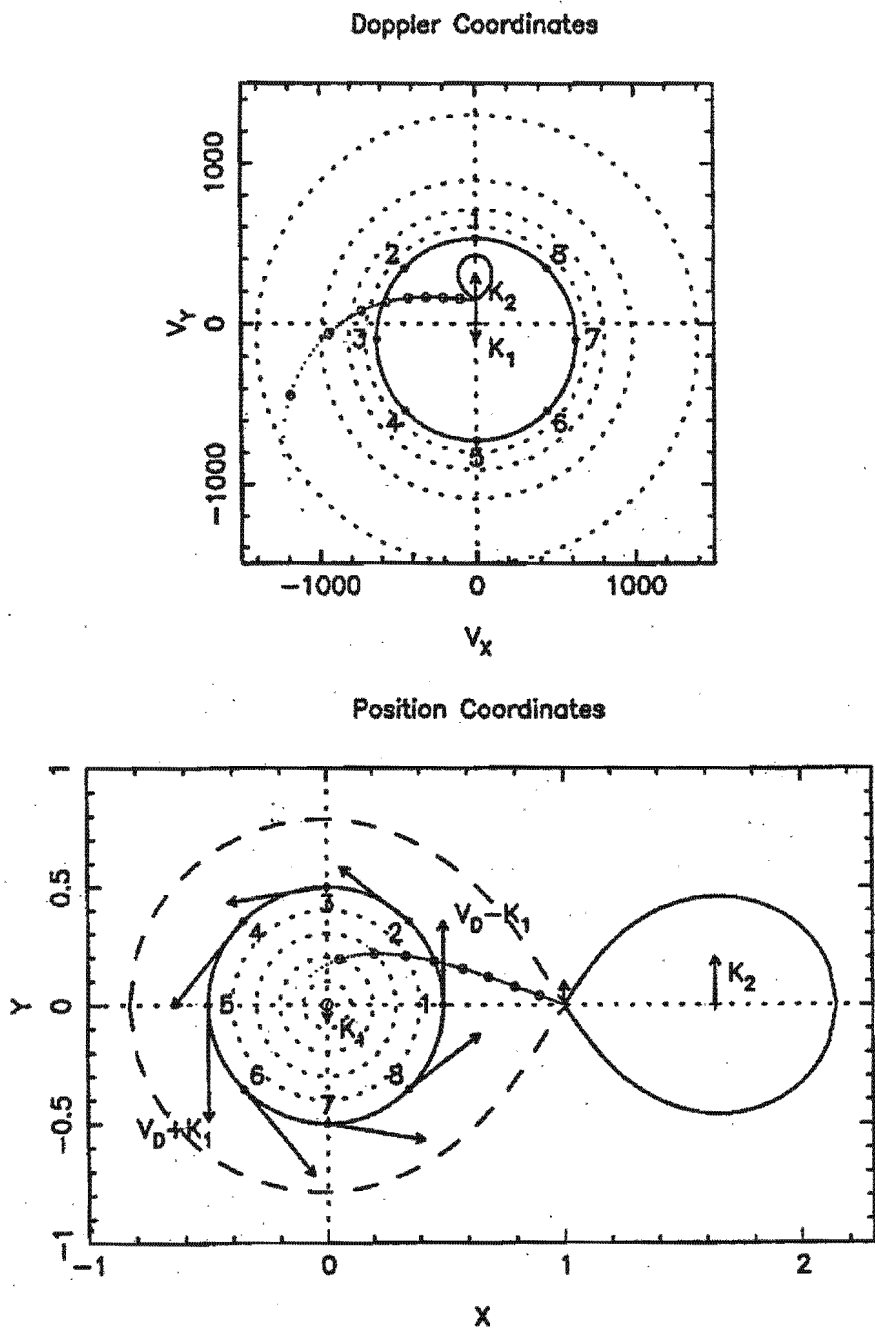
Figure 4.2: The relationship between the velocity coordinates in a Doppler map (top) and the spatial coordinates in the binary frame. The secondary star is mapped uniformly into a rotated Roche lobe. Disc rings at different radii map into rings at the corresponding (Kepler) velocity, resulting in an inside out picture of the disc since the inner ring has higher velocity. The centre of mass is per definition at the origin of the map. The ballistic trajectory of the gas stream is plotted in both frames. The small circles are spaced at equal intervals in radius from the disc center (Marsh & Horne 1988).

where ω_N is the Nyquist frequency. The first term suppresses the $1/V$ tail, while the second term suppresses the amplification of high frequency noise that occurs with Fourier filters. The cutoff frequency ω_c is set by the spectral resolution of the data.

4.3.2 Limitations

As mentioned previously, a fundamental assumption in the production of a Doppler map is that each line emission site is equally visible over all phases. Clearly eclipsing systems violate this assumption. However, the data from the eclipse phase can be safely excluded from the analysis. Doppler tomography also implicitly assumes that the emission is completely optically thin and bound to the orbital plane of the binary. Both prerequisites are violated in Polars due to the presence of optically thick radiating or absorbing surfaces, and the presence of out-of-plane velocities along magnetic field lines. However, the impact of out-of-plane emission on Doppler maps can become large only for low inclination systems, but these are generally unfavorable targets for Doppler tomography due to their low projected radial velocities. Systems which show a spectral feature at only one orbital phase cannot be modeled by a Doppler map. Emission from a wind could, for example, potentially confuse the interpretation of the Doppler map. Another disadvantage which must be kept in mind when interpreting Doppler maps is that more than one distinct parcel of gas can have the same velocity coordinate, but different spatial location.

Schwope et al. (1998) mention three recipes which can be applied in order to improve on the goodness of fit: (a) use a different subset of the data (in the optically-thin case the data from half a binary orbit gives a full map: one can construct a series of maps, using for each map half of the data, $\Delta\phi = \phi_{start} + 0.5$, sequentially shifting the start phase ϕ_{start}, and then inspect these for systematic changes); (b) decompose the line profiles, e.g. by removing the NEL, from the secondary star; (c) map line profiles on predefined surfaces.

4.3.3 The Advantages

Doppler maps provide an "inside-out" view because high velocity gas appears at the outer portions of the map and lower velocity gas towards the inner regions, whereas the reverse is the case for a spatial map of a Keplerian accretion disc. Without detailed knowledge of the velocity field, we cannot transform the velocity map into a spatial one. However, the physical location of the emission line components can be identified. Features in the Doppler map can easily be identified in the trailed spectrogram. In cases where the system parameters are known the locations of the stars and the Roche lobes can be positioned on the maps. Any emission from the heated face on the secondary can thus be easily identified.

Basic system parameters like the binary mass ratio can also possibly be determined by tomography. If one assumes that the centre of light of the horizontal stream in the Doppler map of Polars follows a one-particle trajectory in the gravitational potential of the binary with mass ratio q ($= M_2/M_1$) one has a good handle on the value of q. Another constraint on q comes from the location of the bright spot on or near the irradiated surface of the secondary. Again the photocentre can be used to determine the size of the Roche lobe and hence the mass ratio q (Schwope et al. 1998).

Chapter 5

Cyclotron spectroscopy: a review of objects

Cyclotron spectroscopy is by far the most successful method for measuring field strengths in Polars. Of the 33 Polars with measured field strengths, about 2/3 have been determined by cyclotron spectroscopy (Beuermann 1996). Table 5.1 is a list (compiled mostly from Beuermann (1996)) of Polars with magnetic field strengths derived from cyclotron spectroscopy. A review of all Polars with field strengths determined by cyclotron spectroscopy is presented in a roughly chronological order with the more recently discovered Polars last.

5.1 VV Pup

In its most commonly observed state, the light curve of VV Pup consists of a bright phase ($V_{mag} \sim 15 - 16$) which lasts for 40% of the orbital period and a faint phase which lasts for the remainder. Cyclotron features are observed in the bright phase (Wickramasinghe & Meggit 1982). The high orbital inclination of $i \sim 75^o$ and high colatitude of the main accretion region of $\delta \sim 150^o$ leads to a long self-eclipse of the main spot by the white dwarf as the system rotates. Table 5.2 lists the parameters B, kT and θ for VV Pup obtained by different investigators. Fig. 5.1 show the spectra for the bright and faint phases as obtained by Schwope & Beuermann (1997).

5.2 DP Leo

DP Leo was the first eclipsing AM Her system to be discovered (Biermann et al. 1985). The eclipse is important for a number of reasons, principally showing that the primary rotates synchronously with the secondary. This confirms that the magnetic field is always presented in the same orientation to the accretion stream of the secondary. Eclipses also allow determination of the size and location of the accretion regions.

Figs. 5.2 & 5.3 show phase resolved spectra for DP Leo, while Fig. 5.4 show an average spectrum for phase ~ 0.75. One hump at ~ 15890 cm^{-1} is particularly prominent in the spectra taken at the beginning and end of the bright phases. At these phases the cyclotron emitting region is seen on the limb of the white dwarf, with accreting field lines nearly perpendicular to the line of sight. Because the humps disappear entirely at the

Table 5.1: P_{orb} refers to the orbital period and $B_{cyc,1}$ & $B_{cyc,2}$ are the field strengths for the main and secondary accreting poles, respectively, obtained from cyclotron spectroscopy.

System	P_{orb} min	$B_{cyc,1}$ MG	$B_{cyc,2}$ MG	Ref
RX J0132-65	78	68		1
RX J2022-39	78	66		1
EV UMa	80	31		2
EF Eri	81	16	21	3,4
A2315-59	89	≤ 17		5
DP Leo	90	31	59	6,7
EU UMa	90	43		8
RX J1844-74	90	25		9
VV Pup	100	31	54	10,11
V834 Cen	101	23		12,13
RX J0453-42	102	36		14
MR Ser	113	24		15
Bl Hyi	114	23		16,17
ST LMi	114	12		18,19
EK UMa	114	34/47		20,21
AN UMa	115	29		21,22
RX J1724+41	120	65-70		23
HU Aqr	125	35		24
EU Cnc	125	42		25,26
UZ For	126	53	75	27,28,29,30
RX J0531-46	133	19		31
QS Tel	140	47	75	32
AM Her	186	14		33,34,35
BY Cam	202	28		21,22
MN Hya	203	42		40
QQ Vul	222	31/36		22
RX J1313-32	255	42		36
RX J0203+29	275	38		37
EUVE1429-38	286	17		38
RX J0515+01	480	61		39

(1)Burwitz *et al* 1997, A&A 327,183;(2)Osborne *et al*, MNRAS 270,650; (3)Östreicher *et al* 1990, ApJ 350,324;(4)Ferrario *et al* 1996, MNRAS 282,218;(5)Thomas & Reinsch, A&A 315,L1;(6)Cropper *et al*, MNRAS, 245, 760;(7)Cropper & Wickramasinge 1993, MNRAS 260,696;(8)Beuermann 1996, Tata Inst. Fund, Res.;(9)Bailey *et al*, MNRAS 272,579;(10)Wickramasinghe *et al* 1989, ApJ 342,135;(12)Schwope & Beuermann 1997, Astr.Nachr 318,111;(13)Ferrario *et al* 1992, MNRAS 256,252; (14)Burwitz *et al* 1995, A&A 305,507;(15)Schwope *et al* 1993, A&A 278,487;(16)Schwope *et al* 1995, A&A 301,447;(17)Ferrario *et al* 1996, MNRAS 282,218;(18)Schmidt *et al* 1983, ApJ 271,753;(19)Ferrario *et al* 1993, MNRAS 262,285;(20)Cropper *et al* 1990, MNRAS 243,565;(21)Schwope 1991, PhD thesis, Technical University Berlin, Germany;(22)Cropper *et al* 1988, MNRAS 236,29P;(23)Greiner *et al* 1998, MNRAS, 296,347;(24)Schwope *et al* 1993, A&A 271,L25;(25)Pasquini em et al 1994, A&A 290,L17;(26)Beuermann & Burwitz 1995, ASP Conf.Ser. 85,99;(27)Beuermann *et al* 1988, A&A 195,L15;(28)Ferrario *et al* 1989, ApJ 337,832;(29)Schwope *et al* 1990, A&A 230,120;(30)Rousseau *et al* 1996, A&A 310,526;(31)Reinsch *et al* 1994, A&A 291,L27; (32)Schwope *et al* 1995, A&A 293,764;(33)Young *et al* 1981, ApJ 245,1043;(34)Bailey *et al* 1991, MNRAS 251,37P;(35)Wickramasinghe *et al* 1991, MNRAS 251,28;(36)Thomas *et al* 1999, in prep;(37)Schwarz 1996, Masters Thesis, Humboldt Universität Berlin, Germany;(38)Craig *et al* 1996, ApJ 457,L91;(39)Shafter *et al* 1995, ApJ 443,319;(40)Ramsay & Wheatley 1998, MNRAS 301, 95

Table 5.2: Magnetic field parameters for VV Pup as determined by various investigators (Schwope & Beuermann 1997).

B_1 MG	kT keV	θ degrees	Reference
31.8	10	90	Wickramasinghe & Meggit, *MNRAS 198, 975*
31.5	8.7	85-90	Barrett & Chanmugam, *ApJ 298, 743*
27.4-30.8	0.2-2.5	85	Canalle & Opher, *A&A 189,325*
30.5	10	85	Wickramasinghe *et al, MNRAS 342, L37*
30.5	10	75	Schwope & Beuermann, *Astron. Nach. 318*
29.5	5	75	Schwope & Beuermann, *Astron. Nach. 318*
31.5	10	75	Schwope & Beuermann, *Astron. Nach. 318*
30.5	5	75	Schwope & Beuermann, *Astron. Nach. 318*
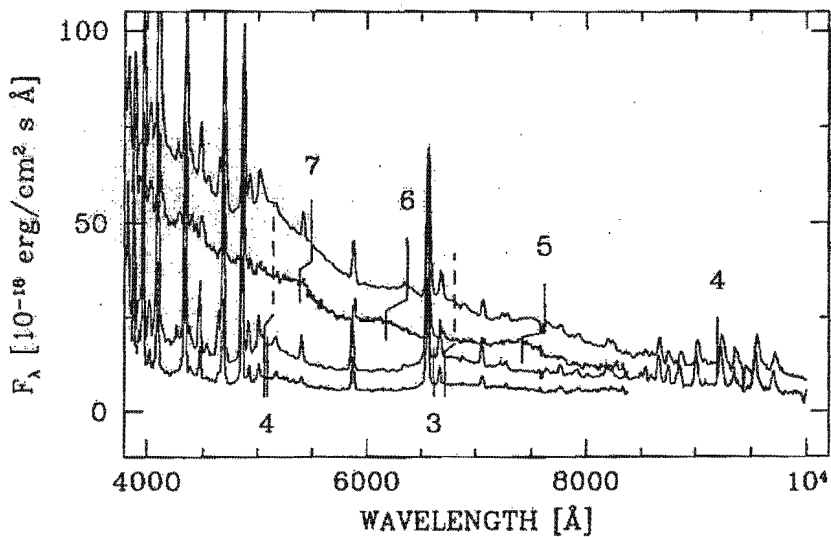
Figure 5.1: Spectra for the centres of the bright and faint phases of VV Pup obtained by (Schwope & Beuermann 1997). The positions and shifts of individual cyclotron harmonics are given. Numbers below the spectra indicate harmonics from the second, weakly accreting pole.
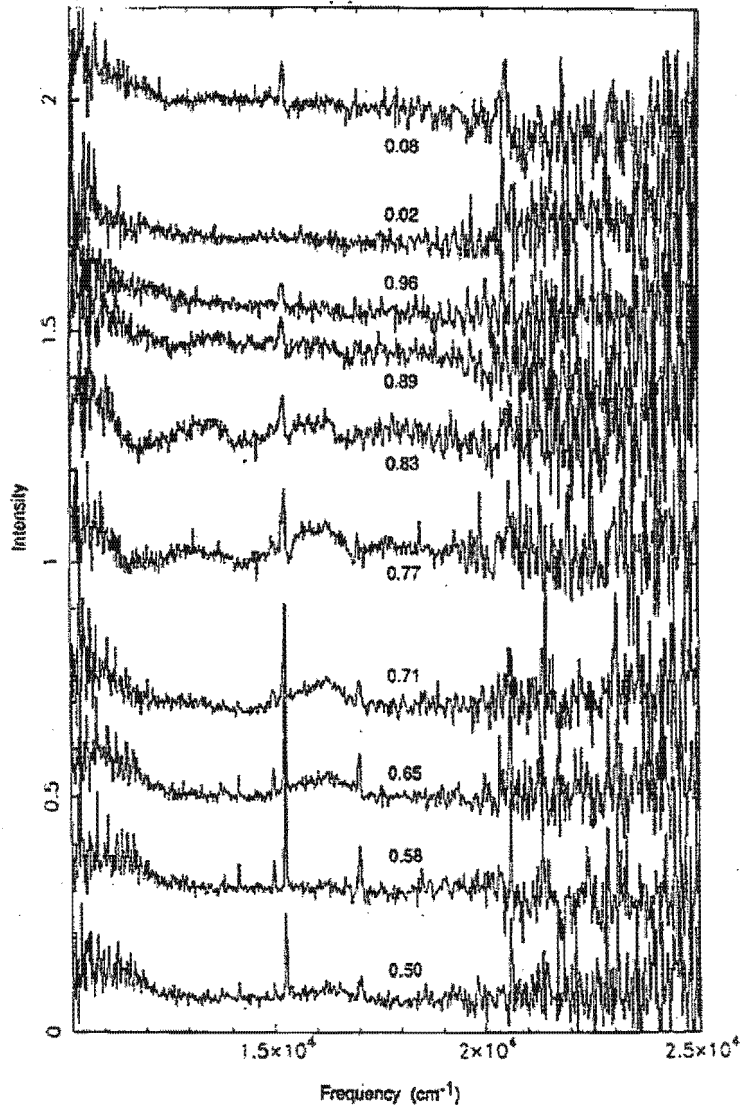
Figure 5.2: Time sequence spectra of DP Leo taken in June 1988 (Cropper et al. 1990).

midpoint of the bright phase (when the accretion region is almost face on) the cyclotron humps are clearly real. The hump at $\sim$15890 cm^{-1} is visible even in the faint phase integrating spectra at phases 0.65 and 0.71 of fig 5.2 and phases 0.41 and 0.81 of fig 5.3. Cyclotron humps are generated only by cyclotron emission in or near the accretion region; this means that accretion in DP Leo is taking place in a region which is not out of sight over the limb of the white dwarf. Cropper et al. (1990) used two methods to determine B from the cyclotron humps. These methods are described in Barrett & Chanmugam (1985) and Wickramasinghe (1988). The results are recorded in Table 5.3

5.3 EV UMa

EV UMa, with an orbital period of 79.7 min, is one of the shortest period Polars. The data obtained by Osborne et al. (1994) show two clear cyclotron humps in the red part of the spectra as seen in figs 5.5. Their data are too noisy, especially in the blue, to obtain a secure estimate of B. The two distinct humps in the best spectra are at 1.27×10^4 cm^{-1}

29
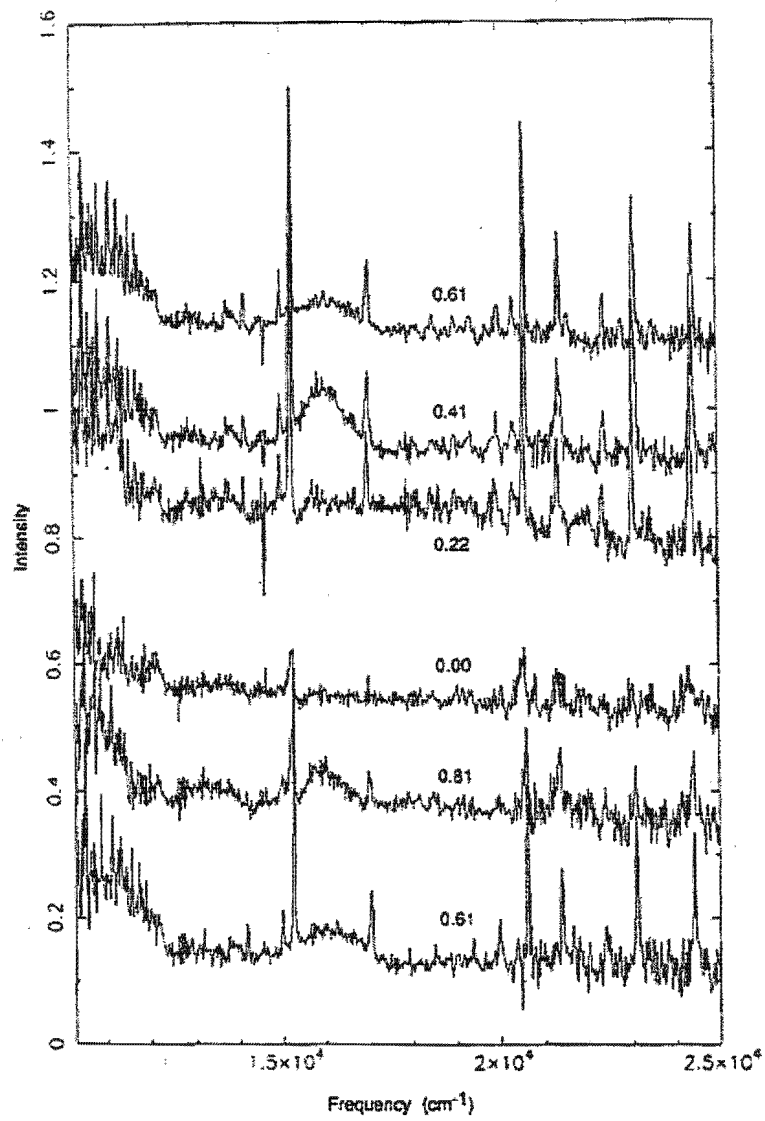
Figure 5.3: Same as for fig 5.2, but taken in January 1989.

Table 5.3: Magnetic field measurement for DP leo using the two methods (Cropper et al. 1990).

Method	B MG	T keV	n
Barrett & Chanmugam	48±1	29±2	4
Wickramasinghe	32±1	14±5	5
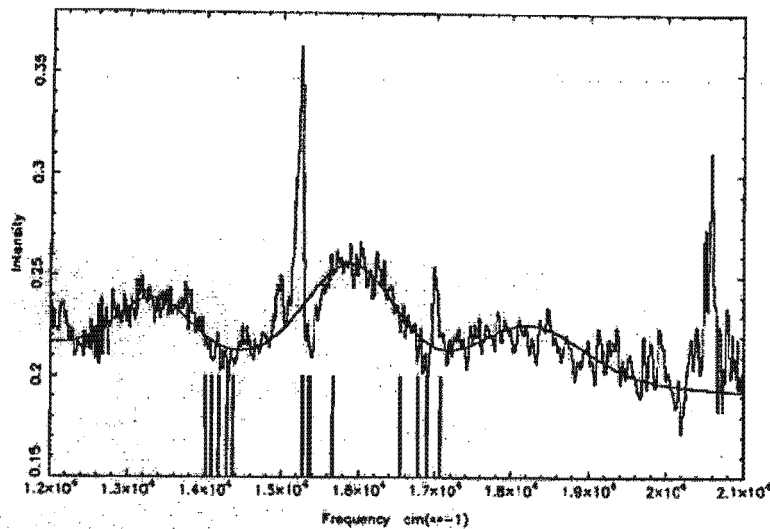
Figure 5.4: Average spectrum of DP Leo for phase ~ 0.75. The smooth curve has Gaussians on a linear continuum, fitted to locate the peak emission wavelength (Cropper et al. 1990).

and 1.5×10^4 cm^{-1}. Using the method described in Wickramasighe, Ferrario, & Bailey (1989) with a temperature of 10 keV & $\theta = 90°$ Osborne et al. (1994) obtain a field strength $B \sim 37$ MG, if the humps correspond to harmonics numbers 4 & 5, and $B \sim 30$ MG for harmonic numbers 5 & 6.

5.4 V834 Cen

Beuermann & Burwitz (1990) obtained a magnetic field $B \sim 22.5 - 23.5$ MG and a temperature $kT = 5 - 10$ keV for V834 Cen. Their best fit to the harmonic spectrum corresponded to the $7^{th} - 10^{th}$ harmonic (see Fig. 5.6). Their model assumed the simple view that the spectrum of V834 Cen consists of an optically thick cyclotron continuum with emission from some optically thin region superimposed. The adjustable parameters in their model were temperature (kT), field strength (B), orbital phase(ϕ_o), orbital inclination (i) and inclination (η) of the accreting field lines with respect to the rotational axis.

Ferrario et al. (1992) obtained an average field strength at the cyclotron emission region of ~23 MG. They found that the best fit to their model (described in Ferrario & Wickramasinghe (1990)) gave an electron temperature $kT = 20$ keV, electron number density $N_e = 3.0 \times 10^{16}$ cm^{-3} and optical depth parameter $\Lambda = 5.9 \times 10^5$. The features at 6300 and 7050 Å can be seen in Fig. 5.7.

5.5 ST LMi

Ferrario, Bailey, & Wickramasinghe (1993) detected broad peaks near 1.42, 1.65 and 2.00 μm in their IR spectra of ST LMi (see Fig. 5.8). All bright-phase spectra (0.75-0.06), when the main accretion region is visible, were summed to create an average bright phase spectrum.

31
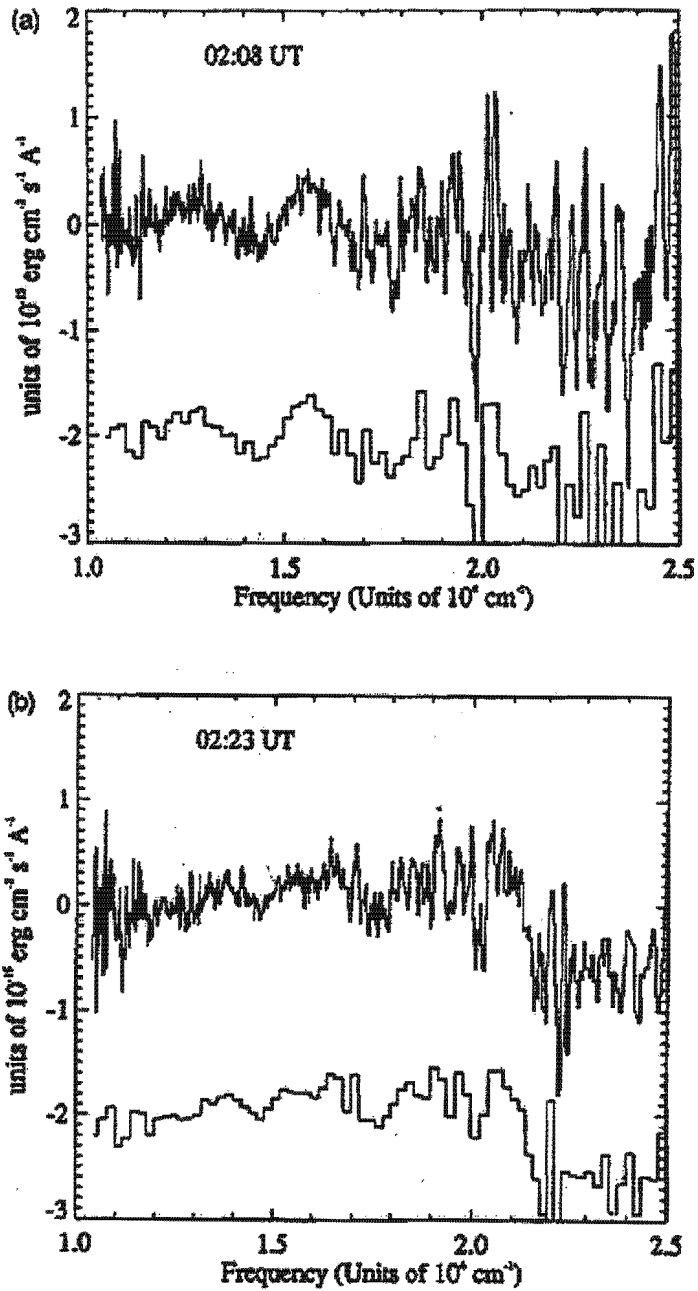
Figure 5.5: Spectra of EV UMa with a low order continuum polynomial and prominent emission lines removed. Prominent humps can be seen, particularly in (a) centred on 1.27×10^4 and 1.56×10^4 cm^{-1} (Osborne et al. 1994).
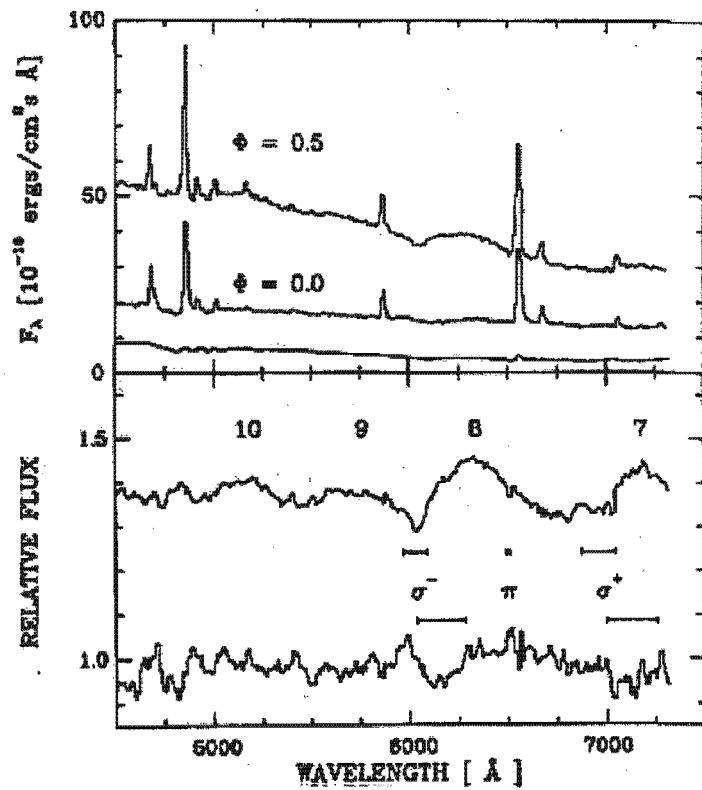
Figure 5.6: Upper panel: high-state spectra of V834 Cen at phases 0 & 0.5. Lower panel: high-state spectra after emission line removal and normalizing. The figure shows the cyclotron harmonics and Zeeman absorption components of $H\alpha$ (Beuermann & Burwitz 1990).
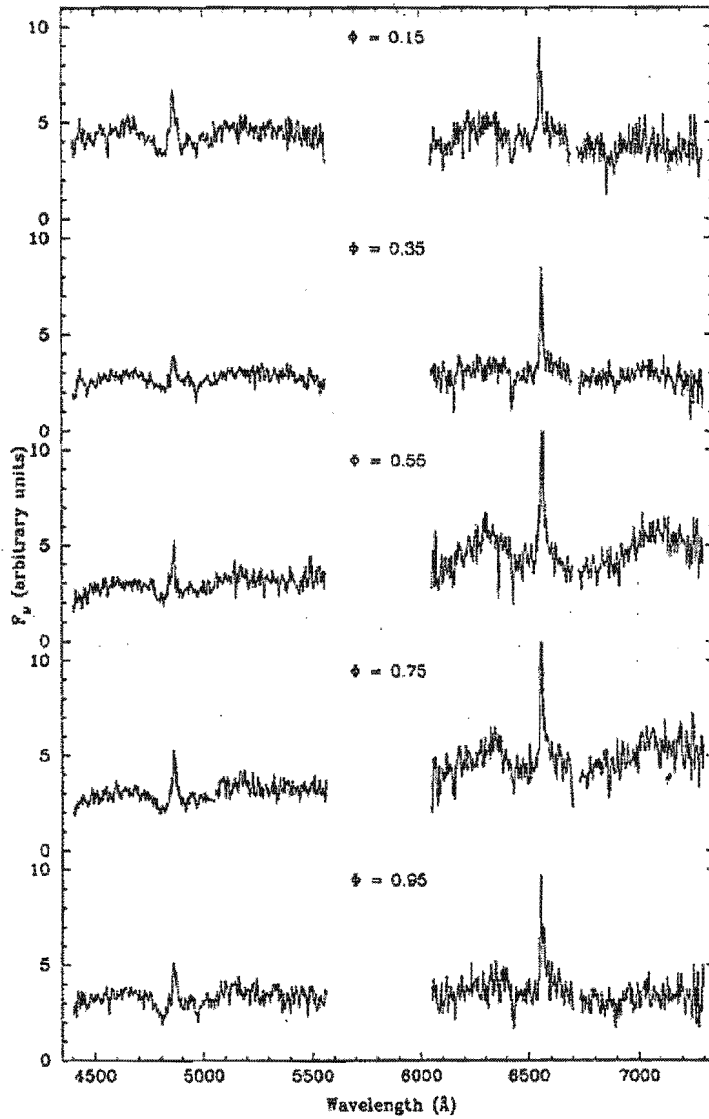
Figure 5.7: Spectra of V834 Cen obtained with the Dual Beam Spectrograph on the ANU 2.3 m telescope. The prominent cyclotron emission features are visible near 6300 and 7050 Å (Ferrario et al. 1992).
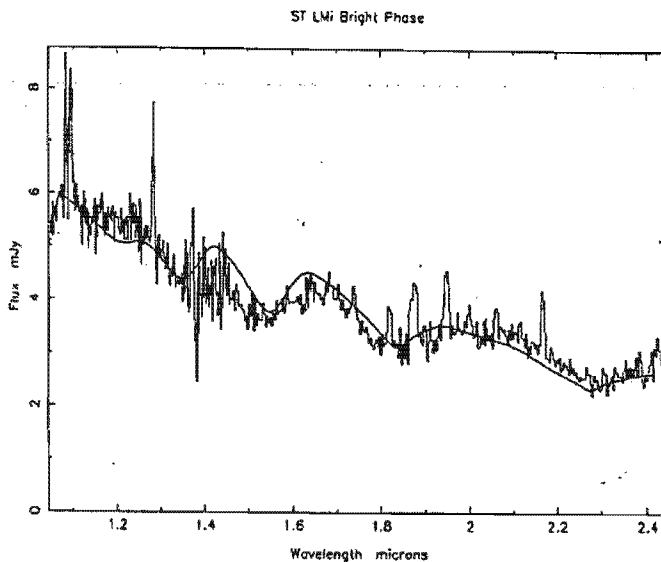
Figure 5.8: Bright-phase spectrum of ST LMi, covering the phase range from 0.75 to 0.06. The solid line is the fit to the data (Ferrario, Bailey, & Wickramasinghe 1993).

A best fit to their model (described in Ferrario & Wickramasinghe (1990)) gave a polar field strength $B_p = 11.5 \pm 0.5$ MG, $\Lambda = 10^5$ and $kT = 10$ keV. They found that models based on uniform emission regions cannot reproduce the observed spectral slope and profiles of the cyclotron emission lines, in particular those of the optically thin lower harmonics. A better fit was obtained by introducing inhomogeneities, allowing for two regions with different opacities along the same accretion arc. This model gave harmonics 6, 5 & 4 at 1.42, 1.61 & 2.08 μm respectively.

5.6 HU Aqr

HU Aqr is the brightest ($V_{mag} \sim 15$) eclipsing polar currently known. The spectrum (upper panel in Fig. 5.9) in the low state shows all the hallmarks of a Polar in the low state; weak emission lines of Hα, TiO bands and the NaI $\lambda\lambda$ 8183,94 absorption line from the M-dwarf secondary (Schwope, Mantel, & Horne 1997).

The continuum flux in the spectra in the lower panel in Fig. 5.9 is modulated with cyclotron emission lines. Schwope, Mantel, & Horne (1997) obtained this spectrum by subtracting a suitable scaled M-dwarf spectrum. They identified intensity maxima at 7800, 6300 and 4600 Å. A best fit to their cyclotron model identified these maxima as the $4^{th} - 7^{th}$ harmonics for an assumed 10 keV plasma with an 80° polar angle and a field strength $B = 37$ MG.

5.7 BY Cam, AN UMa, DP Leo & MR Ser

Cropper (1988) observed the four Polars BY Cam, AN UMa, DP Leo & MR Ser with a low resolution spectrograph and detected cyclotron harmonics in all four systems. He fitted Gaussians to the cyclotron humps to obtain wavenumbers of the peaks. The wavenumbers for the different systems are listed in Table 5.4. The Gaussians were weighted to their

35
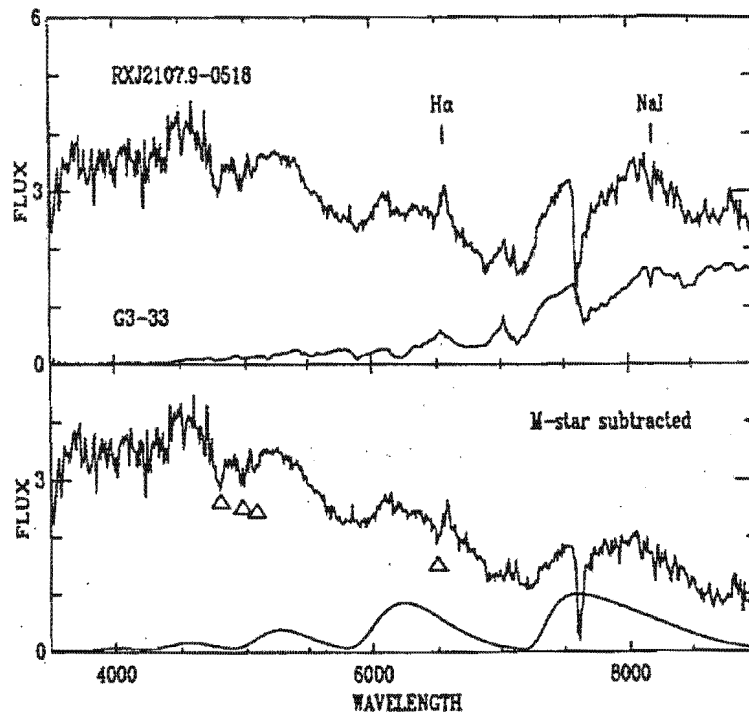
Figure 5.9: Upper panel: low-resolution spectrum of HU Aqr (alias RX J2107.9-0518) and suitably scaled spectrum of the M-dwarf G3-33. Lower panel: same spectrum as above after subtraction of the M-dwarf spectrum. Triangles indicate likely identification of Zeeman absorption troughs (Schwope, Mantel, & Horne 1997).

Table 5.4: Wavenumbers of the cyclotron humps detected in the four systems BY Cam, AN UMa, DP Leo & MR Ser (Cropper 1988). Wavenumbers of cyclotron hump peaks in units cm^{-1}. The weighting for the least squares fits is given in brackets.

	BY Cam	AN UMa	DP Leo	MR Ser
f_n	11857(0.76)	12280(1.00)	13155(0.39)	12886(0.6)
f_{n+1}	13989(0.47)	14852(0.71)	15945(1.00)	14857(1.00)
f_{n+2}	15286(0.57)	17465(0.28)	18567(0.25)	16485(0.63)
f_{n+3}	18964(0.20)	19982(0.27)	20525(0.22)	18614(0.63)
f_{n+4}	20714(0.46)	22923(0.20)	23160(0.40)	20571(0.43)
f_{n+5}	22297(1.00)	-	-	22457(0.15)
f_{n+6}	23989(0.48)	-	-	24143(0.32)

Table 5.5: Best fits to the wavenumbers. n is the harmonic number of the first peak (Cropper 1988).

	H0538+608	AN UMa	DP Leo	MR Ser
n	4	4	4	6
B (MG)	40.8±1.5	35.8±1.0	44.0±1.4	24.6±0.6
$T\sin^2\theta$ (keV)	23±4	6.9±1.8	19.0±3	3.4±0.7

peak height and inversely by their width for a least squares fit to Equation 3.13. The best fits for each system are given in Table 5.5. Figs. 5.10, 5.11, 5.12 and 5.13 are spectra obtained by Cropper (1988) for BY Cam, AN UMa, DP Leo & MR Ser respectively.

5.8 EK UMa

Cropper, Mason, & Mukai (1990) found five cyclotron humps in the spectra of EK UMa as illustrated in Fig. 5.14. The wavenumbers of the line centres of these humps are listed in 5.6. The determined a field strength $B \sim 48$ MG, $T\sin^2\theta \sim 13$ keV and harmonic number $n = 3$ for the the first visible harmonic.

5.9 EF Eri & BL Hyi

Ferrario, Bailey, & Wickramasinghe (1996) obtained echelle spectra for EF Eri giving a

Table 5.6: Wavenumbers of cyclotron hump peaks for EK UMa.

	k cm^{-1}
f_n	12140
f_{n+1}	15470
f_{n+2}	18570
f_{n+3}	21790
f_{n+4}	25000
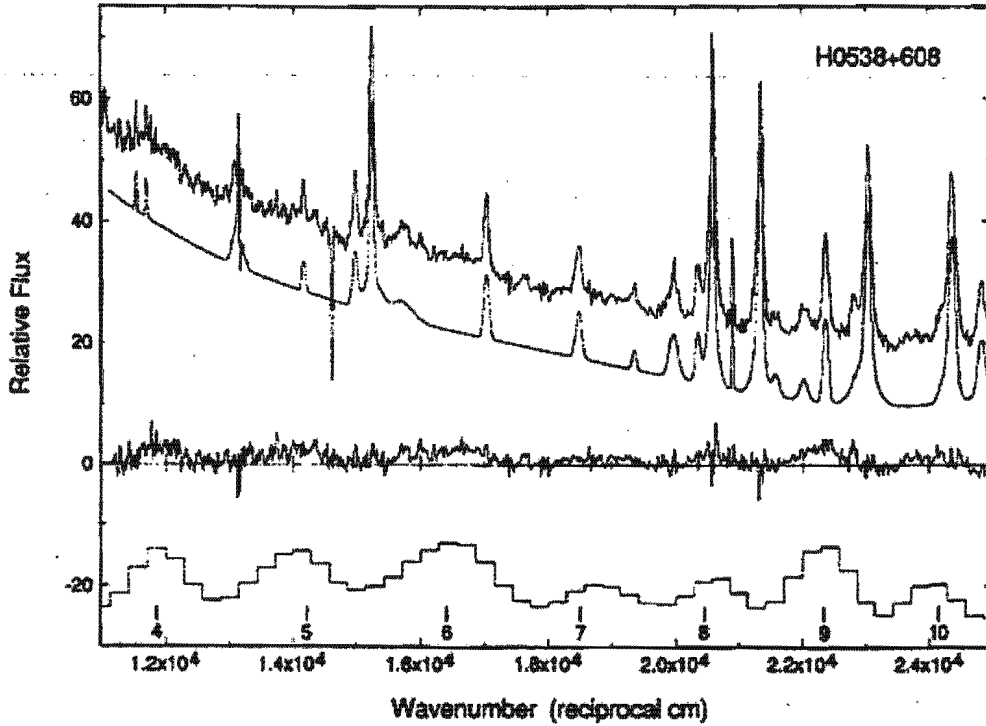
Figure 5.10: The spectrum of BY Cam is shown on top. Beneath the spectrum is a synthesized spectrum of Gaussian emission lines and a low order polynomial continuum. The residual cyclotron spectrum is shown in the third plot. Tick marks indicate the position of the harmonic peaks predicted by equation 3.13 for the best fit parameters in Table 5.5 (Cropper 1988).
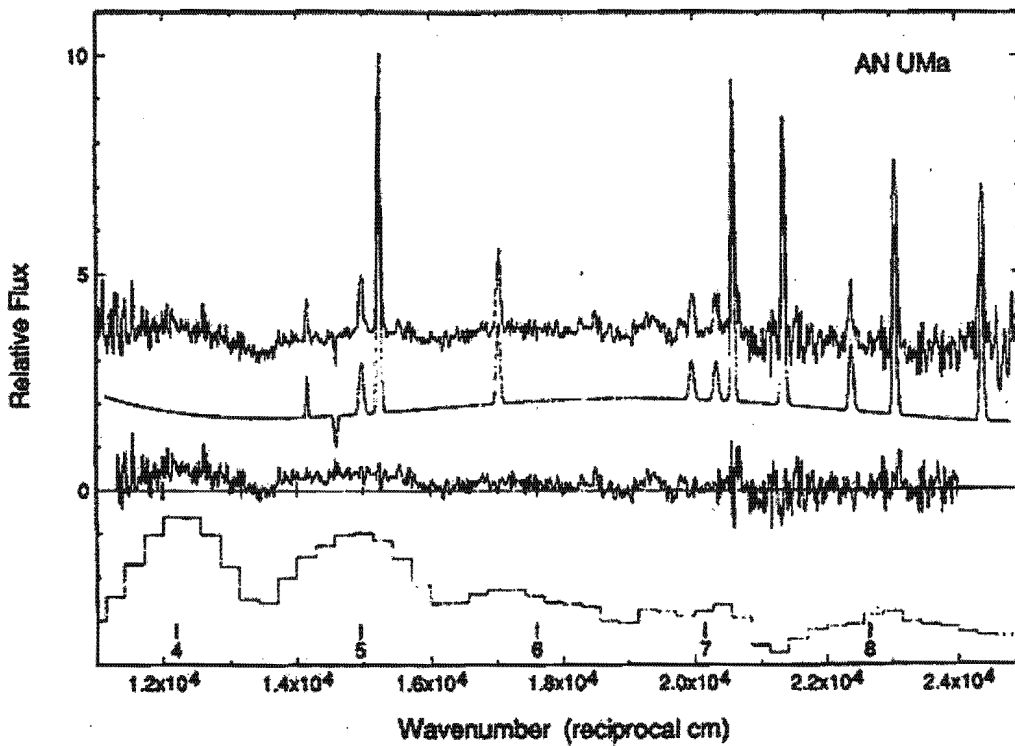
Figure 5.11: As in Fig 5.10 but for AN UMa (Cropper 1988).
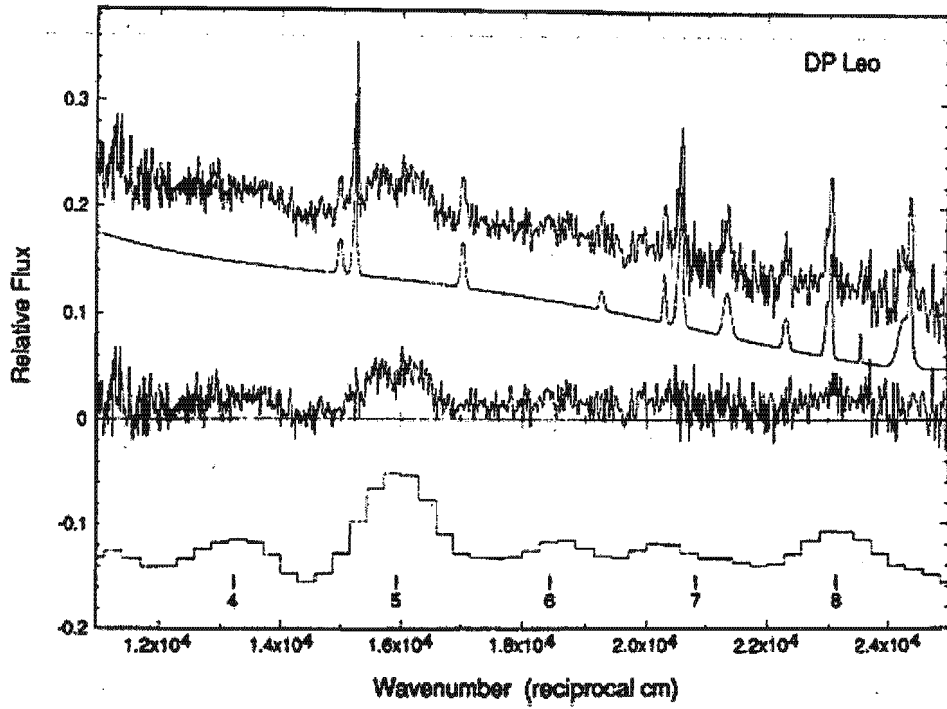
Figure 5.12: As in Fig 5.10 but for DP Leo (Cropper 1988).
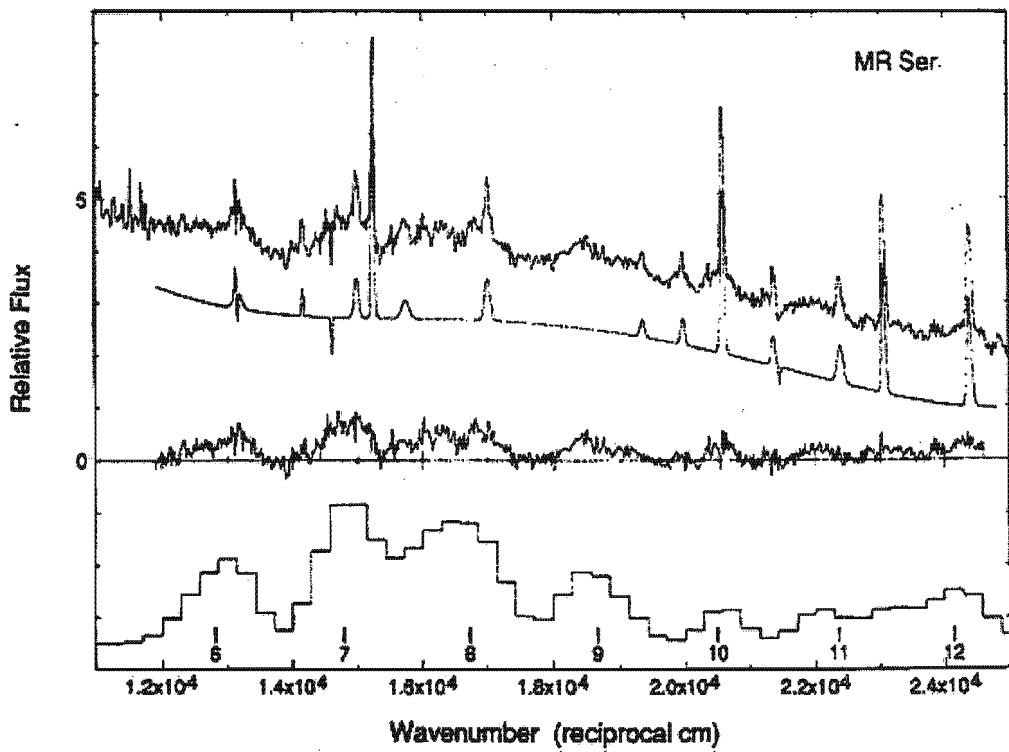
Figure 5.13: As in Fig 5.10 but for MR Ser (Cropper 1988).
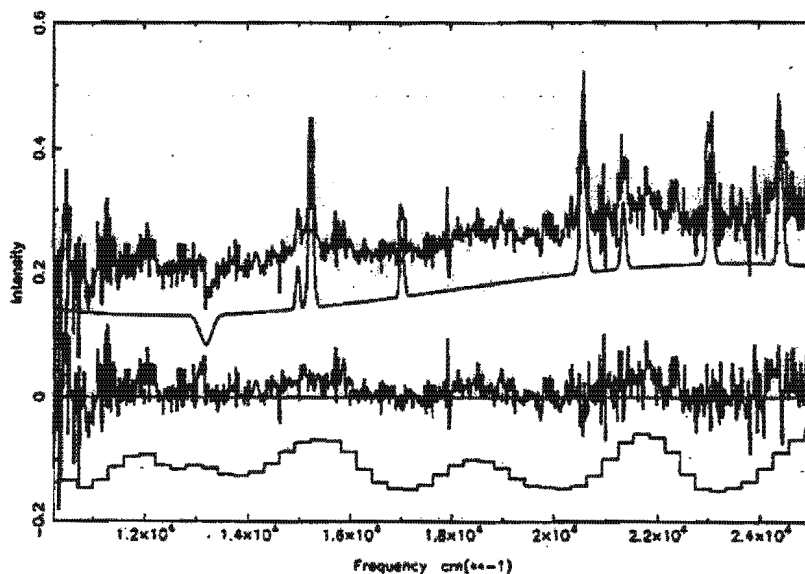
Figure 5.14: Spectrum of EK UMa plotted against wavenumber in cm^{-1} (4000 to 9750 Å) is shown at the top. Beneath is a synthesized spectrum of Gaussian emission lines and low-order polynomial continuum. The residual cyclotron spectrum is shown in the third plot and a binned and smoothed residual spectrum is shown on an expanded vertical scale at the bottom (Cropper, Mason, & Mukai 1990).

wavelength coverage from 0.9 to 2.5 μm. They found cyclotron peaks near 1.05, 1.30, 1.70 and 2.20 μm. A mean EF Eri spectrum is shown in Fig. 5.15. Ferrario, Bailey, & Wickramasinghe (1996) modeled the cyclotron emission assuming a field structure of a centred dipole and the emission region from linearly extended arcs. Their model was adopted to fit an orbital inclination $i = 55°$ and dipole inclination $\theta_d = 150°$ with respect to the spin axis. To fit the data they introduced inhomogeneities by having two regions with different temperatures and opacities along the emitting arc. The model yielded a polar magnetic field strength $B = 16.5$ MG, but the hump near 1.05 μm was not well reproduced. They found that a field strength of 21 MG gave a better fit, but the spacing between humps became too large. They suggested there might be two accreting regions.

Ferrario, Bailey, & Wickramasinghe (1996) used the same model as for EF Eri above to model cyclotron data for BL Hyi. They assumed model parameters $i = 70°$ & $\theta_d = 150°$. The model yielded a field strength $B = 23$ MG. The cyclotron spectrum and best-fitting model is shown in Fig. 5.16. The 23 MG field differs from the 30 MG field deduced by Wickramasinghe, Visvanathan, & Tuohy (1984) from a Zeeman study of this system. Ferrario, Bailey, & Wickramasinghe (1996) interpreted this discrepancy as an indication that the field structure of BL Hyi is probably that of an offset dipole.

5.10 QS Tel

Schwope et al. (1995) found three cyclotron lines centred around $\lambda\lambda$ 3900, 5000 & 7500 Å in their low state spectra (after subtraction of a suitable scaled M-star spectrum) of QS Tel (alias RX J1938.6-4612). Their best fit model yielded harmonic numbers 2-4 in a field strength of B $\approx$ 70 MG. In a state of intermediate brightness Schwope et al. (1995)

40
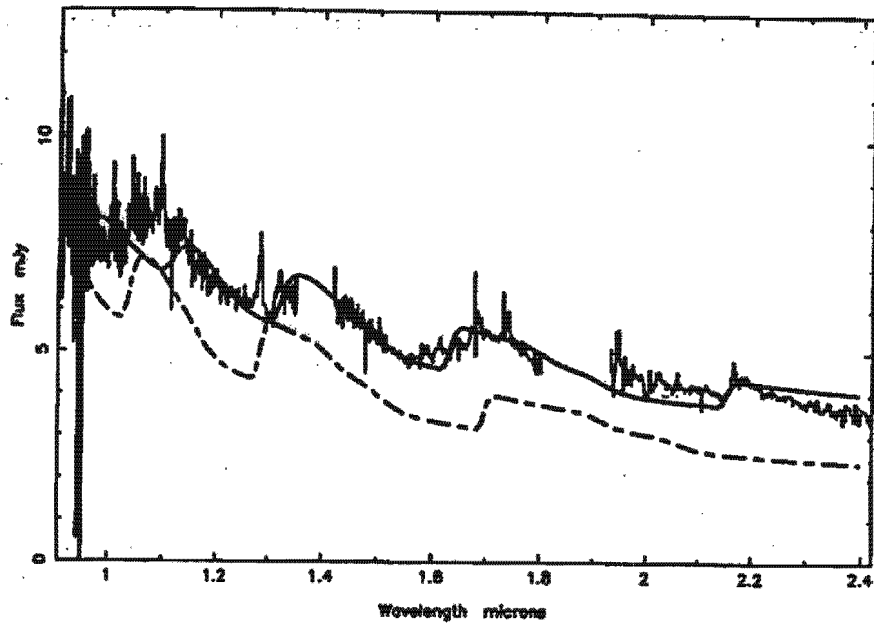
Figure 5.15: AAT spectrum of EF Eri with a best fit model superimposed. The solid and dashed lines correspond to fields of 16.5 and 21 MG, respectively. The data near 1.4 and 1.9 μm have been removed because of the increased noise caused by atmospheric absorption (Ferrario, Bailey, & Wickramasinghe 1996).
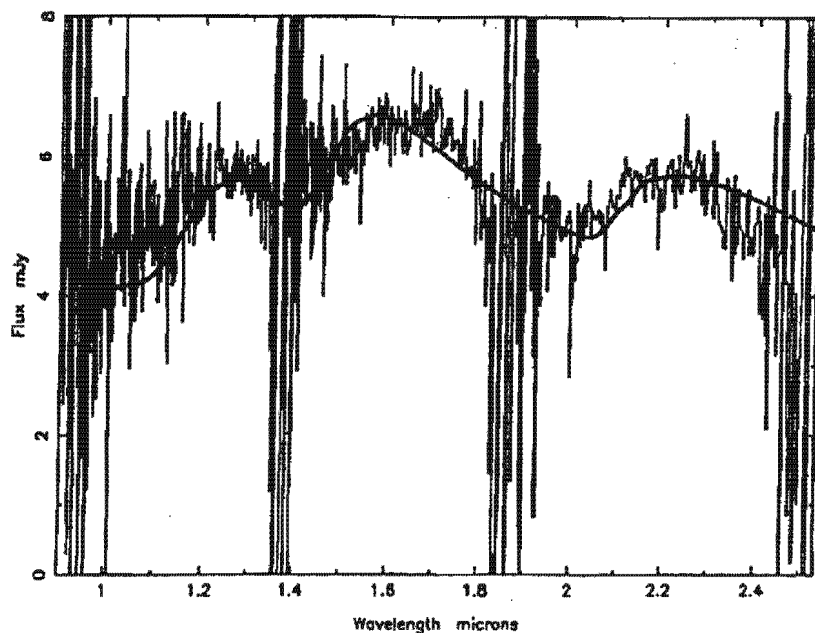
Figure 5.16: AAT spectrum of BL Hyi with a best fit model superimposed. The solid line correspond to a magnetic field strength of 23 MG. The increased noise near 1.4 and 1.9 μm is caused by atmospheric absorption (Ferrario, Bailey, & Wickramasinghe 1996).
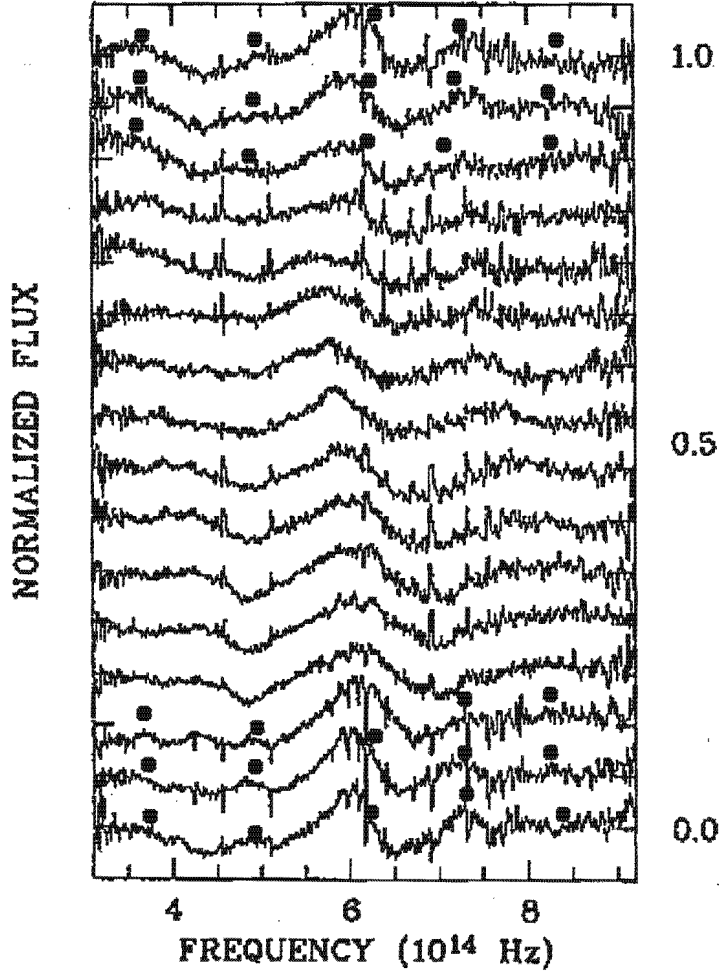
Figure 5.17: Phase resolved cyclotron spectroscopy of QS Tel in the intermediate state. Phases given at the ordinate at the right are rough guides. The dots indicate predicted positions of cyclotron harmonics peaks for the second set of cyclotron (Schwope et al. 1995).

found two independent systems of cyclotron lines. Fig. 5.17 shows the phased resolved cyclotron spectroscopy of QS Tel in the intermediate state. The one system was most pronounced around phase $\phi_{NEL} = 0.3$ (NEL - Narrow Emission Line) with the maxima of the cyclotron emission lines at $\lambda\lambda$ 3750, 5000 & 7500 Å, which corresponds to that of the low state. From these lines they inferred $B_2 = 70$ MG and temperature $kT = 5$ keV. A second system of cyclotron lines was identified only between $\phi_{NEL} = 0.86 - 1.12$. This set of cyclotron humps is marked with dots in Fig. 5.17 and interrupted lines in Fig. 5.18. Modeling this set of cyclotron lines yielded harmonic numbers $n = 3$ - 7 with $B_1 \sim 47$ MG. Ferrario et al. (1994) also detected cyclotron lines in their low-state spectropolarimetric data near 5250 and 6500 Å (see Fig. 5.19). They identified these lines with harmonic numbers $n = 4$ and 3, respectively, in a magnetic field of $B \approx 60$ MG.
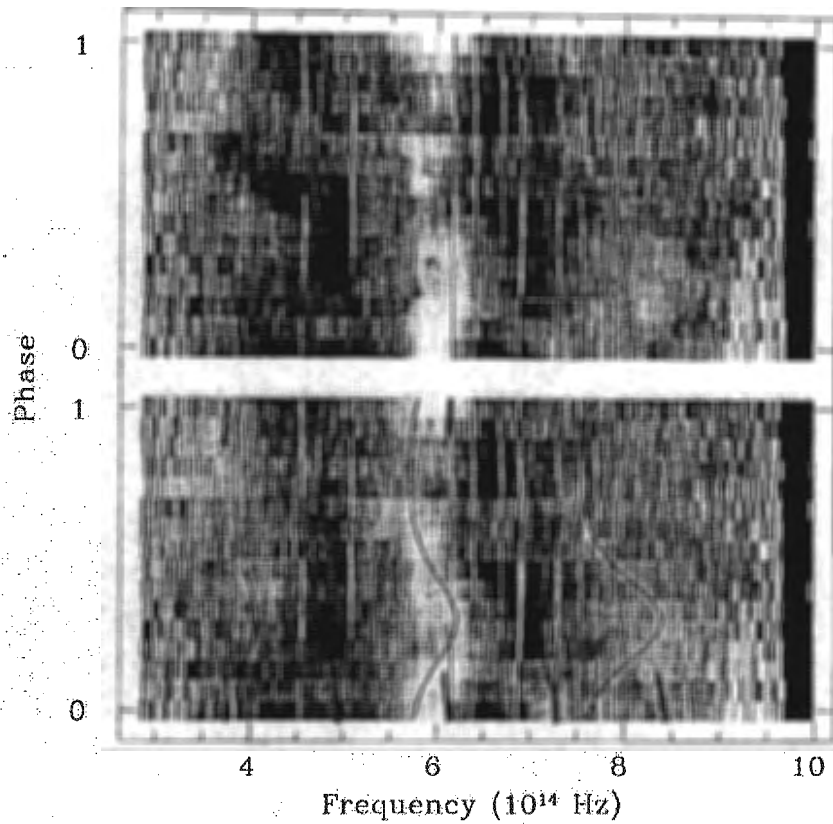
Figure 5.18: Greyscale phase resolved cyclotron spectrogram of QS Tel. The spectra are shown twice for two orbital cycles. The solid lines indicate predicted positions of cyclotron harmonic peaks for the two systems of cyclotron lines (Schwope et al. 1995).
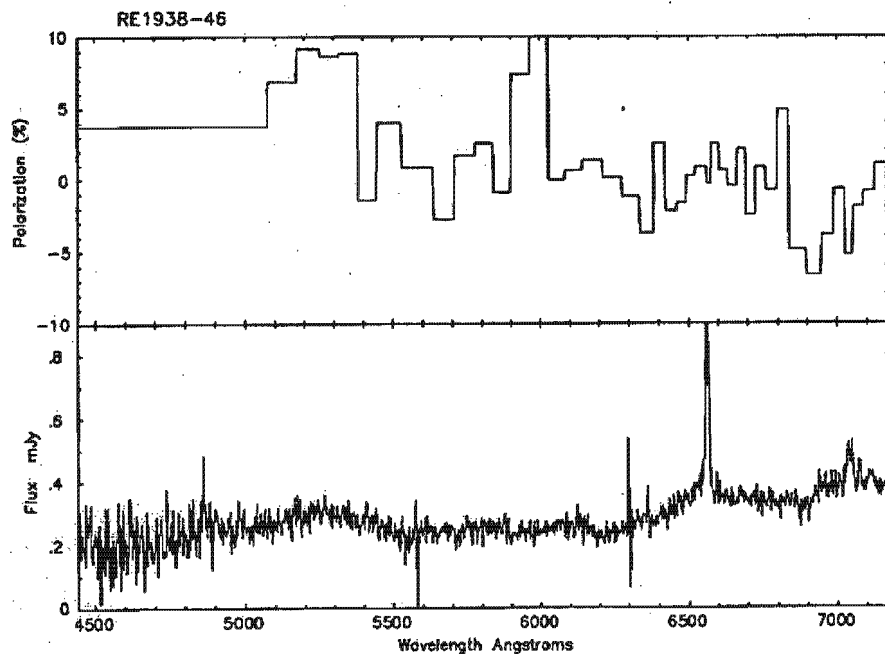
Figure 5.19: Phase-averaged AAT spectra of QS Tel. Upper panel: polarization spectrum. Lower panel: intensity spectrum (Ferrario et al. 1994).
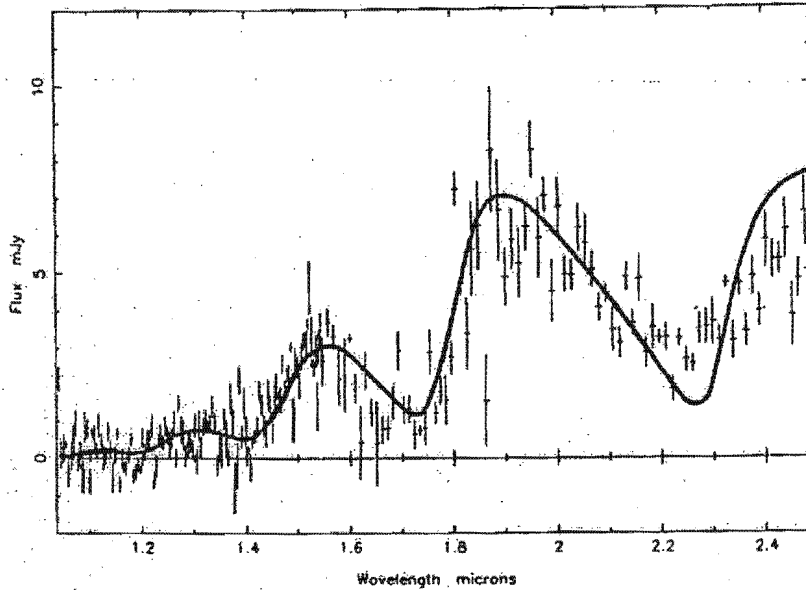
Figure 5.20: The spectrum of AM Her resulting from the subtraction of a faint phase spectrum from a bright phase spectrum. the solid line is a point source cyclotron model with $B = 14.5$ MG, $T_e = 8.5$ keV, $\Lambda = 2.1 \times 10^3$ and $\theta = 65°$ (Bailey, Ferrario, & Wickramasinghe 1991).

5.11 AM Her

Bailey, Ferrario, & Wickramasinghe (1991) identified broad features in their infrared spectra of AM Her near 1.55, 1.9 and 2.5 μm as being cyclotron harmonics. They found that they could fit the cyclotron spectrum using a constant Λ model with a magnetic field strength of $B = 14.5 \pm 0.3$ MG, an electron temperature $kT = 8.5 \pm 0.5$ keV, an optical depth parameter $\Lambda = 1 - 4 \times 10^3$ and viewing angle $\theta = 65° \pm 5°$. According to the model the features at 1.55, 1.90 and 2.5 μm are identified with cyclotron harmonic numbers 5, 4 and 3 respectively. A spectrum resulting from the subtraction of a faint phase spectrum from a bright phase spectrum is shown, together with the best fit cyclotron model, in Fig. 5.20

5.12 RX J1844-741

RX J1844-741 was identified with a $V_{mag} = 16$ CV with an orbital period of $P = 90$ min by O'Donoghue et al. (1993). Later Bailey et al. (1995) obtained detailed phase resolved spectropolarimetry which confirmed that the system emits polarized radiation. Their data showed no resolvable cyclotron harmonics, but from the rise of the continuum toward the red it is likely that the magnetic field strength of this system is $B \leq 25$ MG.

5.13 RX J0531.5-4624

RX J0531.5-4624 is a Polar with an orbital period of $P = 2.22$ hrs, which places it in the period gap for CVs. Reinsch et al. (1994) identified broad cyclotron humps with flux
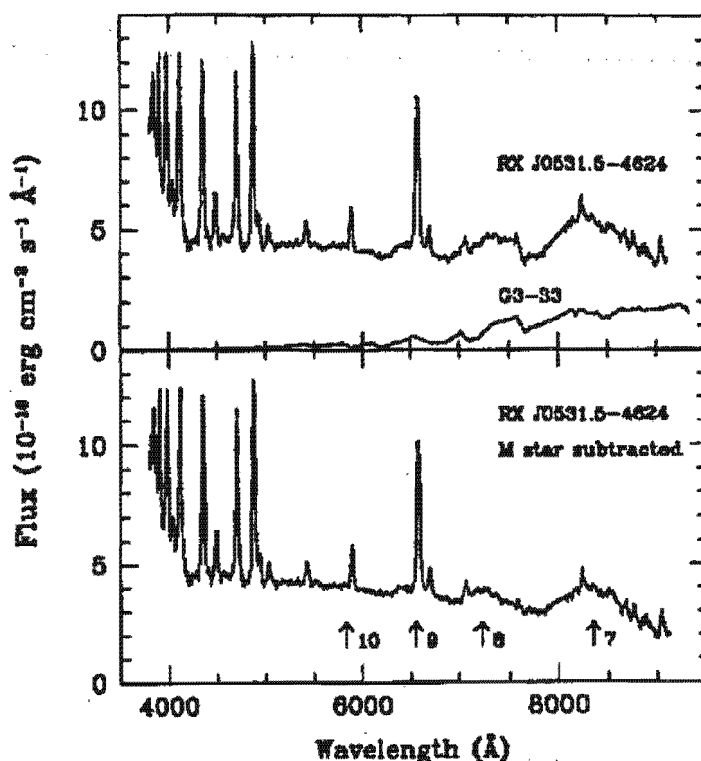
Figure 5.21: Low-resolution optical spectrum of RX J0531.5-4624, and spectrum of the M-dwarf G3-33 (Gl83.1) scaled to match the spectral features of the late-type secondary (upper panel). After subtraction of the M-star component cyclotron lines (harmonics marked with arrows) become clearly evident (lower panel) (Reinsch et al. 1994).

maxima at 8350, 7230, 6550 and 5830 Å in their low-resolution spectra of RX J0531.5-4624. They interpreted these cyclotron lines as being the 7th to 10th harmonics for a magnetic field strength of $B = 19$ MG. The cyclotron spectrum for RX J0531.5-4624 is shown in Fig. 5.21.

5.14   RX J0515.6+0105

With an orbital period of $P \sim 8$ hr, RX J0515.6+0105 is a Polar (Shafter et al. 1995a) with the longest known period, which makes this system particularly important for the studies of conditions and mechanisms for achieving synchronism in magnetic systems. Shafter et al. (1995a) obtained low-dispersion spectra of RX J0515.6+0105 at a variety of orbital phases ($\phi = 0.01$, 0.05, 0.21, 0.052 and 0.67). They subtracted the eclipse spectrum from the out-of-eclipse spectrum in an attempt to distinguish cyclotron harmonics. The out-of-eclipse and eclipse spectra are shown in Fig. 5.22 and the spectrum after subtraction is shown in Fig. 5.23. The resultant spectrum in Fig. 5.23 shows broad features near 5900 and 8500 Å which are interpreted as being cyclotron harmonics. Shafter et al. (1995a) find that, if these features are real, they are roughly consistent with radiation from a $B \sim 61$ MG field, where the second and third harmonics are expected to be centred at wavelengths of 8770 and 5850 Å, respectively, with a fourth harmonic expected to fall
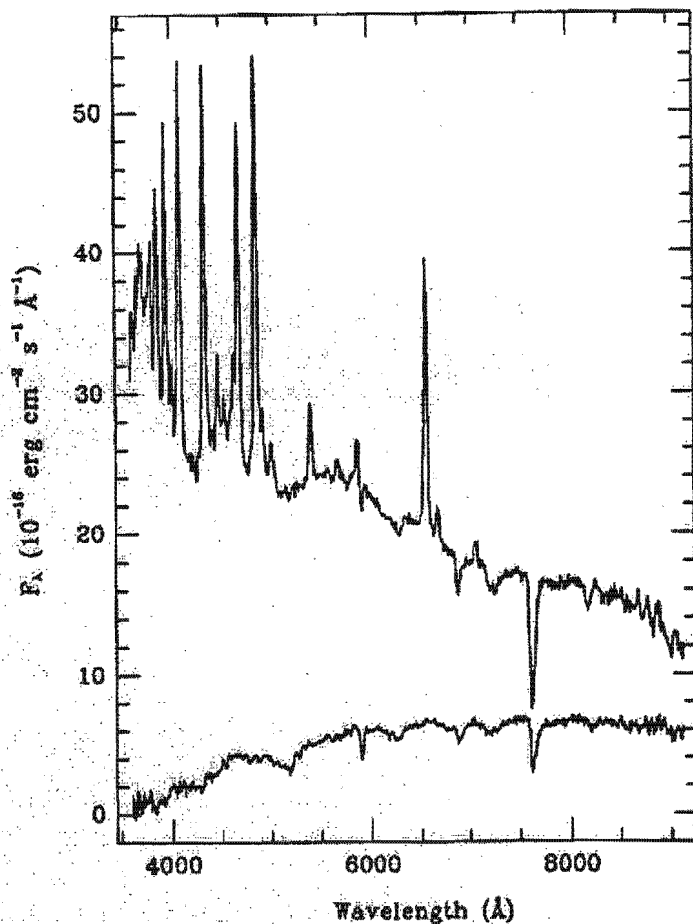
Figure 5.22: Low-dispersion spectra of RX J0515.6+0105. The top spectrum is centred about orbital phase $\phi = 0.21$ and the bottom spectrum is centred about $\phi = 0.01$ (Shafter et al. 1995a).

at ~ 4400 Å. There is a hint of a hump near this wavelength (see Fig. 5.23), but the blending of several strong emission lines makes its identification uncertain.

5.15 RX J1313.2-3259

Thomas et al. (1999) detected cyclotron humps at wavelengths of ~ 5000 & 6600 Å in their spectropolarimetric data. These humps peaked in emission at phase $\phi = 0.2$. From the relative spacing of the humps they estimate a magnetic field strength in the main accretion region to be $B = 52$ MG. Another peak was also detected at ~ 3800 Å with a maximum at phase 0.4, which may indicate a second accretion region on the white dwarf.

5.16 RX J1724.0+4114

Greiner, Schwarz, & Wenzel (1998) identified this $V_{mag} \sim 17$ Polar as being the optical counterpart of the X-ray source RX J1724.0+4114 detected during the RASS. Their photometric observations reveal a period of $P = 119.9$ min, right below the period gap
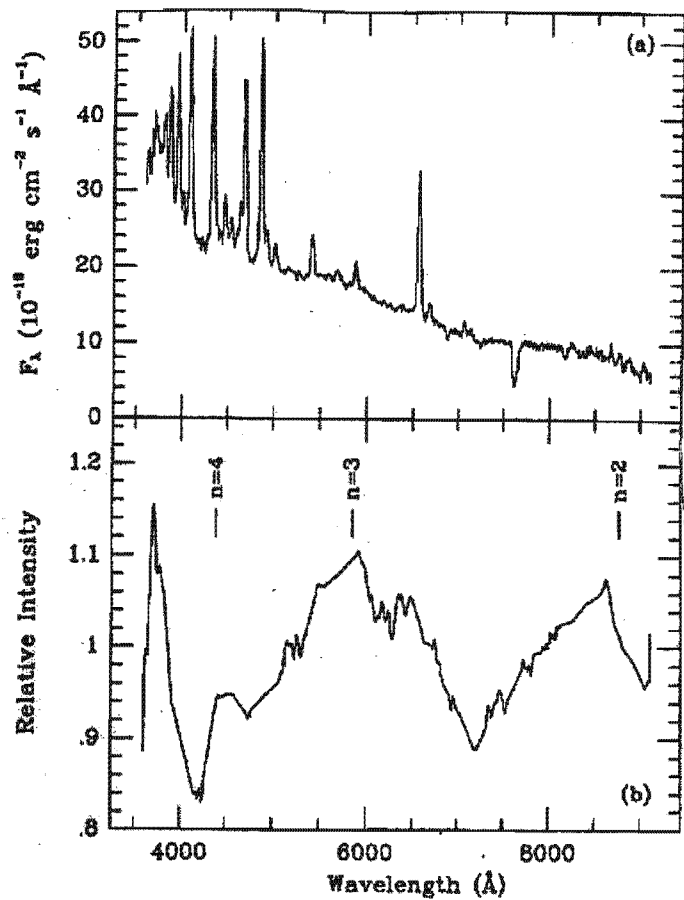
Figure 5.23: The out-of-eclipse spectrum for RX J0515.6+0105 is shown in the upper panel. The same spectrum with the eclipse spectrum subtracted is shown in the lower panel. The position of the 2nd, 3rd & 4th cyclotron harmonics for a 61 MG magnetic field are indicated (Shafter et al. 1995a).
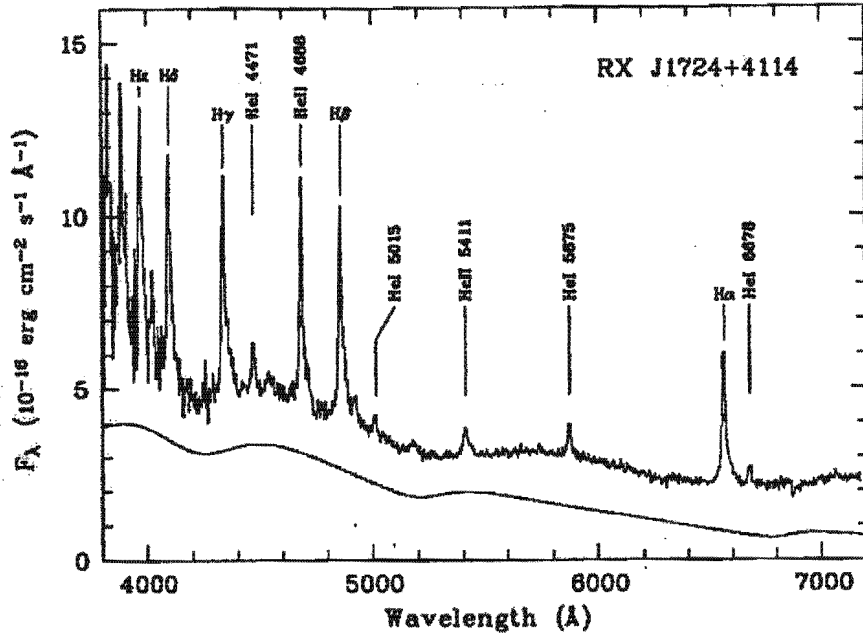
Figure 5.24: Low resolution spectrum of RX J1724.0+4114. The solid line represents a homogeneous cyclotron model for a magnetic field strength of $B = 50$ MG assuming $kT = 20$ keV, $\log \Lambda = 3.5$ and $\theta = 7°$ (Greiner, Schwarz, & Wenzel 1998).

for CVs. Their low-resolution spectrum, shown in Fig. 5.24, shows cyclotron humps at 4500 and 5700 Å. The relative spacing of these lines allows for an interpretation as the $3^{rd}/4^{th}$ or $2^{nd}/3^{rd}$ harmonics in a field of $B = 70/50$ MG respectively. Greiner, Schwarz, & Wenzel (1998) identify the cyclotron lines as the 4th & 3rd harmonics in a $B = 50$ MG magnetic field.

5.17 AX J2315-592

This Polar was identified as the optical counterpart of the X-ray source AX J2315-592, detected serendipitously by the ASCA satellite (Thomas & Reinsch 1996). The system does not show any resolvable cyclotron harmonics, but does show a phase dependent rise in the spectral continuum, toward longer wavelengths. This rise in the continuum is interpreted by Thomas & Reinsch (1996) as being due to optically thin cyclotron emission. A mean faint and bright phase spectrum is shown in Fig. 5.25. Thomas & Reinsch (1996) estimated the magnetic field strength of AX J2315-592 from the turnover frequency (i.e., where the cyclotron radiation changes from being optically thin to optically thick). The turnover frequency depends strongly on the temperature and field strength of the plasma, but only weakly on the geometry of the accretion region. It was calculated that for a turnover frequency of 3.4×10^{14} Hz (as indicated in Fig. 5.26) at a temperature of $kT = 17 \pm 4$ keV the magnetic field strength could not be higher than $B = 17$ MG (Thomas & Reinsch 1996).

48
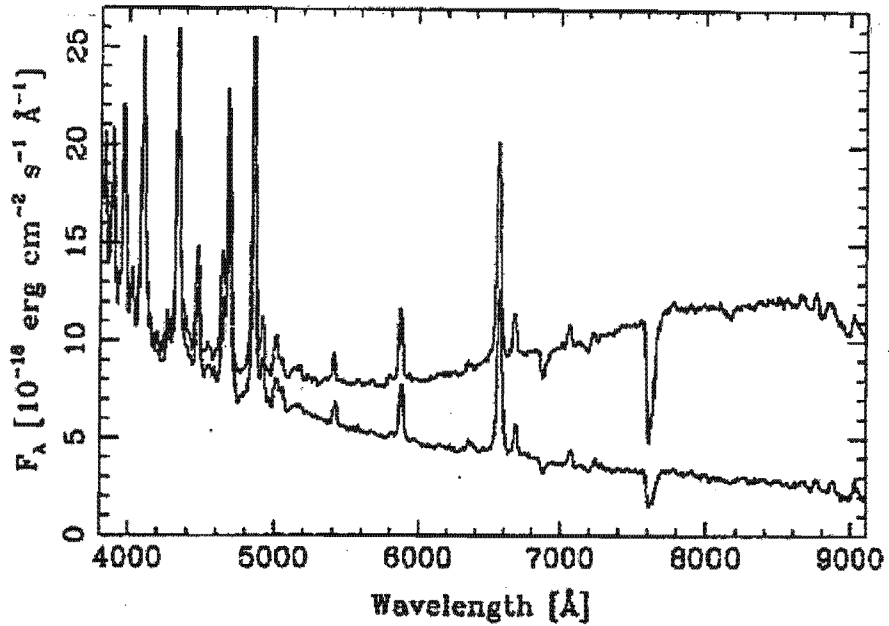
Figure 5.25: Low resolution mean bright phase ($\phi = 0.27 - 0.54$) and faint phase ($\phi = 0.80 - 0.06$) spectra for AX J2315-592 (Thomas & Reinsch 1996).
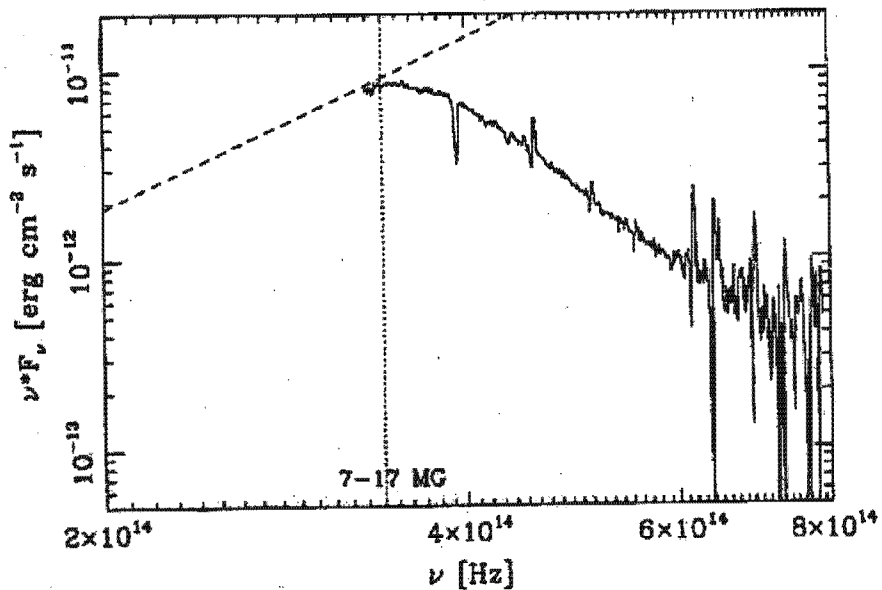
Figure 5.26: Cyclotron spectrum for AX J2315-592 obtained as the difference between the bright and faint phase spectra shown in Fig. 5.25. The dashed line gives a possible Rayleigh-Jeans tail for the optically thick part of the radiation. For the turnover frequency from optically thick to optically thin (dotted vertical line) the corresponding range of magnetic field strengths is given (Thomas & Reinsch 1996).

5.18 EU Cnc

Pasquini, Belloni, & Abbot (1994) obtained three low resolution spectra of the soft ROSAT source EU Cnc (alias G186) in the field of the old open cluster M67. It is the first spectroscopically confirmed Polar found associated with an open cluster. Cyclotron humps are clearly present in the continua of spectra b & c shown in Fig. 5.27.

5.19 EUVE J1429-38.0

The source EUVE J1429-38.0 was discovered serendipitously by the Extreme Ultraviolet Explorer (EUVE) satellite. It has an orbital period of $P \sim 2.5$ hr, placing it in the period gap for CVs. Craig et al. (1996) detected what appears to be weak cyclotron humps, with peaks near 5300 and 5700 Å, in their spectrum of EUVE J1429-38.0. They estimate a magnetic field strength of $B = 20 - 25$ MG, if the features are indeed cyclotron humps. Although Stobie et al. (1997) call into doubt such an interpretation, since Craig et al. (1996) did not remove the M-star secondary features. The discovery spectrum of EUVE J1429-38.0 is shown in Fig. 5.28.

5.20 RX J0203.8+2959

RX J0203.8+2959 was contained in a subsample of sources with a soft X-ray spectrum discovered during the RASS and optically identified as a Polar with a suspected period of $P \sim 3.8$ hr (Schwartz et al. 1998). Schwartz et al. (1998) subsequently showed that RX J0203.8+2959 has an orbital period of $P = 4.6$ hr, making it the third longest orbital period Polar.

In order to search for cyclotron features Schwartz et al. (1998) calculated average bright and faint phase spectra. They removed the contribution of the emission lines and secondary star (i.e. subtracting a M-star template). The final cyclotron spectrum was computed by subtracting the mean faint phase spectrum from the bright phase spectrum. The final spectrum, shown in Fig. 5.29, revealed prominent humps at 7600, 6200 and 5300 Å which Schwartz et al. (1998) identified as the 4th, 5th & 6th cyclotron harmonics. They adapted an isothermal, homogeneous cyclotron model to the data, and found an excellent agreement could be achieve with $B = 38 \pm 2$ MG, $kT = 20$ keV and $\theta = 70°$.

5.21 UZ For

UZ For (alias EXO 033319-2554.2) was discovered as an X-ray source during a systematic analysis of all EXOSAT X-ray data. It is an eclipsing binary with a high orbital inclination, $i \simeq 85°$, and ingress and egress times not exceeding ~ 5 sec (Schwope, Beuermann, & Thomas 1990). The measured radial velocity of curve of the secondary implies a high mass white dwarf $M_{wd} \simeq 1.3$ M$_\odot$ (Schwope, Beuermann, & Thomas 1990), while Bailey & Cropper (1991) obtain $M_{wd} \leq 0.8$ M$_\odot$. Ferrario et al. (1989) identified cyclotron harmonics at 6550, 5400 and 4720 Å in their spectra of UZ For (see Fig. 5.30 & 5.31). They found they could not model the cyclotron peaks considering only a single accretion region. They argue that the cyclotron features can be interpreted in terms of emission
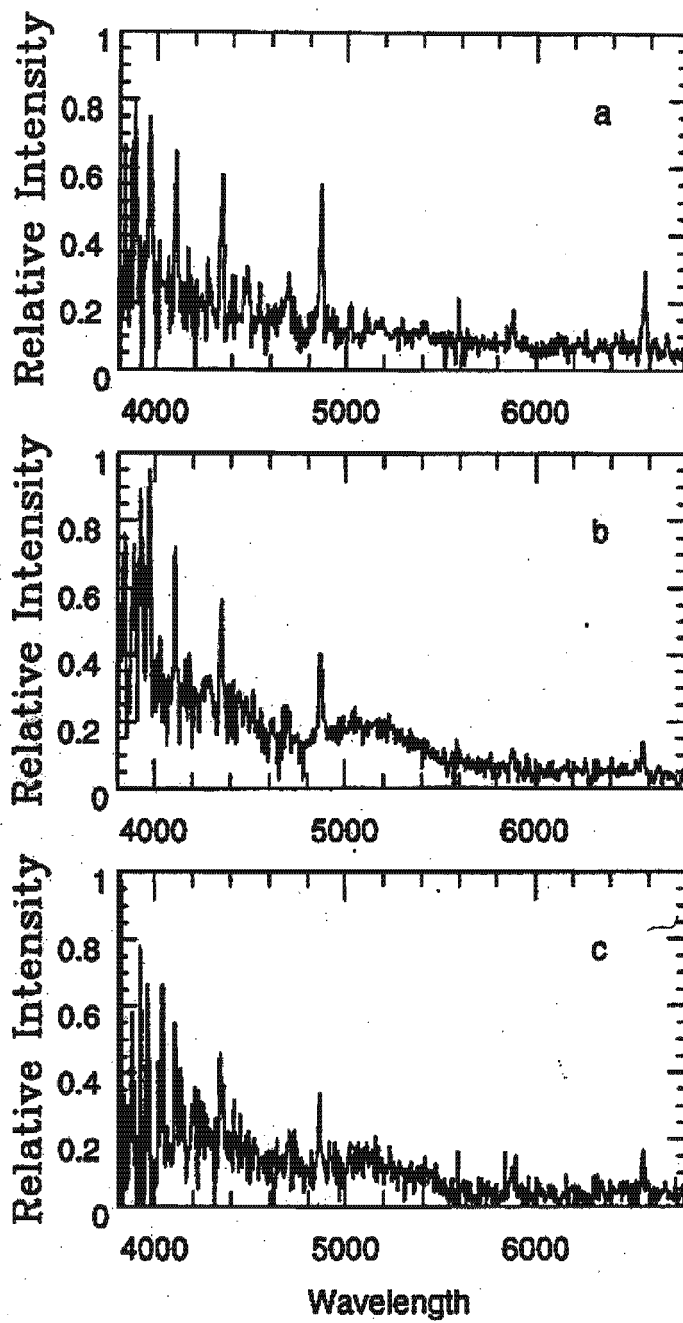
Figure 5.27: Three spectra of the Polar EU Cnc (Pasquini, Belloni, & Abbot 1994).

Figure 5.28: Discovery spectrum of EUVE J1429-38.0 (Craig et al. 1996).

Figure 5.29: Difference of the bright phase and faint phase average spectra. Contributions of the emission lines and the M-star have been subtracted beforehand. The spectra from two different nights are displayed separately. The prominent $4^{th} - 6^{th}$ harmonics are marked. The solid lines represent a cyclotron model for $B = 38$ MG (Schwartz et al. 1998).

Figure 5.30: Spectra of UZ For with the spectra summed and merged into 10 phase bins. Prominent cyclotron line are visible near 5200 and 6550 Å from $\phi = 0.7 - 0.9$ (Ferrario et al. 1989).

from a main region of field strength $B = 56$ MG and $kT = 20$ keV and a second region of field strength $B = 28$ MG & $kT = 10$ keV. Schwope, Beuermann, & Thomas (1990) found that a best fit to their cyclotron data (see Fig. 5.32) yields a magnetic field $B = 53$ MG and temperature $kT = 5 - 10$ keV.

5.22   RS Cae

RS Cae (alias RX J0453.4-4213) has been reported as a Polar with visual magnitude $V_{mag} \sim 19$ by Burwitz et al. (1996). Burwitz (1997) identified cyclotron lines in the spectra occurring at $\sim$7500, $\sim$6100, $\sim$5100 & $\sim$4250 Å as the 4th - 7th harmonics. The cyclotron humps can be seen in the average spectra shown in Fig. 5.33. Their best fit model yields a field strength of $B = 36 \pm 1$ MG with a plasma temperature $kT_{br} = 10$ keV and two possible field geometries: the first case, inclination $i \sim 60°$ and colatitude $\beta \sim 25°$ and the second case, $i \sim 60°$ and $\beta \sim 25°$. RS Cae is one of the rare examples of a Polar where the movement of the cyclotron emission lines can be followed over its entire orbit, this makes it possible to study the accretion geometry in detail instead of using the polarimetric properties as previously applied to other systems (Burwitz 1997). The phase dependent movement of the cyclotron harmonics are represented in the trailed
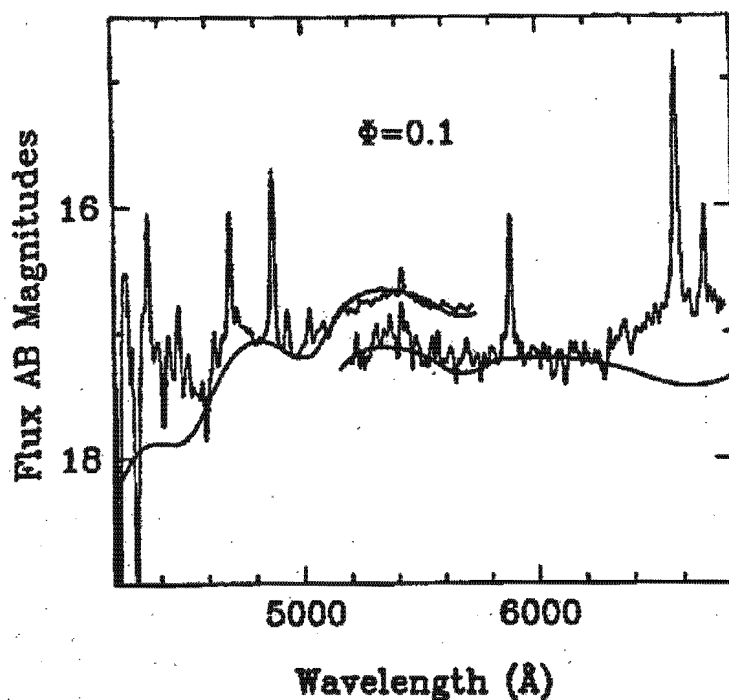
Figure 5.31: Spectra of UZ For at $\phi = 0.1$ showing the cyclotron modulation of the continuum. The two overlapping spectra were obtained on consecutive binary cycles and are displaced by an arbitrary amount for clarity. The solid line represents a best fit model for a magnetic field strength strength (Ferrario et al. 1989).
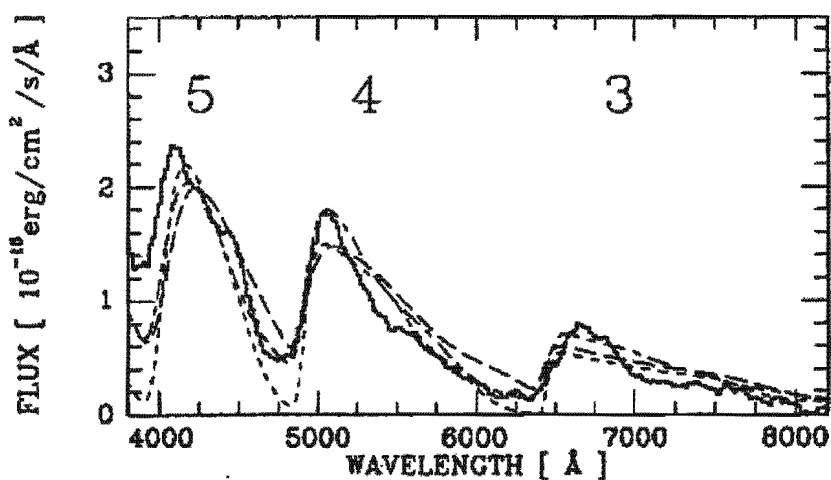
Figure 5.32: Average spectra of UZ For. Results of model calculations are shown with dashed lines (5 keV, 52.5 MG: short dashed lines; 10 keV, 53 MG long dashes); composite spectrum : short-long dashes (Schwope, Beuermann, & Thomas 1990).
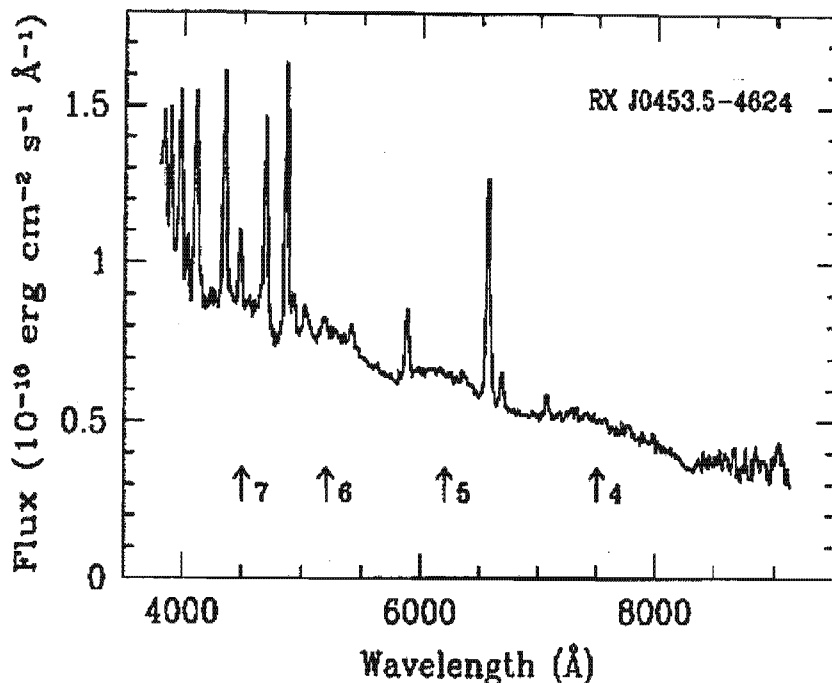
Figure 5.33: Average low-resolution optical spectra of RS Cae. The cyclotron lines have been identified as the 4th to 7th harmonics for a field strength of $B = 36$ MG (Burwitz 1997).

spectrogram illustrated in Fig. 5.34.

5.23 RX J2022.6-3954

RX J2022.6-3954 is a $V_{mag} \sim 19$, short-period (P ~ 78 min), high-field ($B = 67 \pm 2$ MG) Polar. Burwitz (1997) reports that the underlying spectral continuum is flat during the optical dip phase ($\phi \sim -0.5 - 0.5$) and shows broad humps during the bright phase ($\phi \sim 0.15 - 0.30$ and $\sim 0.75 - 0.92$). Fig. 5.35 shows the bright phase and dip phase spectra and a difference spectrum between them which shows the humps more clearly. The humps in the difference is identified with the 2nd, 3rd and 4th harmonics corresponding to a magnetic field strength of $B = 67 \pm 2$ MG.

5.24 RX J0132.7-6554

RX J0132.7-6554 is a Polar with $V_{mag} \sim 20$ with an orbital period $P \sim 77.8$ min (Burwitz 1997). Burwitz (1997) obtained two 12 min exposures of RX J0132.7-6554 in July 1995 and one 40 min spectrum centred on the bright phase and one 30 min spectrum centred on the faint phase in November 1995. The difference spectrum between the bright and faint phase shows cyclotron humps (see Fig. 5.36) which have been identified as the 2nd, 3rd and 4th harmonics corresponding to a magnetic field strength of $B = 67 \pm 2$ MG.
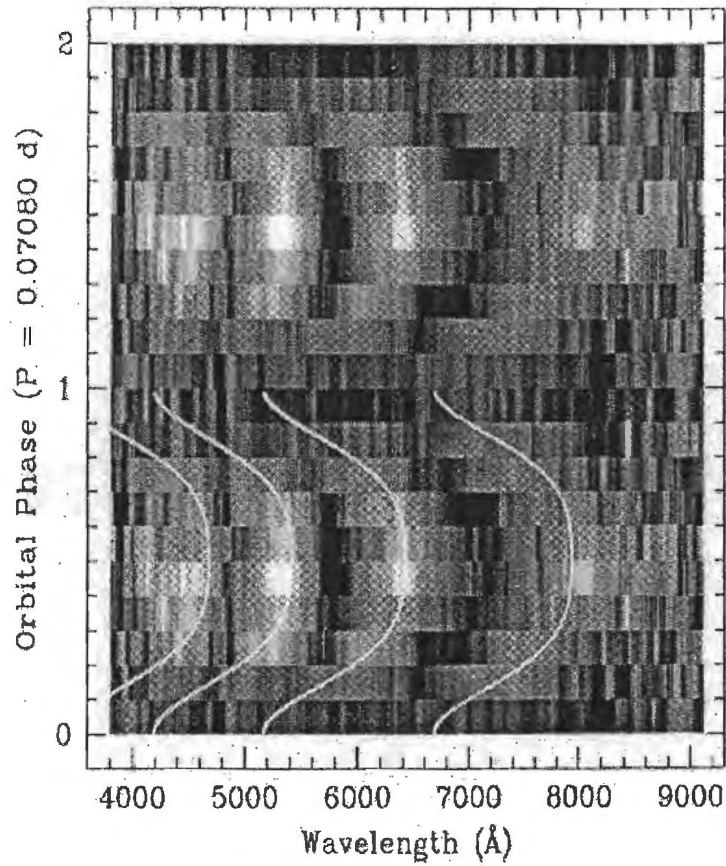
Figure 5.34: Grey scale representation of the cyclotron line emission in RS Cae. the phase dependent movement of the cyclotron harmonics (4th to 7th from right to left) can be clearly seen. The best fit to the phase-dependent positions is superimposed on the lower panel (Burwitz 1997).
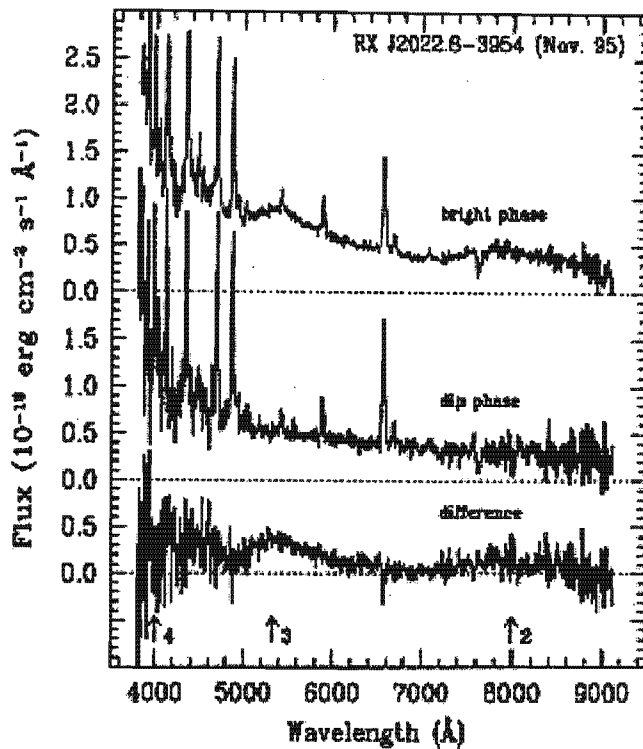
Figure 5.35: Low-state bright-phase, dip-phase, and difference spectra of RX J2022.6-3954 (from top to bottom). The positions of the 2rd, 3rd and 4th cyclotron harmonics expected for a magnetic field strength of 67 MG are marked by arrows (Burwitz 1997).

5.25   RX J1015.5+0904

RX J1015.5+0904 is another short period ($P \sim 80$ min) Polar with $V_{mag} \sim 16.5$. Burwitz (1997) calculated average bright and faint phase spectra from his low-resolution spectra, with a phase coverage of $0.19 \le \phi \le 0.34$ and $0.65 \le \phi \le 0.92$ for the bright spectrum and $0.42 \le \phi \le 0.58$ and $0.93 \le \phi \le 1.07$ for the faint spectrum. The difference spectrum (see Fig.5.37) is basically a smooth continuum with a sharp decline shortwards of ~ 5300 Å which Burwitz (1997) explains as being the contribution of cyclotron radiation from the accretion region. From a fit to the difference spectrum, Burwitz (1997) determined the viewing angle of magnetic field lines, θ, the magnetic field strength, B, and the range of mass flow rates, $\dot{m}$, in the accretion regions. The best fit to the cyclotron spectrum yielded $\theta = 55° \pm 5°$ and $B = 23 \pm 3$ MG.
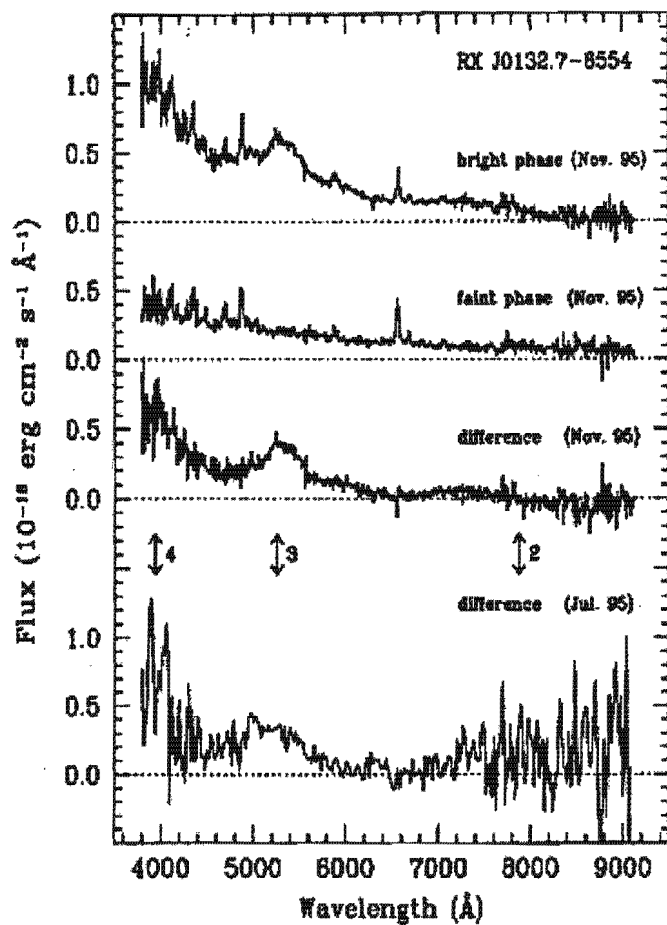
Figure 5.36: Low-state bright-phase and faint-phase spectra and difference spectra of RX J0132-65 for November and July 1995 data (Burwitz 1997).
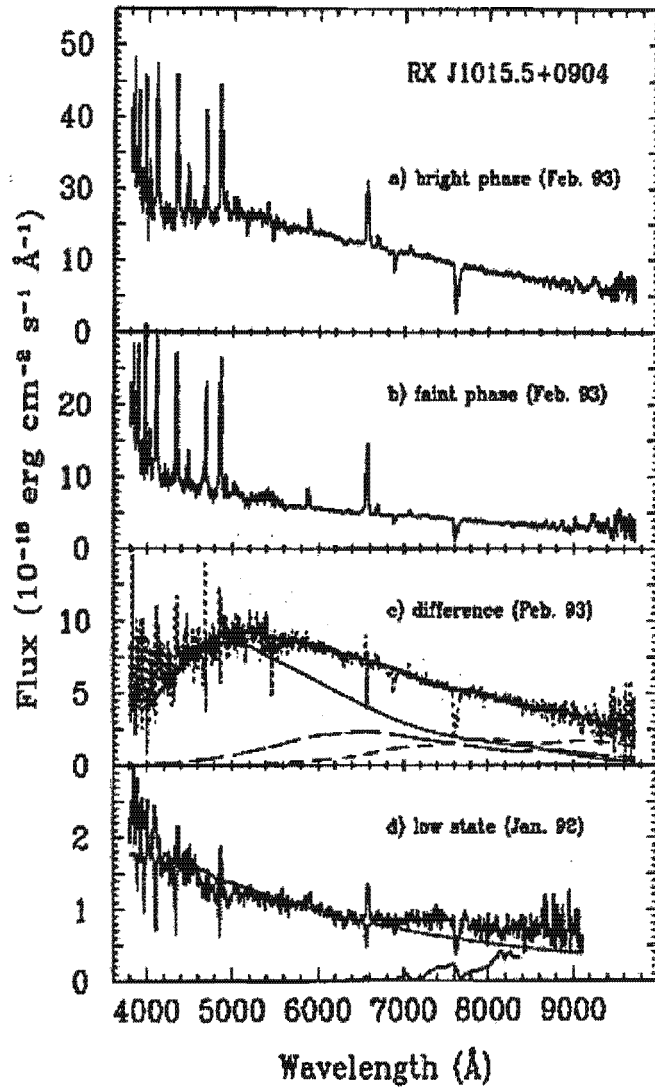
Figure 5.37: Optical spectra of RX J1015+09. (a): average bright phase spectrum (b): average faint phase spectrum (c): difference spectrum of a and b, cyclotron model spectrum for $B = 23$ MG and $\theta = 55°$ (thick solid line), and the contributions from of the individual mass flow rates: $\dot{m} = 0.3$ g cm^{-2}s^{-1} (thin solid line), $\dot{m} = 0.1$ g cm^{-2}s^{-1} (long dashed line) and $\dot{m} = 0.03$ g cm^{-2}s^{-1} (short dashed line) (d): low-resolution discovery spectrum (Burwitz 1997).

Chapter 6

Observations and data reductions

The spectroscopic data used in this thesis were obtained from observations done with the Cassegrain spectrograph (see Section 6.2) which was mounted on the 1.9-m Radcliffe telescope (the largest of four telescopes at the Sutherland station of the SAAO). The aim was to see if new candidate mCVs belonged to the class, and if so, to obtain phase resolved spectroscopy of them, and recently discovered mCVs, which would be used to search for cyclotron features and to conduct radial velocity and Doppler tomographical studies. In addition, limited CCD photometry, which complements some of the spectroscopy, was also obtained. Some known Polars, which have shown cyclotron features, were also observed as test cases, to confirm the techniques for detecting cyclotron features and Doppler tomography.

6.1   Observing campaigns

Four spectroscopic observing runs were undertaken to provide data for this project. Table 6.1 provides information on the spectroscopic observing campaigns undertaken and Table 6.2 lists all the objects observed, some of which do not form part of this thesis. Candidate systems (obtained from the RBS, e.g. Fischer et al. 1998) (see Table 7.14) were monitored, many for the first time, to ascertain whether they where suitable (i.e., bright enough) for further detailed observations. Time resolved spectra were obtained of the most suitable objects.

Table 6.1: A list of spectroscopic observing campaigns.

Date	Observers	No. usable nights out of 7
March 1998	D. Buckley K. van der Heyden	1
August 1998	D. Buckley K. van der Heyden	4
January 1999	K. van der Heyden	6.5
February 1999	K. van der Heyden	4.5
August 1999	K. van der Heyden S. Potter	4

Table 6.2: Log of objects observed over the duration of this thesis. Key for the comments column: H - high state, LS - low state, W - weak emission, VW - very weak emission, TF - too faint.

Object	Date-obs d/m/y	Exp-time s	Grating no.	λ range Å	Res. Å	No. spec	Comments
BL Hyi	20/08/98	900	8	6086-8938	4	4	H
EF Eri	24/01/99	900	12	5202-9140	5	2	W
EUVE J1429-38	24/03/98	900	7	4590-8258	5	1	VW
	20/08/98	900	8	6086-8940	4	7	H
	23/08/98	900	8	6086-8940	4	3	cloudy
EX Hya	29/03/98	300	7	5325-9263	5	1	
	29/03/98	600	7	5325-9263	5	1	
	29/03/98	600	11	7523-9291	2	5	
	29/03/98	900	11	7523-9291	2	6	
	20/02/99	120	6	3630-5555	2	40	H
	21/02/99	300	12	5200-9140	5	26	H
	22/02/99	120	6	3630-5555	2	46	H
	22/02/99	240	6	3630-5555	2	15	H
HU Aqr	20/08/98	900	8	6086-8940	4	9	H
	24/08/98	300	6	3630-5555	2	3	H
	24/08/98	100	6	3630-5555	2	62	H
	24/08/98	300	8	6092-8950	4	41	H
MN Hya	24/01/99	900	12	5202-9140	5	2	VW
QS Tel	17/08/99	900	5	6203-6956	1	14	H
	18/08/99	900	8	6002-8872	4	14	H
	18/08/99	600	6	3567-5492	2	17	H
	19/08/99	600	6	3567-5492	2	32	H
	21/08/99	600	12	5200-9140	5	1	H
	21/08/99	600	12	5200-9140	5	11	H
RBS 0324	19/08/98	900	7	3250-8190	5	1	TF
	23/08/98	600	6	3630-5555	2	1	TF
	19/01/99	900	12	5227-9165	5	7	TF
	20/01/99	900	12	5193-8643	5	5	VW
	21/01/99	900	7	3705-8643	5	14	H
	18/02/99	900	12	5200-9100	5	2	VW
	21/02/99	900	12	5200-9100	5	4	VW
	22/02/98	900	6	5200-9100	2	3	VW

continued ...

Table 6.2 continued

Object	Date-obs d/m/y	Exp-time s	Grating no.	λ range Å	Res. Å	No. spec	Comments
RBS 0372	19/08/98	900	7	3250-8188	5	1	W
	23/08/98	500	6	3630-5555	2	·1	W
	23/08/98	900	6	3630-5555	2	2	
	22/01/99	900	12	5204-9142	5	1	W
RBS 0490	19/08/98	900	7	3250-8188	5	1	H
	23/08/98	900	6	3630-5555	2	2	H
	23/08/98	500	6	3630-5555	2	2	H
	22/01/99	900	12	5204-9142	5	1	H
	18/02/99	900	12	5204-9142	5	1	H
RBS 0541	20/08/98	900	8	6086-8940	4	1	TF
	23/08/98	900	6	3630-5555	2	1	TF
	22/01/99	900	12	5204-9140	5	1	TF
RBS 1955	23/08/98	600	6	3630-5555	2	2	TF
RBS 1969	19/08/98	900	7	5350-9295	5	2	H
	20/08/98	900	8	6086-8940	4	2	H
	21/08/98	900	8	6086-8940	4	1	H
	23/08/98	600	6	3630-5555	2	12	H
RX J1313	21/01/99	600	12	5204-9140	5	1	H
	21/01/99	300	12	5204-9140	5	9	H
	22/01/99	300	12	5204-9140	5	30	H
	21/01/99	600	12	5204-9140	5	1	H
	19/02/99	400	12	5200-9140	5	40	LS
	20/02/99	600	6	5350-5555	2	5	LS
	19/08/99	600	6	3568-5493	2	14	H
	22/08/99	600	6	3580-5493	2	9	H
RX J1940	20/08/98	900	8	6086-8940	4	2	W
	21/08/98	900	8	6068-8940	4	1	W
TW PIC	21/03/98	900	7	5325-9260	5	1	H
UW PIC	22/02/99	900	6	3630-5555	2	1	TF
RX J1957	20/08/98	900	8	6086-8940	4	1	VW

Table 6.2 continued

Object	Date-obs d/m/y	Exp-time s	Grating no.	λ range Å	Res. Å	No. spec	Comments
RX J2115	19/08/98	900	7	5350-9288	5	2	
	17/08/99	900	7	3713-8651	5	7	H
	18/08/99	900	6	3568-5493	2	5	H
RX J0153-59	22/01/99	900	12	5204-9140	5	1	W
	19/08/99	900	6	3568-5493	2	4	H
	20/08/99	900	12	5200-9140	5	4	H
	21/08/99	900	12	5200-9140	5	1	H
RX J0640-24	19/01/99	600	12	5228-9165	5	3	H
	19/01/99	900	12	5228-9165	5	7	H
	22/01/99	900	12	5204-9140	5	1	H
	25/01/99	100	12	3561-9140	5	1	H
	25/01/99	600	6	3561-9140	2	2	H
	25/01/99	300	6	3561-9140	2	23	H
RX J1141	24/03/98	1000	7	4590-8528	5	1	
	29/03/98	900	7	4590-8528	5	15	
RX J1610+03 (RBS 1563)	28/03/98	600	7	4670-8608	5	2	
	28/03/98	1200	7	4670-8608	5	3	
	29/03/98	900	7	5325-9263	5	2	
	30/03/98	1200	7	5330-9268	5	3	
	24/08/98	900	6	3630-5555	2	1	VW
RX J1712-24	29/03/98	600	7	5325-9263	5	2	H
	29/03/98	300	7	5325-9263	5	3	H
V347 Pup	22/01/99	900	12	5204-9140	5	1	H
	22/01/99	300	12	5204-9140	5	2	H
	23/01/99	300	4		1	67	H
	21/02/99	900	12	5200-9140	5	4	H
	22/02/99	900	6	3630-5555	2	30	H
V348 Pup	22/02/98	900	6	3630-5555	2	2	W
V834 Cen	24/03/98	900	7	4590-8528	5	4	H
	24/01/99	300	12	5202-9140	5	20	H
	25/01/99	140	6	3561-5493	2	9	H
	25/01/99	300	6	3651-5493	2	17	H

continued ...

Table 6.2 continued

Object	Date-obs d/m/y	Exp-time s	Grating no.	λ range Å	Res. Å	No. spec	Comments
VV Pup	24/03/98	900	7	4590-8528	5	1	LS
	29/03/98	900	7	5325-9263	5	3	LS
	21/01/99	900	12	5204-9140	5	2	H
VZ Scl	19/08/98	900	7	5350-9293	5	1	VW
	19/08/98	900	7	3810-8748	5	1	VW
	20/08/98	900	8	6086-8940	4	1	VW
	23/08/98	900	6	3630-5555	2	1	VW
	24/08/98	900	8	6092-8948	4	1	VW
WGA1802+18	2/03/98	900	7	5325-9263	5	1	
WGA-N	19/08/98	1200	7	3250-8188	5	1	
WGA-NN	19/08/98	500	7	3250-8188	5	1	
WGA-SE	19/08/98	600	7	3250-8188	5	1	
WGA-SS	19/08/98	600	7	3250-8188	5	1	
WGA0053-S	19/08/98	600	7	3250-8188	5	1	
WGA0053-W	19/08/98	1000	7	3250-8188	5	1	
WGA0053-W	19/08/98	900	7	3250-8188	5	1	
RX J0501-03	22/01/99	900	12	5204-9140	5	1	W
	18/02/99	900	12	5200-9140	5	2	W
RX J0512-72	18/02/99	900	12	5200-9140	5	1	W
RX J1015	18/02/99	900	12	5200-9140	5	1	TF
	20/02/99	900	6	3630-5555	2	2	TF
RX J0515+01	19/02/99	900	6	3630-5555	2	9	
	20/02/99	900	6	3630-5555	2	5	
	21/02/99	900	12	5200-9140	5	4	

Table 6.3: Gratings information

Grating No.	Lines mm^{-1}	Å mm^{-1}	Useful Range	Blaze (1st order)	Resolution Å
4	1200	50	800	4600	1
5	1200	50,20	800,350	6800	1,0.5
6	600	100	1600	4600	2
7	300	210	3200	4600	5
8	400	155,75	2300,1150	7800	4,2
9	830	65,30	960, 480	7800	1.5,0.7
10	1200	50	800	10000	1
11	1200	100	1600	10000	2
12	300	210	3200	10000	5

6.2   Instrumentation - the Cassegrain Spectrograph

Previously this instrument used a 100 mm collimated beam and an f/1.4 Maksutov-Cassegrain camera with an Intensified Reticon Photon Counting System (RPCS) as the detector. The spectrograph was adapted in August 1996 to take a *SITe* CCD chip, using an f/2.2 camera with an 86 mm beam. Most spectrograph functions are automated and operated from the warm room. Grating angle adjustment, slit width adjustment, comparison arc & filters choices are not automated. The star is acquired viewing the sky via a mirror, which is then moved to permit light to reach the slit area which is viewed via a transfer lens. The CCD is controlled by a Sun Sparcstation 10 using CHRISTO, a GUI program (written by J.W. Menzies). At the end of an exposure the data are stored in FITS format on disc. The field viewing system is mounted on XY slides, and allows autoguiding on stars which are bright enough and located between 3' and 7' from the target object.

The *SITe* CCD is effectively 266×1798 pixels in area, with 15 μm pixels, and is usable over wavelengths ranging from 3500 to 10000 Å. Between 6000 and 10000 Å, fringing effects produced by interference become progressively more severe with increasing wavelength, and flat fields need to be obtained at the exact grating angle used for an observation. The *SITe* CCD is run in frame transfer mode, i.e., a mask is placed over half the chip and at the end of an exposure the image formed in the unmasked half is shifted to the masked half, whence it is read out during the next exposure of the unmasked half.

The scale of the slit is 6 arcsec/mm, and for optimal through-put a slit width of 500 μm should be used (O'Donoghue & Smit 1999). Cu/Ar and Ne arc lamps are used for comparison spectrum. The following star filters are available: neutral densities up to 10 magnitudes, BG39 and GG495 order separating filters. Nine gratings (see Table 6.3), at different blaze angles and resolutions, are also available.

The *SITe* CCD offers improved sensitivity over the RPCS, especially in the red. Fig. 6.1 & 6.2 shows the comparison of the performance of the *SITe* CCD with that of the *RPCS* over a spectral range 3500-7500 Å. A sensitivity measure was obtained by observing the same objects (under similar conditions) with both instruments and comparing their fluxes. The *SITe* CCD sensitivity is greater by more than a factor of five in the blue and increases to over a factor of fifty in the red/near-IR (O'Donoghue 1999). Had it not been
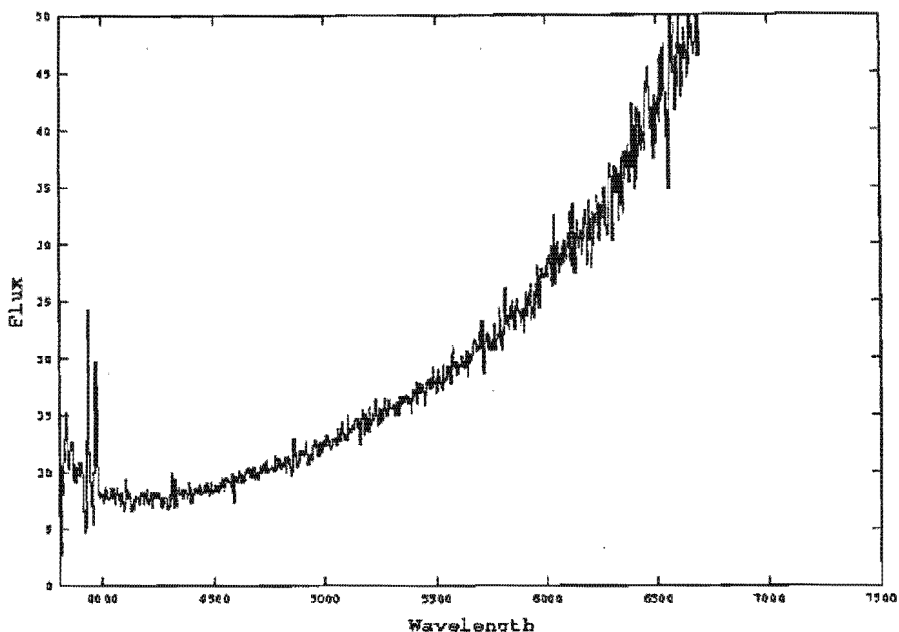
Figure 6.1: A comparison of the sensitivities of the *SITe* CCD versus that of the RPCS detector. Plotted here is the flux obtained using the *SITe* CCD divided by that obtained with RPCS, versus wavelength.

for this improved red sensitivity of the *SITe* CCD over the RPCS this program would not have been possible at the SAAO, where detection of red cyclotron features was an important aspect of the project.

6.3 Data reduction

All the spectral data were reduced using the Image Reduction and Analysis Facility (I-RAF) which is a product of the National Optical Astronomy Observatories in the USA.

All CCD images were bias subtracted, to remove the DC level that is added during readout, and flat fielded to correct for pixel-to-pixel variations, vignetting effects and fringing. Dome flats (i.e., a halogen lamp illuminating a reflective screen) were used to correct for the pixel-to-pixel variations while twilight sky exposures were obtained (when conditions allowed) in order to determine the slit illumination function, i.e., how the intrinsic sensitivity of the instrument varies in the spatial direction (perpendicular to the slit). The object spectrum was extracted as follows: at each point along the dispersion axis the data within the extraction aperture are summed and the sky background is subtracted. The spectrum is then wavelength calibrated by assigning dispersion solutions to the object spectrum. The dispersion functions are obtained by identifying emission lines in extracted comparison lamp exposures (either an argon, or neon lamp, depending on the wavelength range). Telluric features (from the Earths atmosphere) were removed by observing smooth spectrum standards (essentially simple line-free early spectral type stars) and then dividing the object spectra by the normalized (to unity) smooth standard spectrum (Bessell 1999). The spectra are then flux calibrated using observations of
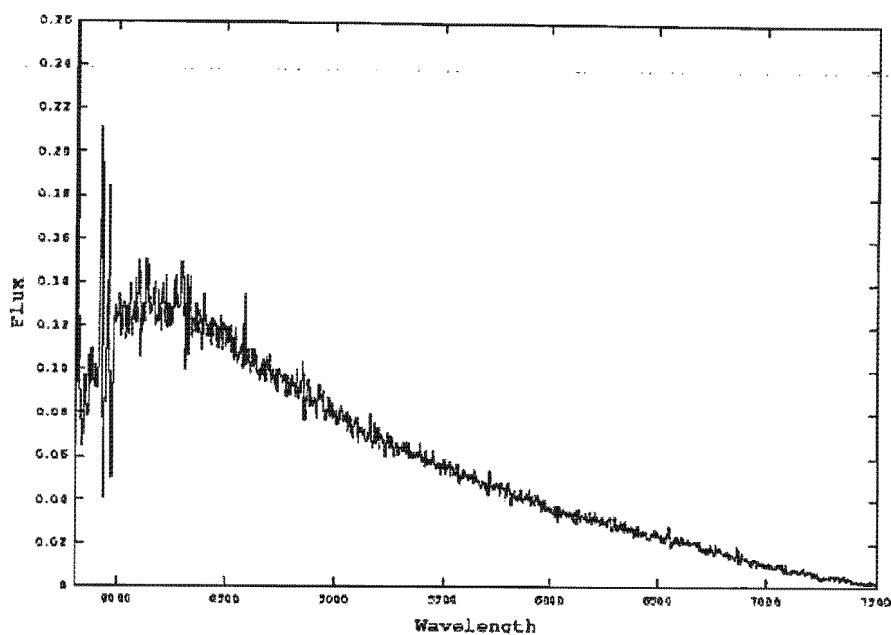
Figure 6.2: Same as for Fig. 6.1, but with the RPCS flux divided by the *SITe* CCD flux.

spectrophotometric standard stars. Fluxes obtained this way are accurate to about 20%.

6.4 Data Analysis

6.4.1 Magnetic field indicators

6.4.1.1 HeII λ4686Å

Magnetic CVs, and Polars in particular, show strong HeII emission lines. The presence of HeII λ4686 emission means two things: (a) there is a strong enough ionizing continuum shortward of the HeII λ228 Å edge (b) there is a line-emitting cloud (or clouds) of gas exposed to this source.

Pure disc accretion in a CV seems to have a difficulty generating strong continuum in the range short-ward of 228 Å, the disk itself is probably never hot enough (except in high $\dot{M}$ novalikes), plus the disc is in a poor position to irradiate itself or the secondary. Polars show strong HeII λ4686 since the soft X-ray component (before interstellar absorption) is very strong in the range 50-228 Å, and the stream and the secondary are favorably irradiated by the soft component (Mukai 1999). Silber (1992) put forward an empirical criterion for magnetic CVs: The equivalent width of Hβ should be greater than 20 Å and the ratio HeII λ4686/Hβ should be greater than 0.4 (although there are other non-magnetic CVs e.g., some novalikes, that obey this criterion). The results of HeII λ4686 emission are discussed in Section 7.

6.4.1.2 Cyclotron harmonics

Even though the cyclotron humps are obvious in the raw spectra of some objects, (e.g. Fig. 6.3 for VV Pup) the spectra usually need to be carefully reduced before the humps
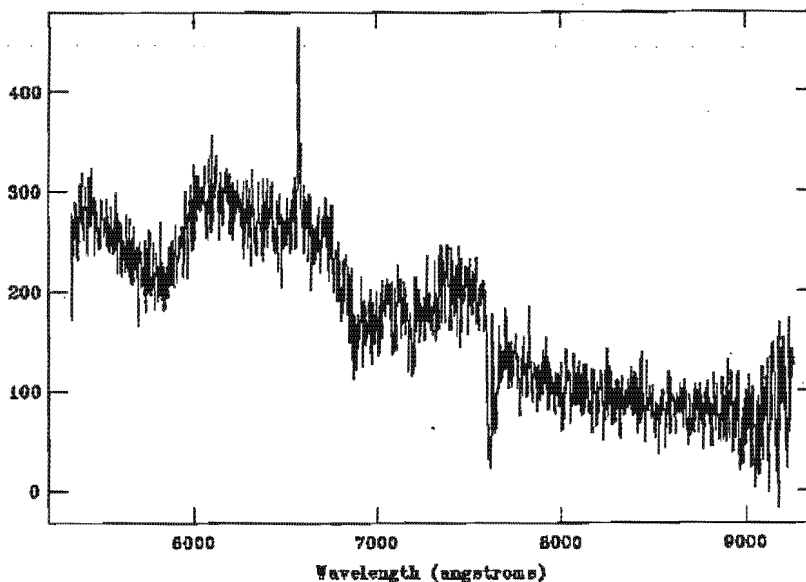
Figure 6.3: Spectrum of VV Pup obtained in March 1998. Plotted are counts versus wavelength. Cyclotron humps can be seen clearly in the continuum, even though the data are not flux calibrated.

are visible. All prominent emission lines are usually removed. This is because the measurement of the position and amplitude of the cyclotron humps is complicated by the the presence of emission lines. The most successful method for the removal of the emission lines usually involves fitting each line with one or more Gaussian profiles. The full spectrum is then fitted with a low-order polynomial which, together with the Gaussian profiles, is subtracted from the spectra. This leaves the cyclotron humps as residuals (e.g. Schwope & Beuermann 1997). The data can also be binned to coarser resolution and smoothed to produce the final spectra.

In self-eclipsing systems a mean faint phase could be subtracted from the spectra, but care must be taken not to introduce residual features in the data. VV Pup for example, shows two-pole accretion and the humps from the second pole are shifted during the bright phase (Schwope & Beuermann 1997). Subtracting the faint phase in this case would thus obviously lead to erroneous results. Suitably scaled K or M-star spectra must also be subtracted in some systems to remove secondary-star features. Here again care must be taken not to introduce spurious features.

The broad cyclotron humps in the spectra can be approximated by Gaussians. The wavenumber, or wavelength, of the line centres can then be used in (3.13) to obtain the parameters n, B and $T\sin^2\theta$. Since electron temperature is the major contributor to broadening, the FWHM can also give some indication of the plasma temperature. The presence of cyclotron features is discussed in Chapter 7.

6.4.2   Radial velocity curves

Radial velocity measurements were obtained using up to three methods: 1) Fitting Gaussians to the emission lines to obtain the line centres, 2) Gaussian convolution, and 3)

Cross-correlation. Gaussian or, in some cases, multiple Gaussians fits, were made to the emission lines using the SPLOT routine in IRAF to determine the centroid wavelength. The wavelength shifts, $\delta\lambda$, with respect to the rest wavelength, λ_0, correspond to Doppler velocities, $\delta v = \frac{\delta\lambda}{\lambda_0}c$ which describe the projection of the true orbital motion onto the line-of-sight toward the observer. One difficulty in using this method is that it is not always possible to distinguish, and thus measure, the different line velocity components.

The FXCOR routine in IRAF was used to determine radial velocities by performing Fourier cross-correlation on a set of object and template spectra. The continua in both object and template spectra were removed and rebinned to $\log\lambda$ (i.e., constant velocity bins) scale before cross-correlation. Template spectra were created by averaging a sequence of Doppler corrected (i.e., shifted to zero radial velocity) object spectra. In addition, a template spectrum similar in spectral type to the secondary star can be used to determine its radial velocity.

Radial velocities were also determined using the Gaussian convolution scheme of Schneider & Young (1980b) supplied by the RVEL routine in the MOLLY software package (by T. Marsh). Positions of the emission line peak were obtained by convolution of the data with a single Gaussian K, given by :

$$K(x) = xe^{(-x^2/2\sigma^2)} \tag{6.1}$$

where σ is the Gaussian standard deviation. Positions of the emission line at various positions from the line centres (e.g. the base) can be obtained by convolution of two Gaussians, given by :

$$K(x) = e^{-(x-a)^2/2\sigma^2} - e^{-(x+a)^2/2\sigma^2} \tag{6.2}$$

where a is the separation of the two Gaussians. The parameters σ and A can be varied to probe different velocity points in the line profiles. In practice what we solve is :

$$\sum_{i=1}^{N} f_i K(i - \lambda) = 0 \tag{6.3}$$

where f_i are the data and λ is the line centre that we are computing (Schneider & Young 1980b). According to Schneider & Young (1980b), this method is very well conditioned for low signal-to-noise ratio data. This method is also appropriate for blended, multi-velocity component, lines. The results of radial velocity studies are discussed in Chapter 7.

Chapter 7

Results on individual systems

In this chapter I report on the two Polars HU Aqr and QS Tel, which were observed as test cases to confirm the techniques of Doppler tomography and cyclotron spectroscopy respectively. Observations of the new magnetic systems RX J1313-32, RX J1141-64, RX J1610+03, RX J0153-59, RX J0501-03, RX J0512-72 and RX J0515+01 are presented. More detailed observations were obtained for RX J1313-32 and RX J1141-64, and thus a more detailed analysis of these objects are is presented. I present the results of RBS 0324, RBS 0372, RBS 0490 & RBS 1969, which were selected from the RBS as possible mCVs. Table 7.1 provides a brief summary of observations obtained of these objects. Heliocentric Julian dates are given only when times series spectroscopy was obtained. Further details on individual objects can be found in Table 6.2.

Table 7.1: A brief observing log of individual objects.

Date-obs	Object	Grating no.	HJD range 2450000+	Phase coverage	λ range Å	Res. Å
March 1998	RX J1141.3-6410	7	902.3812 - 902.5424	0.88 - 2.11	5400-9200	5
	RX J1610+03	7			5400-9200	5
Aug 1998	RBS 1969	7			5400-9200	5
		6			3600-5600	2
	RBS 0372	7			3600-7200	5
	RBS 0490	7			3600-7200	5
	HU Aqr	6	1050.3258 - 1050.4317	0.31 - 1.53	3600-5600	2
		8	1050.4381 - 1050.6027	0.6 - 2.5	6300-8600	4
Jan 1999	RBS 0324	12	1200.3047 - 1200.4609	0.23 - 1.47	5400-9200	5
		7			3500-7200	5
	RX J1313-32	12	1200.5762 - 1200.6154	0.33 - 0.56	5400-9200	5
			1201.4953 - 1201.6451	0.59 - 1.45		
	RX J0501-03	12			5400-9200	5
Feb 1999	RX J1313-32	12	1228.4594 - 1228.6474	0.04 - 1.11	5400-9200	5
	RX J0512-72	12			5400-9200	5
	RX J0501-03	12			5400-9200	5
Aug 1999	RX J1313-32	6	1410.2166 - 1410.3181	0.07 - 0.66	3568-5568	2
			1414.2232 - 1414.2952	0.02 - 0.43		
	QS Tel	5			6200-6956	1
		8	1409.2398 - 1409.3857	0.7 - 2.2	6000-8872	4
		6	1409.4073 - 1409.5343	0.44 - 1.74	3570-5492	2
			1410.3421 - 1410.5876	0.06 - 2.58		
		12			5200-9140	5
	RX J0153-59	6			3568-5493	2
		12			5200-9140	5
	RX J0153-59	6			3568-5493	2
		12			5200-9140	5

7.1 HU Aqr

HU Aqr was identified as the optical counterpart of the RASS X-ray source RX J2107.9-0518 by Schwope, Thomas, & Beuermann (1993) and Hakala et al. (1993). In its high accretion state HU Aqr is the brightest ($V_{mag} \simeq 15$) among 6 known eclipsing systems. The orbital period is $P = 125$ min, close to the lower edge of the period gap, with the eclipse lasting 9.75 min (Schwope, Mantel, & Horne 1997). HU Aqr was observed as a test case to confirm the techniques for Doppler Tomography.

7.1.1 Observations

Time resolved spectroscopy of HU Aqr was obtained on two separate nights during the August 1998 observing run. Eight 900 s integrations, and forty one 300 s integration, covering a wavelength region $\sim 6086 - 8950$ Å were obtained on 20 & 24 August 1998 respectively. A sequence of 63 blue spectra giving a wavelength coverage $\sim 3630 - 5555$ Å with integration times of 300 s for the first three spectra and 100 s for the remainder, was obtained on the 24 August 1998. See Tables 6.2 & 7.1 for a full observing record. The reduction process is detailed in Section 6.3.

7.1.2 Emission lines and Radial velocities

A mean combined blue/red orbital spectrum of HU Aqr is shown in Fig 7.1. HU Aqr shows all the lines usually found in Polars (viz. H-Balmer lines and lines of neutral and ionized Helium). The emission lines are multi-component in nature and one can resolve up to three line components (viz. narrow emission line component (NEL), high velocity component (HVC) and broad 'base' component (BBC)). The NEL is the most prominent line component and together with the BBC is visible throughout the orbital cycle, except during the eclipse phase. The HVC component is only resolvable in our data at phases centering ~ 0.2 & 0.7.

Gaussian fits were made to the HeII λ4686 emission line, in order to determine the radial velocities of the different emission line components. The HeII λ4686 was selected because the emission line components are best seen in this line. The emission lines were fitted with two Gaussians in order to fit the NEL and BBC. No attempt was made to fit the HVC since this component can only be resolved at certain phases. An attempt was also made to fit the radial velocities of Hβ, Hγ, Hδ & HeII λ4686 using the Gaussian convolution scheme. Eight Gaussians filters with separations of 2000, 1500, 900, 700, 500, 200, 100 km s^{-1} and corresponding Gaussian FWHM of 400, 250, 200, 200, 200, 200 & 200 km s^{-1} were used and the data were phase folded using the ephemeris from Schwope, Mantel, & Horne (1997). The amplitude (K-velocity), systemic velocity (γ-velocity) and phase offset (ϕ_0) were determined for each of the radial velocity curves using a nonlinear least-squares algorithm.

The radial velocity variation of the NEL and BBC determined from Gaussian fits is illustrated in Fig. 7.3. The NEL radial velocity curve deviates from a pure sinusoid at phase intervals $\phi \sim 0 - 0.2$ and $\phi \sim 0.7 - 1$. A similar effect is seen in the NEL radial velocity curve of Schwope, Mantel, & Horne (1997). This effect can be understood from the HeII λ4686 trailed spectrogram shown in Fig. 7.2, where a sine wave for the NEL radial velocity parameters is overplotted. It can be seen that the NEL is only resolvable
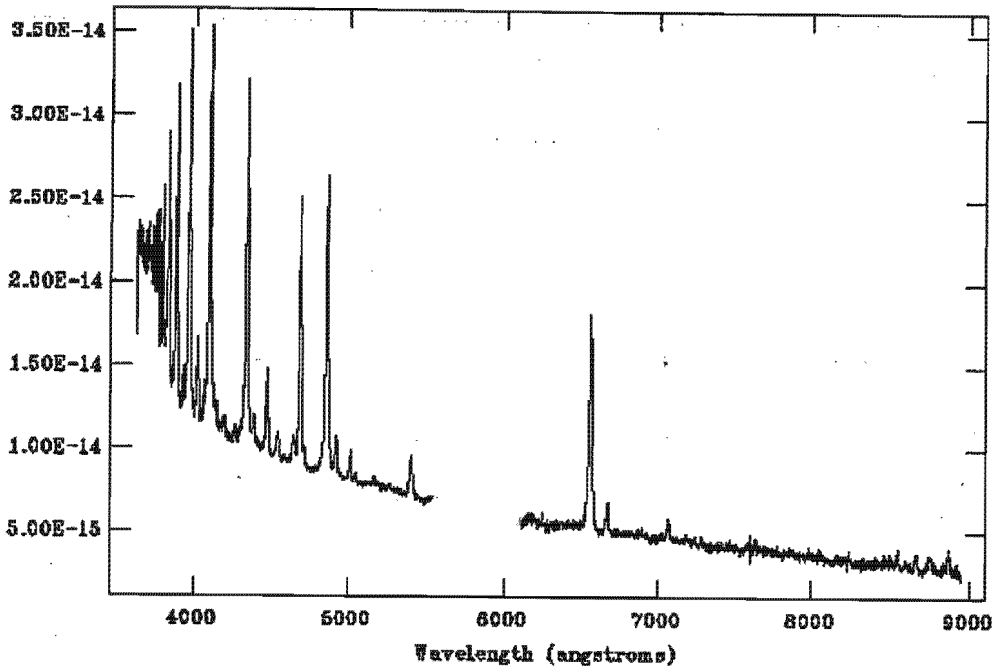
Figure 7.1: Combined red/blue mean-orbital bright phase spectrum of HU Aqr obtained on 24 August 1998.

between phases $\phi \sim 0.2$ - 0.7. Only the data points between phases $\phi \sim 0.2$ - 0.7 were thus used in the NEL radial velocity fit. The fit yields $\gamma = -13.52$ km s^{-1}, $K = 299.79$ km s^{-1} and $\phi_0 = 0.001$ for the NEL and $\gamma = -101.86$ km s^{-1}, $K = 529.44$ km s^{-1} and $\phi_0 = -0.30$ for the BBC. The results for both components are compatible with that obtained by Schwope, Mantel, & Horne (1997).

The radial velocity curves obtained from the Gaussian convolution scheme are illustrated in Fig. 7.4. The radial velocity curves for separation ≤ 700 km s^{-1} show a deviation from a pure sinusoid and an abrupt jump around phase $\phi \sim 0.5$. This deviation is most probably due to the fitting procedure attaching to different line components and is thus interpreted as being an artifact of the fitting procedure. The parameters obtained using Gaussian filters with separations 100, 200, 500 and 700 km s^{-1} are thus not very reliable. The three parameters (γ, K, ϕ) for Hβ, Hγ, Hδ & HeII λ4686 are, nevertheless, listed in Tables 7.2, 7.3, 7.4 & 7.5.

7.1.3 Doppler tomography

Doppler tomograms of Hβ, HeII λ4686, Hγ and Hδ have been computed. The trailed spectrograms of the four emission lines are displayed in Fig. 7.8 while the Doppler tomograms are shown in Fig. 7.9. The most prominent features in the tomograms are a bright spot centred at $V_x \sim 0$ km s^{-1} & $V_y \sim 300$ km s^{-1} and an extended feature extending from the bright spot to $V_x \sim -1000$ km s^{-1}. Roche lobes were calculated for a mass ratio of $q = K_1/K_2 = 0.25$ with $K_1 = 87$ km s^{-1} and $K_2 = 350$ km s^{-1} as used in Schwope, Mantel, & Horne (1997). The Roche lobes, together with the ballistic trajectory, are
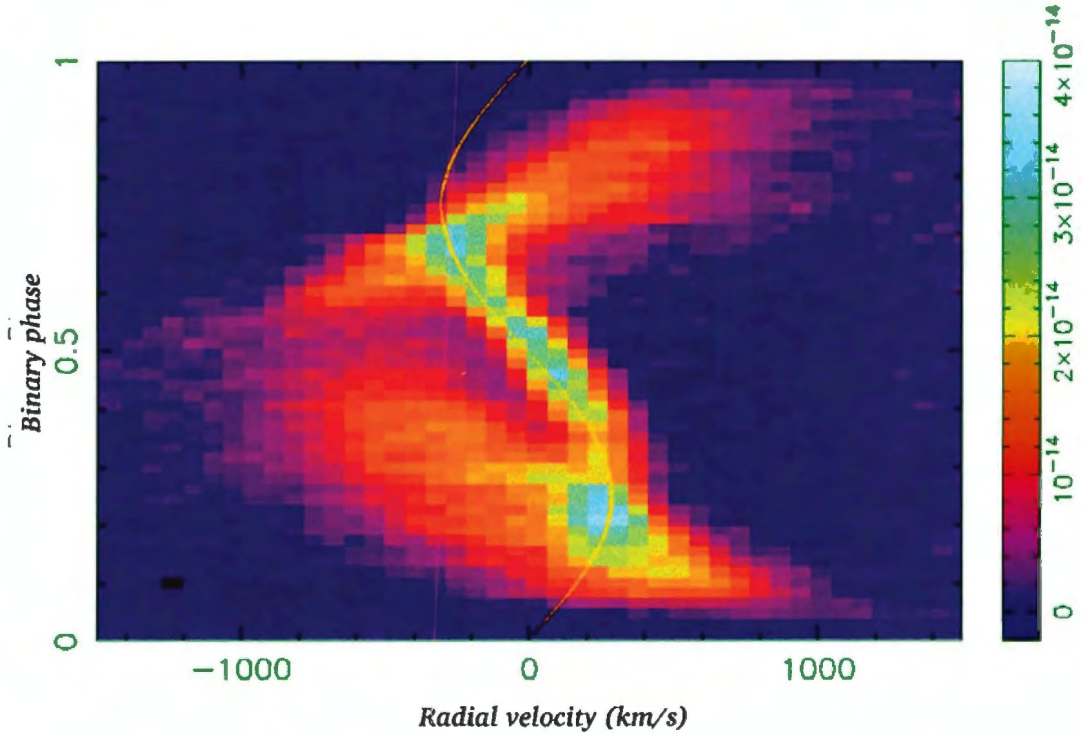
Figure 7.2: HU Aqr trailed spectrogram for HeII λ4686 with an overplotted sine wave. The sine wave was calculated from the radial velocity fits to the NEL.

Table 7.2: Variation in Hβ radial velocity parameters for HU Aqr.

sep km s^{-1}	FWHM km s^{-1}	γ-velocity km s^{-1}	K-velocity km s^{-1}	Phase offset
100	100	113.76	211.41	0.83
200	200	166.13	252.85	0.81
500	200	174.75	254.96	0.81
900	200	126.05	313.27	0.76
1200	200	96.54	355.53	0.73
1500	250	79.10	401.51	0.72
2000	400	87.23	489.55	0.70
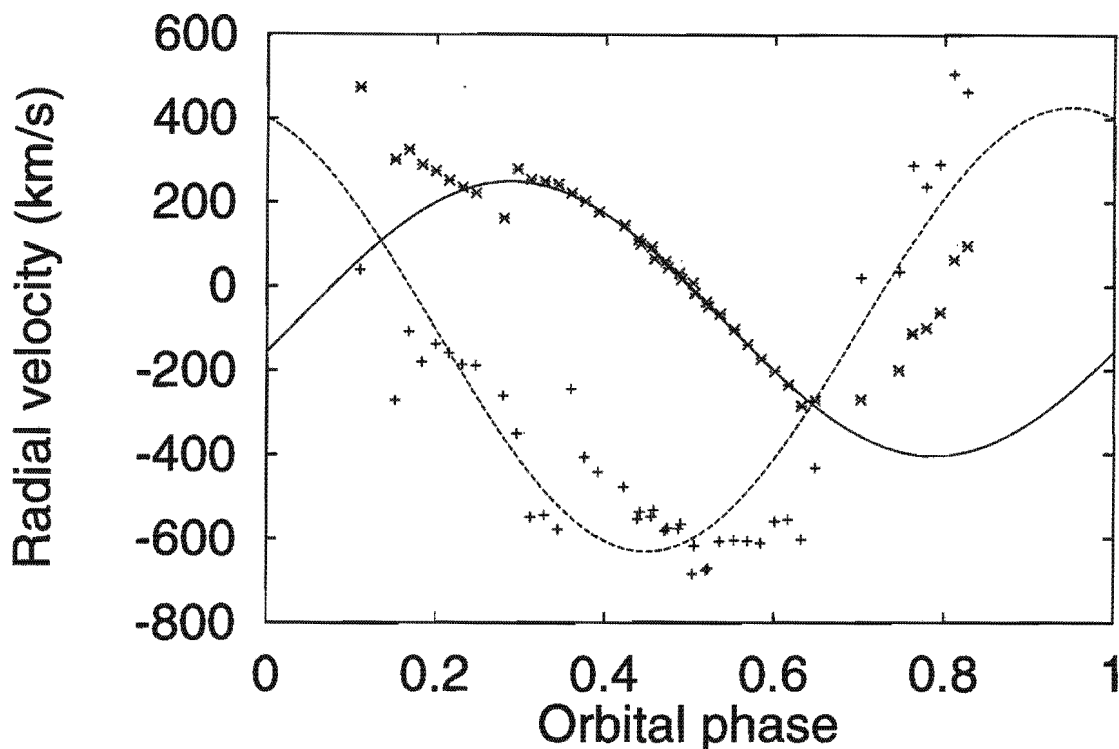
Figure 7.3: HU Aqr radial velocity plots for HeII λ4686 determined by Gaussian fits to the narrow & broad components with their non linear least-squares sine fit overplotted. The narrow component is represented by × and the broad component by +.

Table 7.3: Variation in HeII λ4686 radial velocity parameters for HU Aqr.

sep km s^{-1}	FWHM km s^{-1}	γ-velocity km s^{-1}	K-velocity km s^{-1}	Phase offset
100	100	120.83	222.54	0.83
200	200	134.35	234.45	0.83
500	200	156.81	264.26	0.78
700	200	145.27	305.51	0.77
900	200	123.35	348.71	0.74
1200	200	156.81	264.26	0.60
1500	250	99.63	477.83	0.69
2000	400	113.84	566.58	0.68
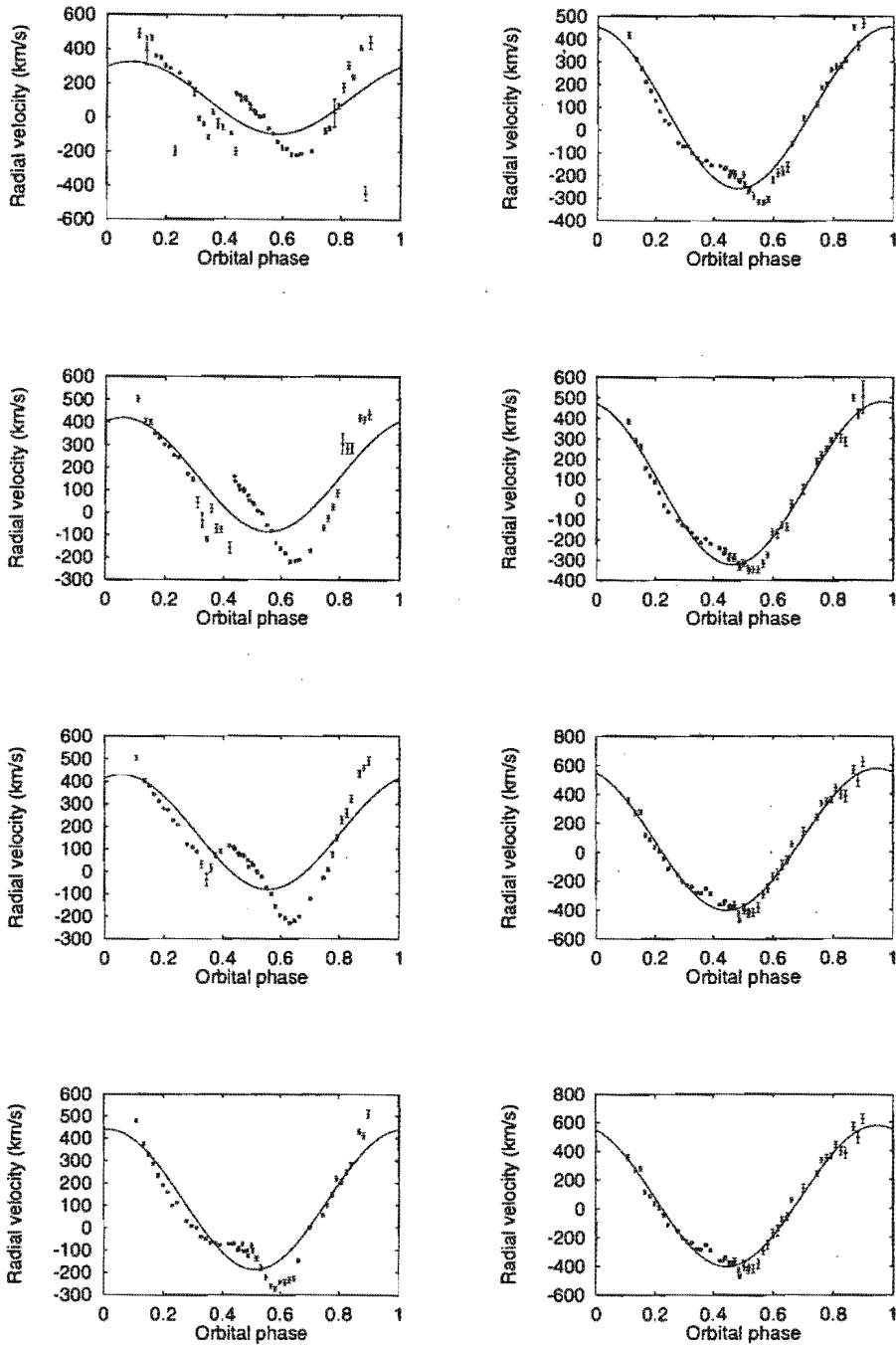
Figure 7.4: HU Aqr radial velocities for Hβ determined by the Gaussians convolution method. Plotted are the Radial velocities verses phase for the different separations of the Gaussian filters. The radial velocity curves for Gaussian separations 100, 200, 500, 700 are plotted from top to bottom in the first column and 900, 1200, 1500, 2000 in the second column.
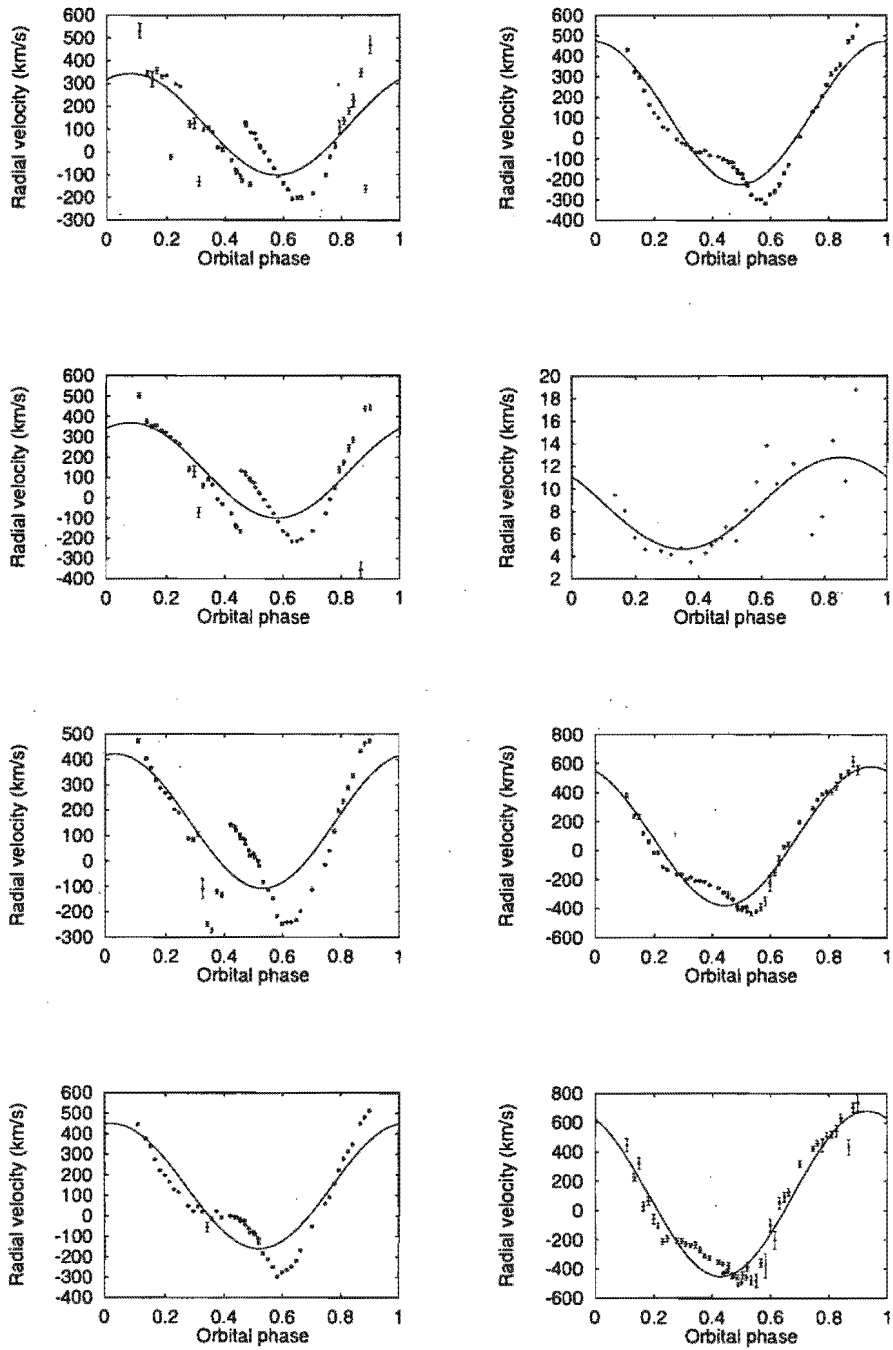
Figure 7.5: Same as for Fig. 7.4, but for HeII $\lambda4686$.
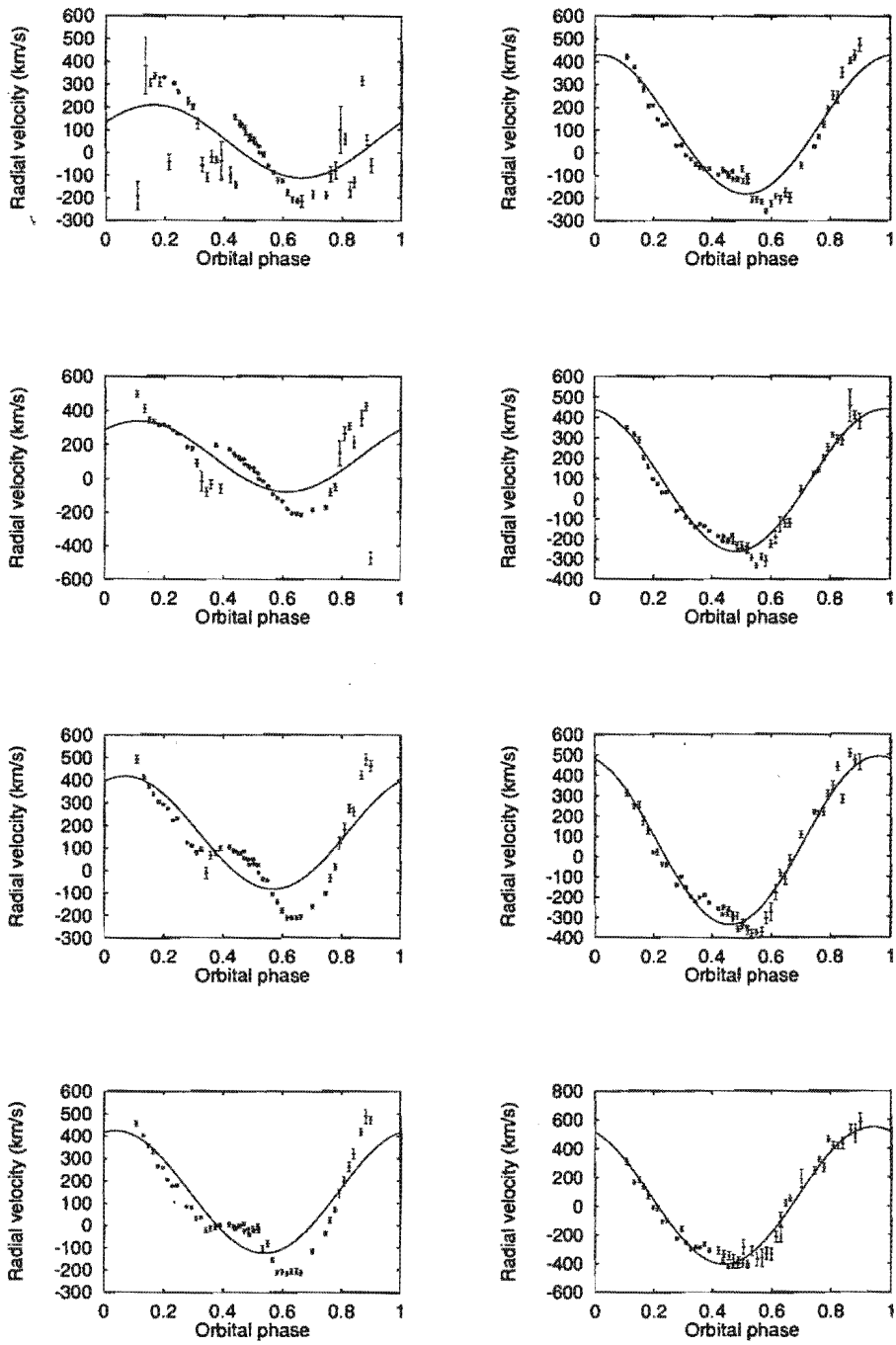
Figure 7.6: Same as for Fig. 7.4, but for Hγ.
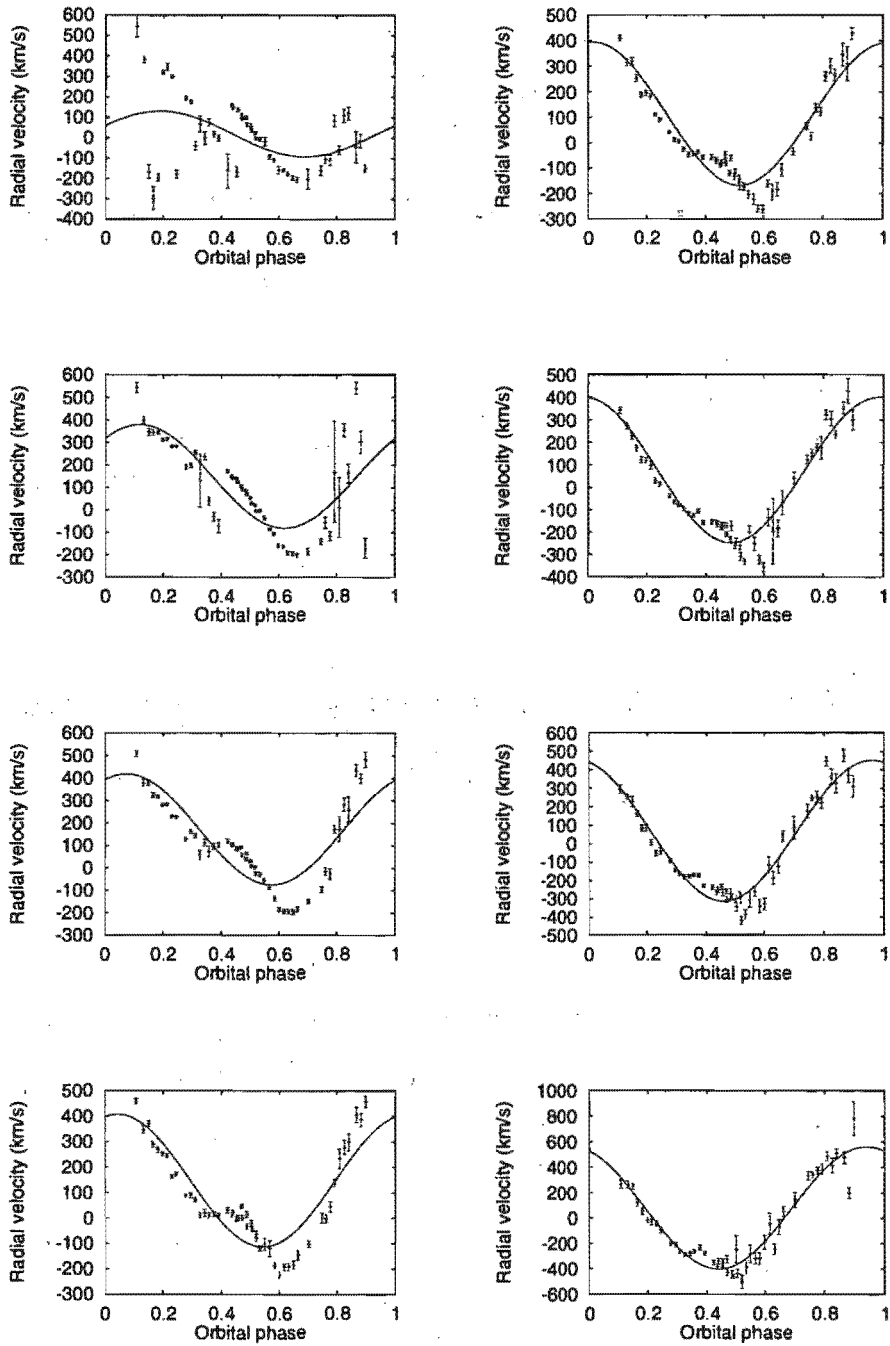
Figure 7.7: Same as for Fig. 7.4, but for Hδ.

Table 7.4: Variation in Hγ radial velocity parameters for HU Aqr.

sep km s^{-1}	FWHM km s^{-1}	γ-velocity km s^{-1}	K-velocity km s^{-1}	Phase offset km s^{-1}
100	100	49.22	160.56	0.91
200	200	129.77	208.60	0.86
500	200	167.98	250.75	0.81
700	200	150.07	274.77	0.79
900	200	124.05	306.56	0.76
1200	200	88.38	350.98	0.73
1500	250	76.99	414.40	0.71
2000	400	72.62	477.30	0.68

Table 7.5: Variation in Hδ radial velocity parameters.

sep km s^{-1}	FWHM km s^{-1}	γ-velocity km s^{-1}	K-velocity km s^{-1}	Phase offset
100	100	19.21	111.32	0.94
200	200	148.82	230.54	0.87
500	200	171.60	246.22	0.82
700	200	146.99	260.46	0.79
900	200	112.20	280.22	0.77
1200	200	75.88	324.07	0.74
1500	250	67.62	383.63	0.71
2000	400	77.76	481.19	0.69
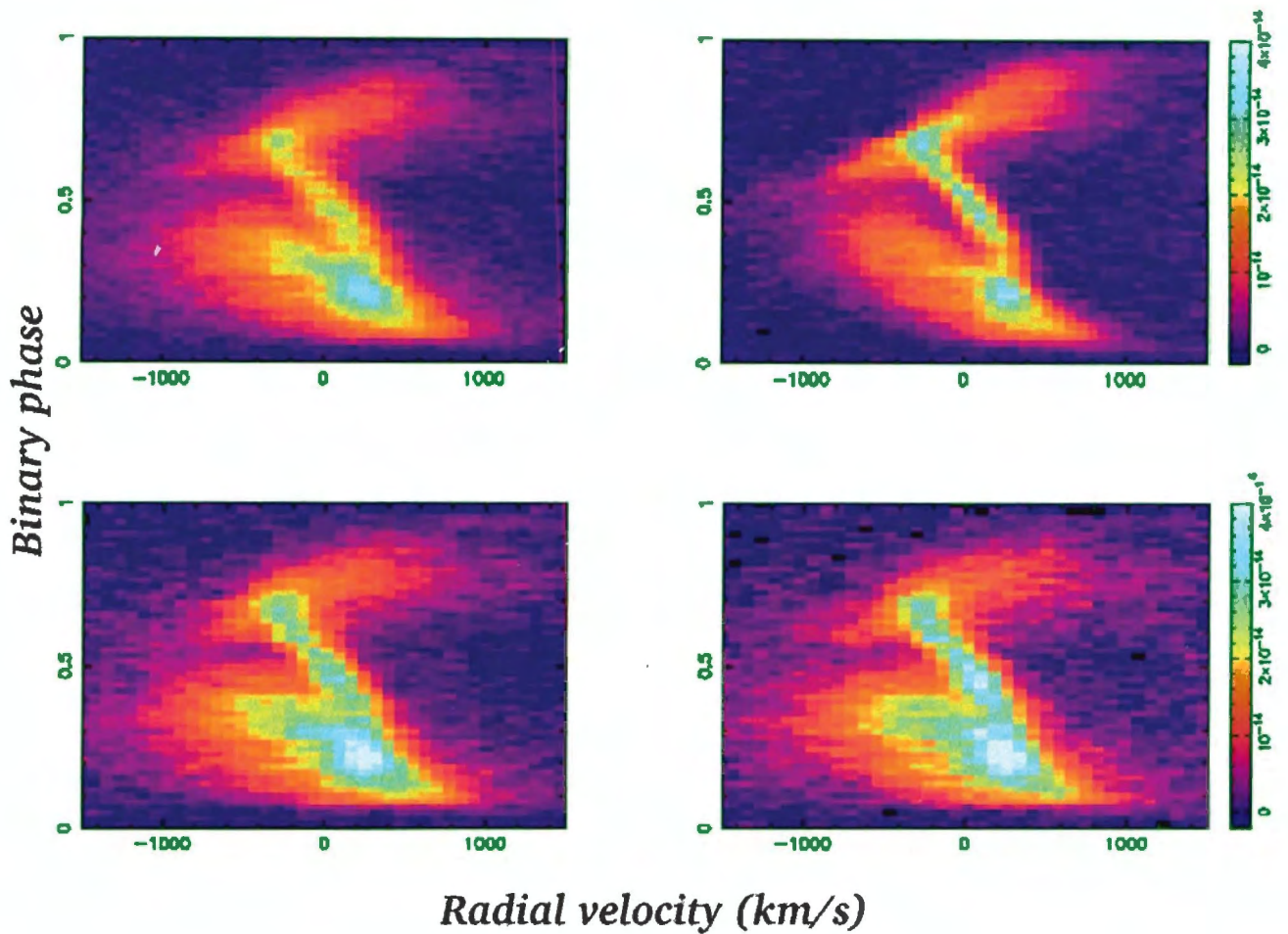
Figure 7.8: HU Aqr trailed spectrograms for Hβ & HeII λ4686 (from left to right) are plotted in the top column and Hγ & Hδ in the bottom column.

shown as overlays in Fig. 7.9 The bright emission spot lies within the calculated Roche lobe overlay, while the ballistic trajectory traces the extended region. This indicates that the bright spot originates on the irradiated face of the secondary and that the extended feature is a horizontal accretion stream. The radial velocity phase offset for the NEL is $\phi_0 = 0.001$, which also indicate that the NEL originates on the irradiated face of the secondary.

All four Doppler maps were plotted using the same intensity scale for comparison. The HeII λ4686 tomogram shows the sharpest features while the tomograms for the H-Balmer lines are more smeared, especially for Hβ. The accretion stream emission stream also does not show up in the H-Balmer tomograms as well as it does in the HeII λ4686 tomogram. In addition to the two main emission features, a third lower intensity feature appears in the HeII λ4686 tomogram as a smeared blotch at velocity coordinates $V_x \sim -500$ km s^{-1} & $V_y \sim -250$ km s^{-1}. This blotch is associated with the BBC. The phasing of the radial velocity curves for the BBC, from both the Gaussian convolution scheme and Gaussian
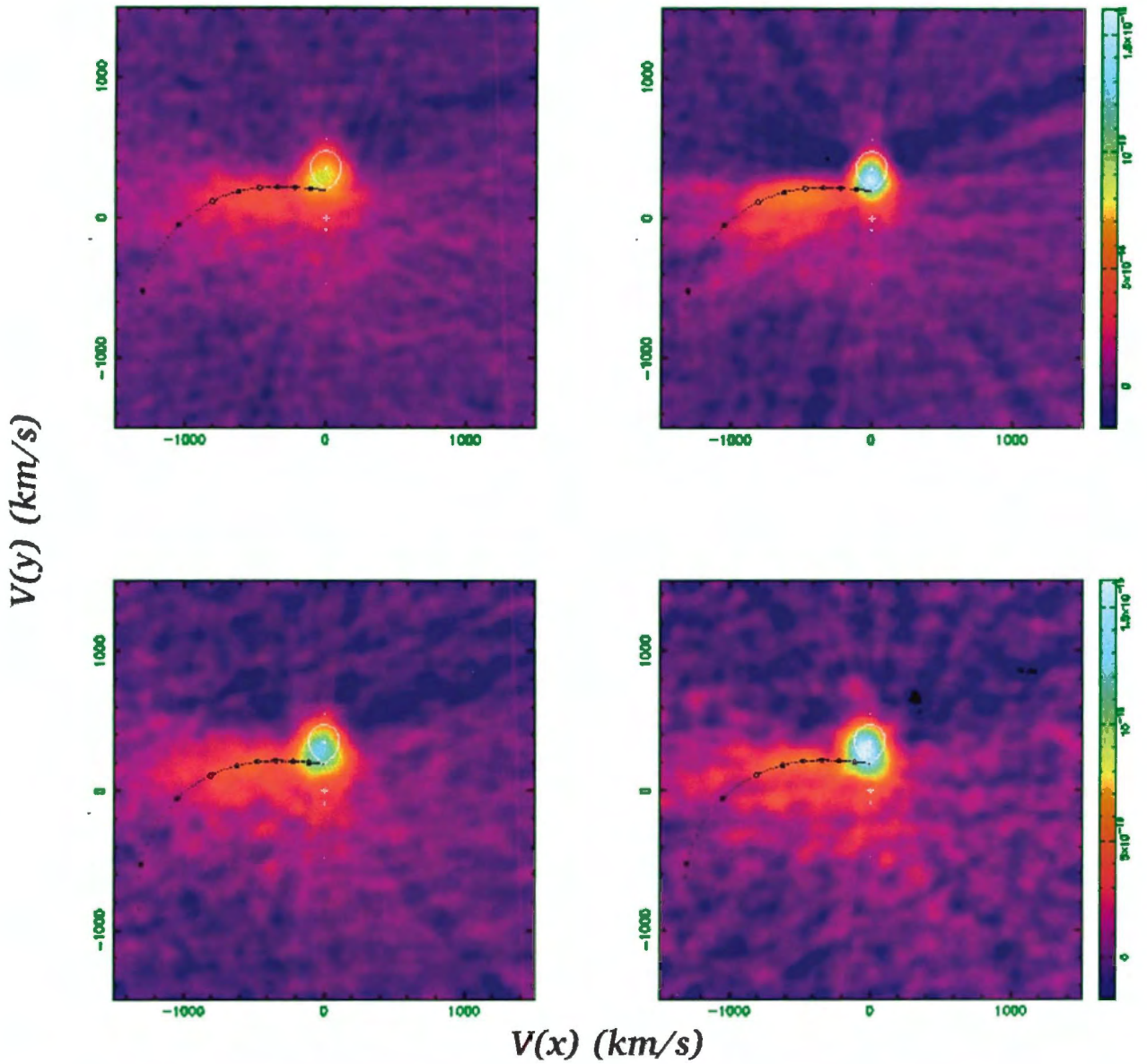
Figure 7.9: HU Aqr Doppler tomograms for Hβ & HeII λ4686 (from left to right) are plotted in the top row and Hγ & Hδ in the bottom row. Calculated Roche lobes and ballistic trajectory for a mass ratio $q = M_2/M_1 = K_1/K_2 = 0.25$ ($K_1 = 87$, $K_2 = 350$ km s^{-1}) are also overplotted.
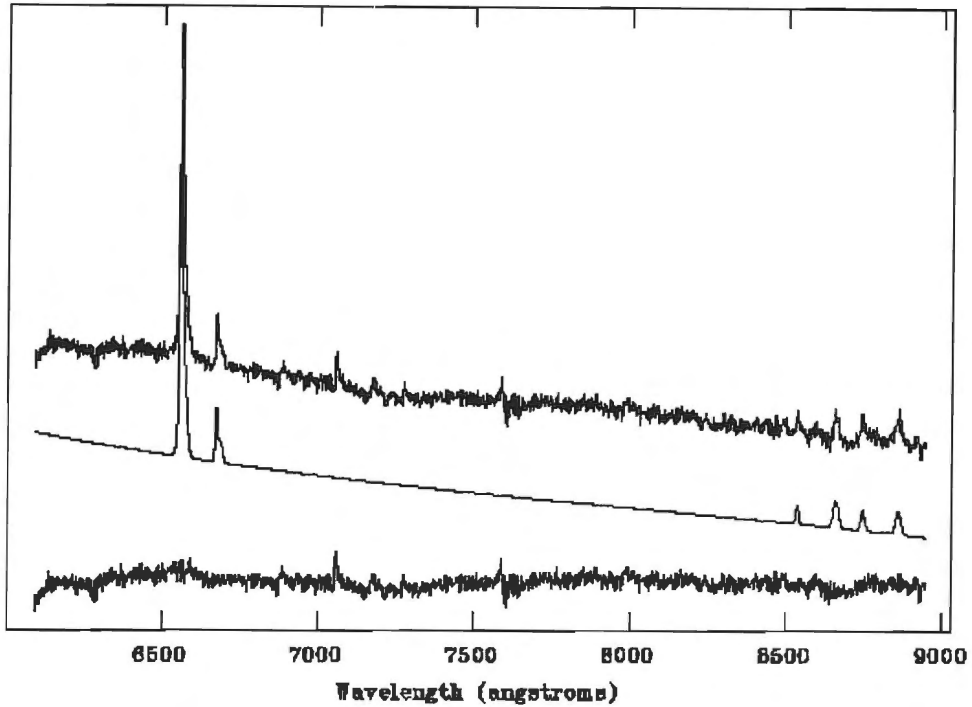
Figure 7.10: The mean spectrum ($\bar{\phi} \sim 0.65 - 0.75$) of HU Aqr is at the top. Beneath is a synthesized spectrum of Gaussian emission lines and low-order polynomial continuum. The residual cyclotron spectrum is in the third plot.

fitting, gives a phase offset of $\bar{\phi}_0 \sim 0.3$. This indicates that the BBC arises from the magnetically channeled part of the accretion stream, so the blotch is thus interpreted as originating from this region.

7.1.4 Cyclotron emission

A search was made for cyclotron emission in the red. A mean spectrum was calculated for the phase interval $\bar{\phi} = 0.65 - 0.75$ and the emission lines and continuum removed as described in Section 6.4.1. The mean spectrum together with the emission line and continuum and the residual cyclotron spectrum is plotted with an arbitrary offset and is illustrated in Fig. 7.10. The cyclotron harmonics at 6600 & 7900 Å are more easily visible in Fig. 7.11 where the cyclotron spectrum is plotted separately. A search for cyclotron humps was also conducted in the blue, but none were evident. This is probably due to a combination of the fact that the cyclotron emission intensity decreases toward the blue and because the spectral resolution for the blue spectra is too high. The intensity maxima at 6500 & 7860 Å were identified with the 5th and 4th harmonics and substituting these values in (3.12) gives the parameters $B = 39$ MG and $T\sin^2\theta = 11$ keV. The magnetic field strength $B = 39$ MG is higher than the value ($B = 37$ MG) obtained by Schwope, Mantel, & Horne (1997), but my estimate is less reliable as only two cyclotron harmonics were identified.

83
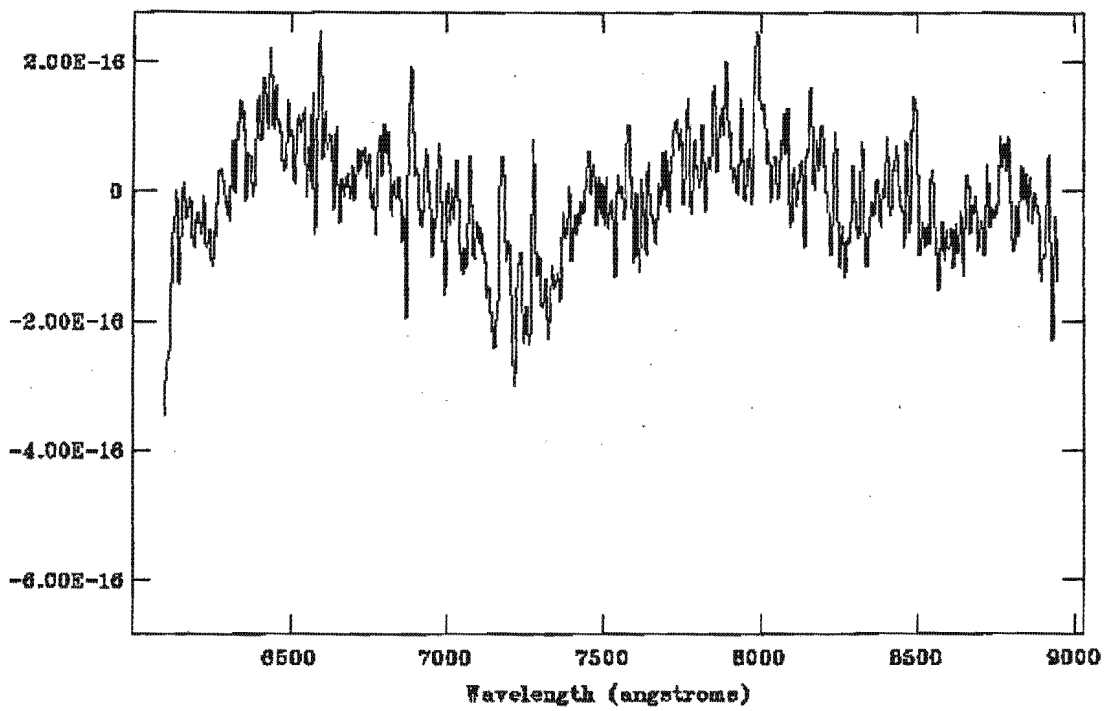
Figure 7.11: Cyclotron spectrum of HU Aqr with continuum and emission lines removed. Cyclotron humps can be seen at $\lambda\lambda$ 6600 & 7880 Å.

7.1.5 Conclusion

I have presented high resolution spectral observations of HU Aqr and have identified up to three emission line components in the trailed spectrograms of Hβ, HeII λ4686, Hγ & Hδ emission lines. With the aid of the Doppler tomograms, these components are identified as originating from the illuminated face of the secondary star, the accretion stream before it attaches to the magnetic field, and the magnetically channeled part of the stream. The Doppler maps presented in this thesis compares well with those of Schwope, Mantel, & Horne (1997) which were generated from high-state phase resolved ($\Delta\phi \sim 0.004$) trailed spectra. I have also identified two cyclotron harmonics, the relative spacing of which indicates a magnetic field strength $B = 39$ MG.

7.2 QS Tel

QS Tel (alias RX J1938.6-4612) was discovered independently by two ROSAT identification teams (Buckley et al. 1993; Beuermann & Thomas 1993) and became of interest because its period ($P \sim 2.33$ hrs) lies well within the period gap of CVs and because of its high EUV brightness. Strong cyclotron features were also detected by both Ferrario et al. (1994) and Schwope et al. (1995). QS Tel is included in this thesis as a test case to confirm the techniques of cyclotron spectroscopy and to investigate changes in the cyclotron spectrum.

7.2.1 Observations

Time resolved spectroscopy of QS Tel was obtained on 18 & 19 August 1999 covering a wavelength region $\sim 6000 - 8872$ Å and $\sim 3567 - 5492$ Å and giving full orbital phase coverage. Additional spectra were also obtained on 17 & 21 August 1999, but some of these were obtained under unfavorable weather conditions. See Tables 6.2 & 7.1 for a full observing record. The reduction process is detailed in Section 6.3. The mean spectra of QS Tel, shown in Figs. 7.12 & 7.13 exhibit strong emission lines of H-Balmer together with HeI, HeII and lines of the Paschen series. The spectra are also characterised by a large Balmer jump and broad continuum features.

7.2.2 Cyclotron spectroscopy

The broad features seen in the continuum of the spectra of QS Tel are similar in character to those observed in other Polars (see Chapter 5) where these feature have been interpreted as cyclotron harmonics. A similar interpretation is possible for QS Tel (e.g. Schwope et al. 1995; Ferrario et al. 1994). Secondary star features were removed before hand in order not to confuse the TiO bands with cyclotron lines. This was achieved by subtracting a suitably scaled M4.5V (GL 234AB) star template spectrum from each of the red spectra. Schwope et al. (1995) determined the spectral type of the secondary star to be M4.5. I also find that the M4.5 star template provided the best result in removing the TiO bands compared to using a M3.5V star template. In order to explore the full cyclotron information contained in the phase resolved spectra, they were phase-binned into 10 bins, the continuum fitted with a low order cubic spline and the emission lines removed by subtracting Gaussian (or multiple Gaussian) fits. Finally the spectra were normalised to unity. The blue and red spectra were combined to give a wavelength coverage of 3567 to 8870 Å. Finally the spectra were smoothed and converted to frequency space. The resulting stacked spectra and grey scale trailed spectrogram are shown in Figs. 7.14 & 7.15, respectively. The Balmer jump is intense between phases $\phi \sim 0.2 - 0.8$ and this complicates the search for harmonics longward of $\sim 7.6 \times 10^{14}$ Hz during these phases. The dark band seen at $\sim 7.8 \times 10^{14}$ Hz in Fig. 7.15 is due to the Balmer jump and is an artifact of the normalisation process. The gap in between 5×10^{14} - 5.45×10^{14} Hz is because the wavelength range of the blue and red spectral data do not overlap. The data in the greyscale are plotted twice for clarity.

Cyclotron spectra (see Fig. 7.16) were created by combining all spectra between phases $\phi = 0.8-1.2$ and $\phi = 0.3-0.6$. The phases were calculated using the ephemeris determined by Schwope et al. (1995). Gaussian fits to the individual cyclotron humps indicate peak
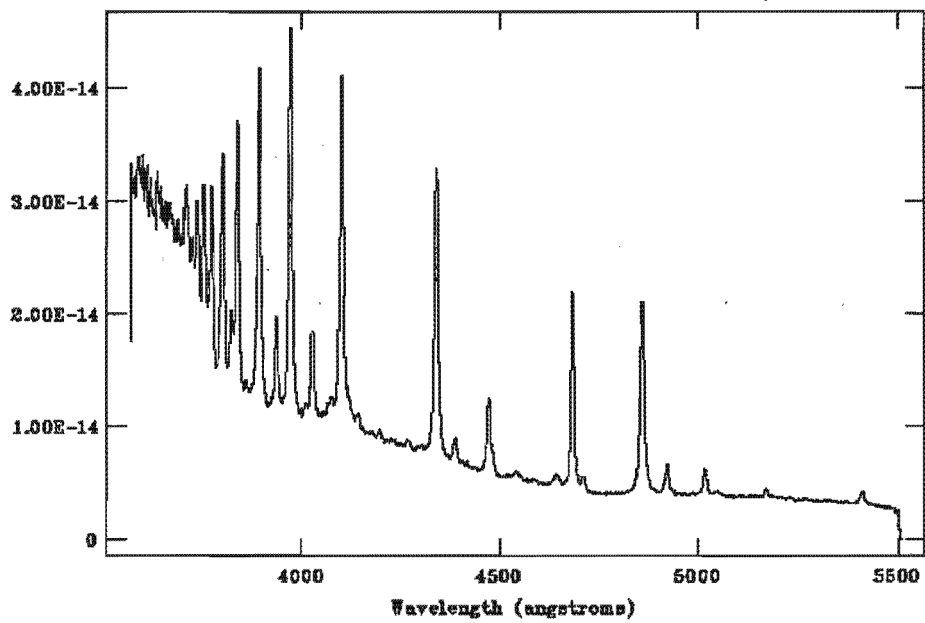
Figure 7.12: Mean blue spectrum for QS Tel.
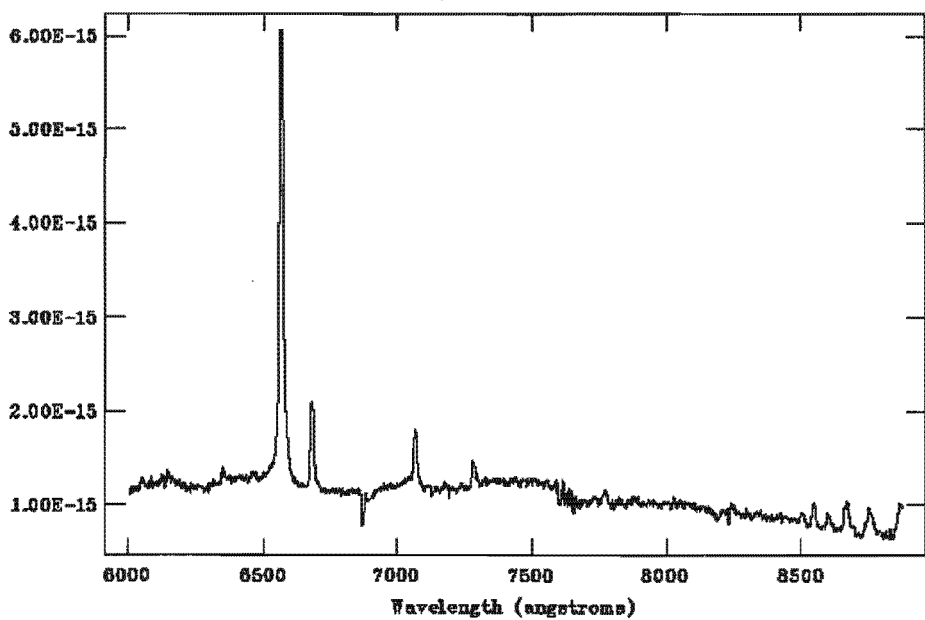
Figure 7.13: Mean red spectrum for QS Tel.
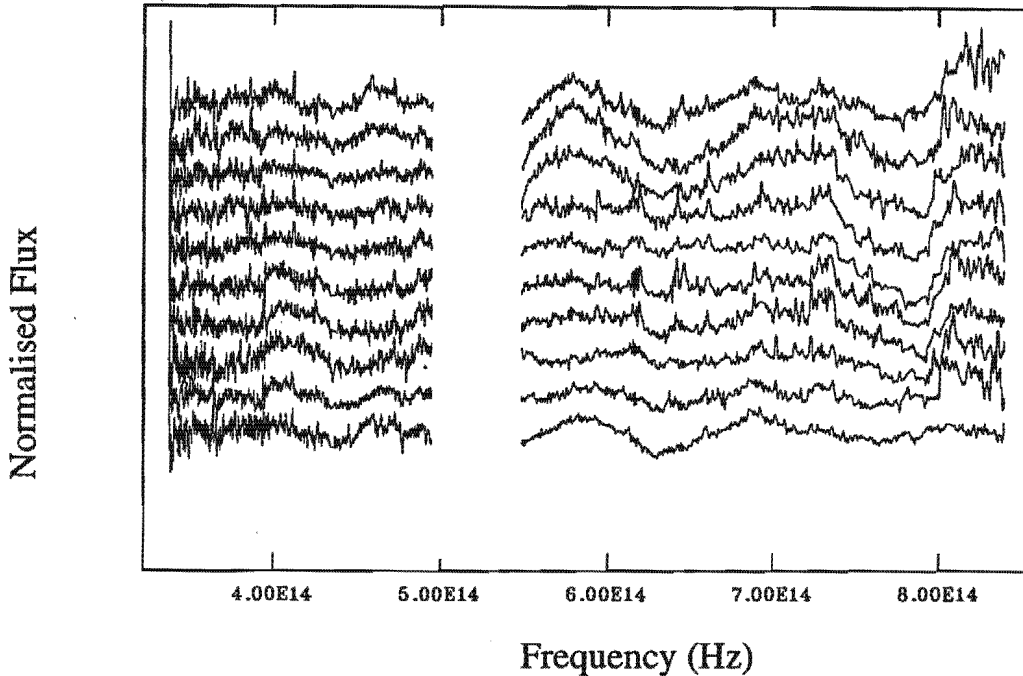
Figure 7.14: Phase resolved stacked cyclotron spectra for QS Tel. All spectra are normalised and phase binned. The spectra are vertically shifted with respect to one another starting with the first phase bin at the bottom. The gap in the data is due to the fact that the two sets of spectra do not overlap in frequency.

values at 8200, 7450, 6500, 5100, 4350 & 3680 Å (3.7×10^{14}, 4.0×10^{14}, 4.6×10^{14}, 5.9×10^{14}, 6.9×10^{14} & 8.2×10^{14} Hz). The harmonic at 7450 Å is visible nearly throughout the orbital cycle, while those at 8200, 6500, 5100, 4350, & 3680 Å are most prominent at phases $\phi \sim 0.8 - 1.2$. Schwope et al. (1995) similarly identified cyclotron harmonics at 3750, 5000 & 7500 Å with more humps detectable only between $\phi = 0.86 - 1.12$. They interpreted this as evidence for two pole accretion in QS Tel. While the first set of cyclotron lines dominate the Schwope et al. (1995) spectra, the second set of cyclotron lines are dominant in our spectra. The cyclotron peaks are also shifted to slightly lower frequencies in our data.

Schwope et al. (1995) identified the second set of humps as harmonic numbers 3 - 7 in a field of $B \simeq 47$ MG. If the same interpretation is followed in the current case, then a best fit cyclotron model identifies the humps at 8200, 6500, 5100, 4350 & 3680 Å (3.7×10^{14}, 4.6×10^{14}, 5.9×10^{14}, 6.9×10^{14} & 8.2×10^{14} Hz) as being the 3rd-7th harmonics. The parametres of the model (shown in Fig. 7.16) are $B = 45$ MG, $kT = 10$ keV and a viewing angle of $\chi = 80°$. The cyclotron absorption coefficients used in our models are normalised and suitably scaled to fit the cyclotron peaks. To test the possible misidentification of harmonics we investigated an alternative hypothesis where the main peak at 5.9×10^{14} Hz was $n = 4$, but this did not fit the observed spectra as well as the $B = 45$ MG model. This model required $B = 55$ MG with $kT = 10$ keV, $\chi = 80°$ when harmonic numbers $n = 3 - 5$, are predicted to occur in our spectra. This model curve is also shown
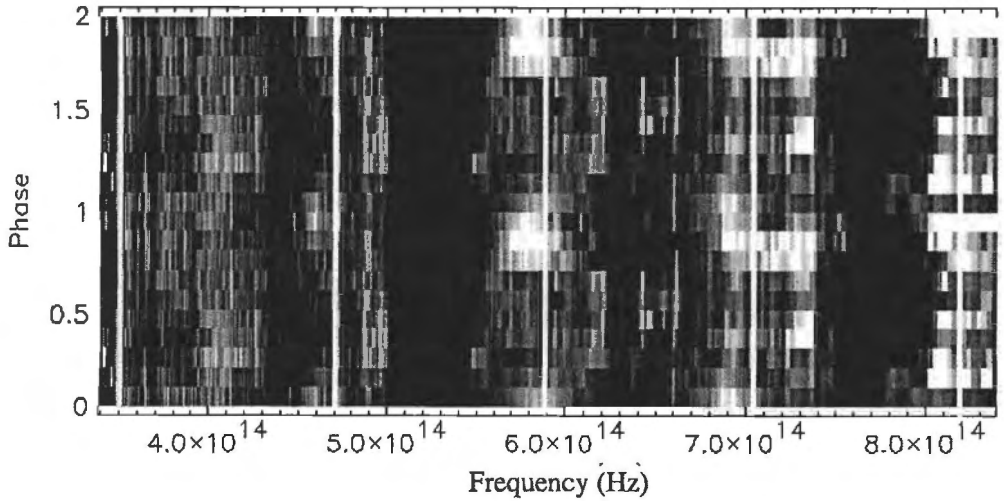
Figure 7.15: Grey scale phase resolved cyclotron spectrogram for QS Tel. The positions of the second set of harmonic peaks, are indicated by the hand drawn solid white lines.

in figure 7.16 (bottom dashed curve). Likewise a model where the main peak at 5.9×10^{14} Hz was $n = 6$ gave an even more unsatisfactory fits.

A cyclotron spectrum was created for the other magnetic pole by averaging all the cyclotron spectra between phases $\phi = 0.3 - 0.6$. A best fit cyclotron model indicates that the hump at 7450 Å (4×10^{14} Hz) is the 2nd harmonic in a $B = 65$ MG field. The parametres used for this model are $B = 65$ MG, $kT = 5$ keV and $\chi = 40°$. The observed cyclotron spectra and model is shown in Fig. 7.16. To test the possible mis-identification of harmonics we investigated an alternative model, as for the other set of cyclotron lines. Identifying the line at 4×10^{14} Hz as the $n = 3$ harmonic with parametres $B = 45$ MG, $kT = 5$ keV and $\chi = 40°$, gave a less favourable fit. This is also shown in Fig. 7.16 (top dashed curve).

Our models did not take into account different optical depth parameters, viewing angles and non-uniformities in the temperature and magnetic field structures, all of which are parameters which could influence the cyclotron spectrum, in particular the relative intensities of the harmonics. We cannot, thus, rule out a different interpretation of the observed cyclotron spectrum. More detailed modeling, taking these parametres into account, is required.

7.2.3 Conclusion

In the previous section I have shown that two sets of cyclotron lines are present in our QS Tel data. The main result of the data presented here is that the second set of cyclotron humps are more prominent in our data set than in Schwope et al. (1995). Magnetic field strength determination indicate fields of $B = 45$ & $B = 65$ MG for the two magnetic poles. The field of the stronger pole is lower than the $B = 70 - 80$ MG estimated by Schwope et al. (1995), while the weaker pole is of similar strength, although the second set of cyclotron lines could also be fitted with a $B = 55$ MG model, but this gave a less favourable fit. More detailed cyclotron modeling taking into account different optical depth parametres and considering non-uniform temperatures and field strengths across the
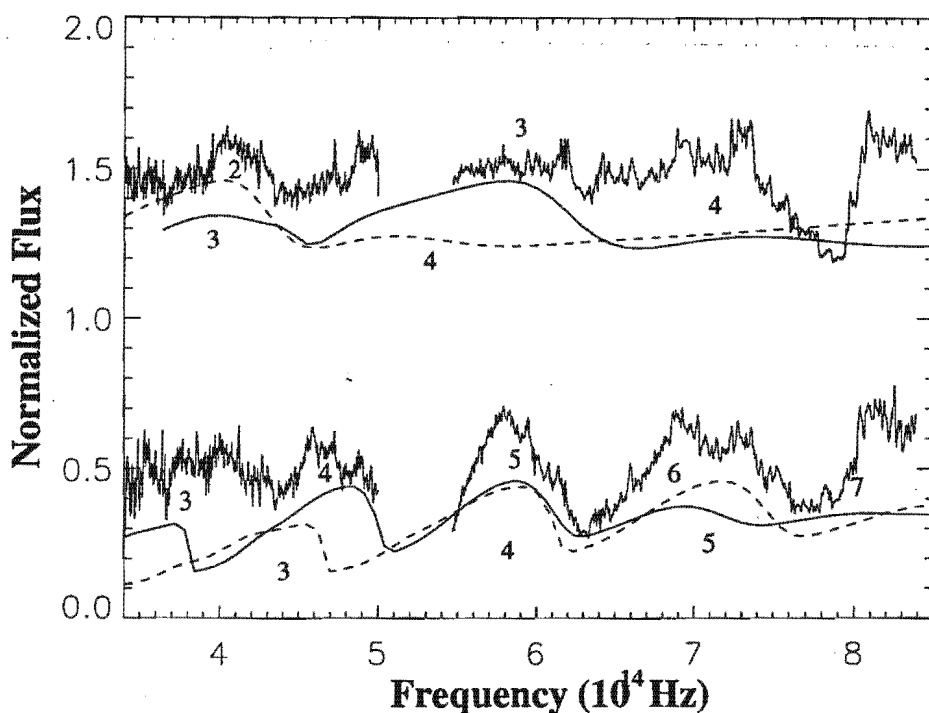
Figure 7.16: Bottom plot: Cyclotron spectrum for QS Tel centred on phase $\phi = 0.9$. The solid and dashed curves are normalised and suitably scaled model spectra for parametres $B = 45$ & 55 MG, $kT = 10$ keV and $\chi = 80°$, respectively. Harmonic numbers for the solid curve is placed above and numbers below correspond to the dashed curve; Top plot: Cyclotron spectrum for QS Tel centred on phase $\phi = 0.4$. The solid and dashed curves below the observed spectra are normalised and suitably scaled model spectra for parametres $B = 65$ & 45 MG, $kT = 5$ keV and $\chi = 40°$, respectively. Harmonic numbers for the solid curve is placed above and numbers below correspond to the dashed curve.

accretion column, is needed to obtain a more accurate magnetic field strength estimate.

7.3 RX J1313.2-3259

7.3.1 Introduction

RX J1313.2-3259 (RX J1313-32) was discovered from the RASS (Beuermann & Thomas 1993). It is a Polar with a long orbital period of $P{\sim}4.18$ hrs (Thomas et al. 1999), thus forming together with V1309 Ori (alias RX J0515.6+0105)($P_{orb} = 8$ hrs), V895 Cen (alias EUVE J1429-38.0)($P_{orb} = 4.7$ hrs) and RX J0203.8+2959 ($P_{orb} = 4.6$ hrs) a group of outstanding systems with long orbital periods.

7.3.2 Observations

Time resolved spectroscopy of RX J1313-32 was obtained on two consecutive nights in January 1999 (21&22) giving effectively a full orbital coverage. It was not possible to obtain full orbital coverage of this system in one night because of the position of the system during the January 1999 run. During the February 1999 run the system was more suitably placed for full orbital observation, but at this time the system was in a low state. We did, however, obtain a sequence of low state red spectra giving full orbital coverage. We also attempted to obtain blue spectra, but the system was too faint. During the August 1999 run the system was in a higher accretion state, but a combination of bad weather, bright moon and the fact that the system set early in the evening meant that we could not obtain a full orbital coverage. We did manage to obtain a sequence of high resolution blue spectra on two separate nights, but these unfortunately gave a similar phase coverage ($\phi \sim 0$ - 0.6). See Table 6.2 & 7.1 for an observing log. The reduction process is described in Section 6.3.

7.3.3 Spectrum

In the red spectral range the spectra are dominated by secondary star features, as can be seen in the mean combined spectrum from the January data shown in Fig. 7.17. TiO absorption bands are clearly visible at $\lambda\lambda$ 6195, 6322, 6651 & 7051 Å as well as the NaI doublet at $\lambda\lambda$ 8183 & 8194 Å. The January 1999 spectra exhibit a strong Hα emission line and weaker lines of neutral helium (e.g. HeI $\lambda\lambda$ 5875, 6678 & 7065 Å). The H-Paschen series and CaII triplet at $\lambda\lambda$ 8498, 8542 & 8662 Å are also visible. The blue spectra obtained in August 1999 exhibit strong emission lines of H-Balmer (Hβ - H11), neutral Helium (HeI $\lambda\lambda$ 3936, 4026, 4387, 4471, 4927 & 5015 Å) and ionized Helium (HeII $\lambda\lambda$ 4686 & 5411 Å). A mean combined spectrum from the August 1999 data shown is in Fig. 7.18.

7.3.4 Radial velocity

Radial velocities for the Hα emission line were determined using a Gaussian convolution scheme using eight Gaussian "filters" with separations of 2000, 1500, 1200, 900, 700, 500, 200 and 100 km s^{-1}, and corresponding Gaussian sigmas of 400, 250, 200, 200, 200, 200, 200 and 100 km s^{-1}. Radial velocities via the Gaussian convolution scheme were determined for the Hα line only, since it is the only strong emission line observed over the entire orbital period and with good phase resolution ($\Delta\phi \sim 0.025$). Each radial velocity
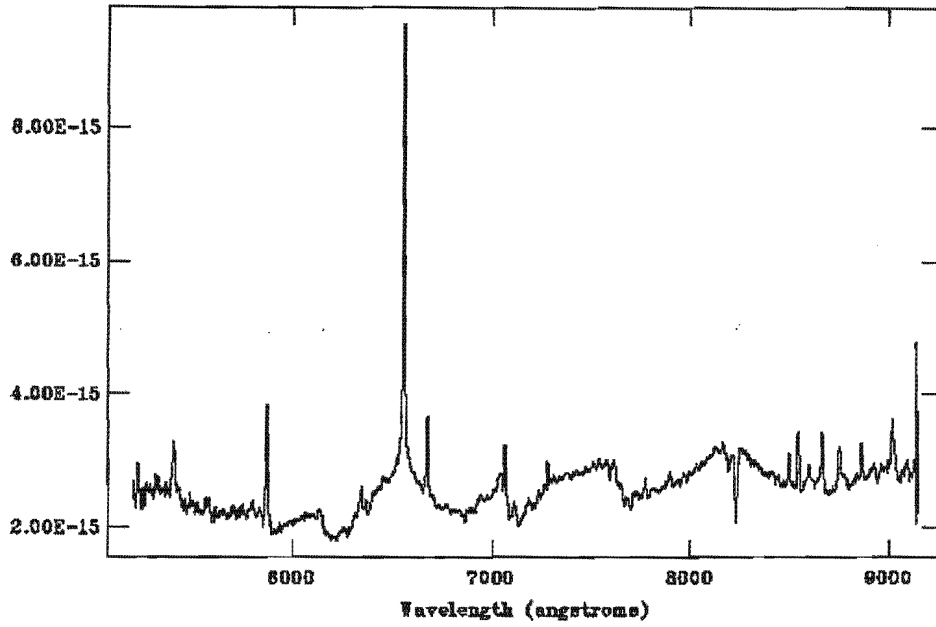
Figure 7.17: A mean combined spectrum of RX J1313-32 from the January 1999 observations.
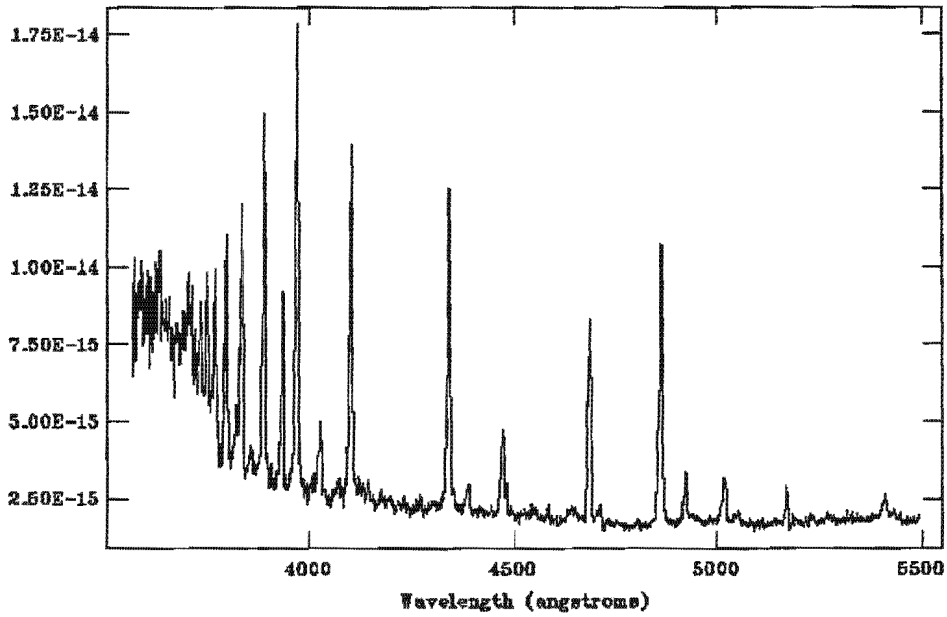
Figure 7.18: A mean combined spectrum of RX J1313-32 from the August 1999 observations.

92

Table 7.6: Variation in Hα (RX J1313-32) radial velocity parameters

sep	FWHM	γ-velocity	K-velocity	Phase offset
km s^{-1}	km s^{-1}	km s^{-1}	km s^{-1}	
100	100	47.39	126.30	0.034
200	200	47.95	123.59	0.024
500	200	51.31	114.41	-0.015
700	200	53.25	117.65	-0.083
900	200	53.95	154.02	-0.155
1200	200	66.18	227.92	-0.232
1500	250	83.70	307.25	-0.258
2000	400	144.70	357.10	-0.266

curve was phase folded using the ephemeris of Thomas et al. (1999) and the amplitude (K-velocity), systemic velocity (γ-velocity) and phase offset (ϕ_0) determined by fitting 4.1, using a nonlinear least-squares algorithm.

Fig. 7.19 shows the radial velocity (RV) curves for the Hα line, together with their best-fit sinusoids, and the three variable parameters (K,γ,ϕ_0) are listed in Table 7.6 and plotted in Fig. 7.22. From these plots it can be seen that the K-velocity increases into the wings up to a value of ∼371 km s^{-1} for a Gaussian filter with a separation of 2000 km s^{-1}. There is also a phase shift as a function of Gaussian separation with the phase offset shifting from $\phi = 0.034$ for a separation of 100 km s^{-1} to $\phi = -0.266$ for a separation of 2000 km s^{-1}. From the phase shift between the RV curves for a separation of 100 & 2000 km s^{-1} it follows that the broad line emission region leads the narrow line emission region by $\Delta\phi = 0.3$. This phase shift is also illustrated in Fig. 7.20 where RV curves for separations 200 & 1200 km s^{-1} are over-plotted. From the RV plots in Fig. 7.19 it can be seen that the narrow line component does not follow a pure sinusoid, instead its motion is deflected at phases $\phi \sim 0.2$ & 0.7. This deflection can be interpreted as resulting from the influence of a different components crossing over the same velocity space at those phases. Fig. 7.20 shows the RV curve for separations 200 & 1200 km s^{-1} crossing at phases $\phi = 0.2$ & 0.7.

To help quantify the secondary star contributions, a library of M-dwarf (see Table 7.7) spectra was created by observing stars classified from M1.5 to M4.5 in the list given by Kirkpatrick, Henry, & McCarthy (1991). These spectra, with differing scaling factors, were subtracted from the observed RX J1313-32 spectra until best removal of M-star features was reached. I created a mean faint phase spectrum and judging from the removal of the M-star templates from this, found the M3.5V star GL 273 as the most suitable template.

The radial velocities of the CaII triplet (8498, 8542 & 8662 Å) was computed by fitting Gaussians to the emission lines and calculating the radial velocities from the relative shifts of the line centres. The CaII lines are only visible in the spectra between phases $\phi \sim 0.2 - 0.8$, this is because the irradiated face of the secondary star (where the CaII emission originates) is not in view outside this phase range as it is self-eclipsed by the cooler part of the star. In addition, I attempted to determine the secondary star radial velocity via Fourier cross-correlation, using the FXCOR routine in the IRAF radial velocity package. Here I correlated the object spectra against the M-star (GL 273) template. The radial
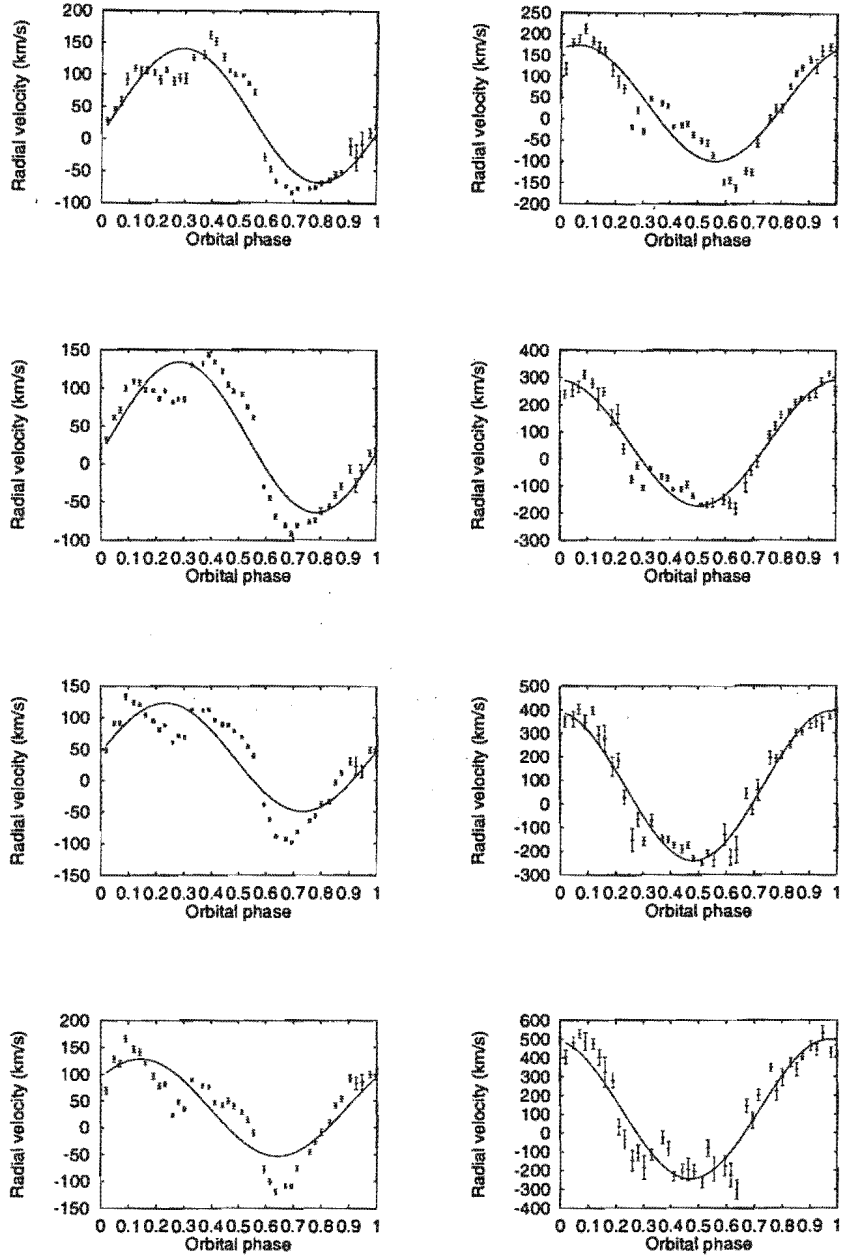
Figure 7.19: Radial velocity curves computed for Hα (RX J1313-32). The curves were computed via Gaussian convolution for separations 100 - 700 km s^{-1} in the first column (top to bottom) and 900 - 2000 km s^{-1} in the second column.
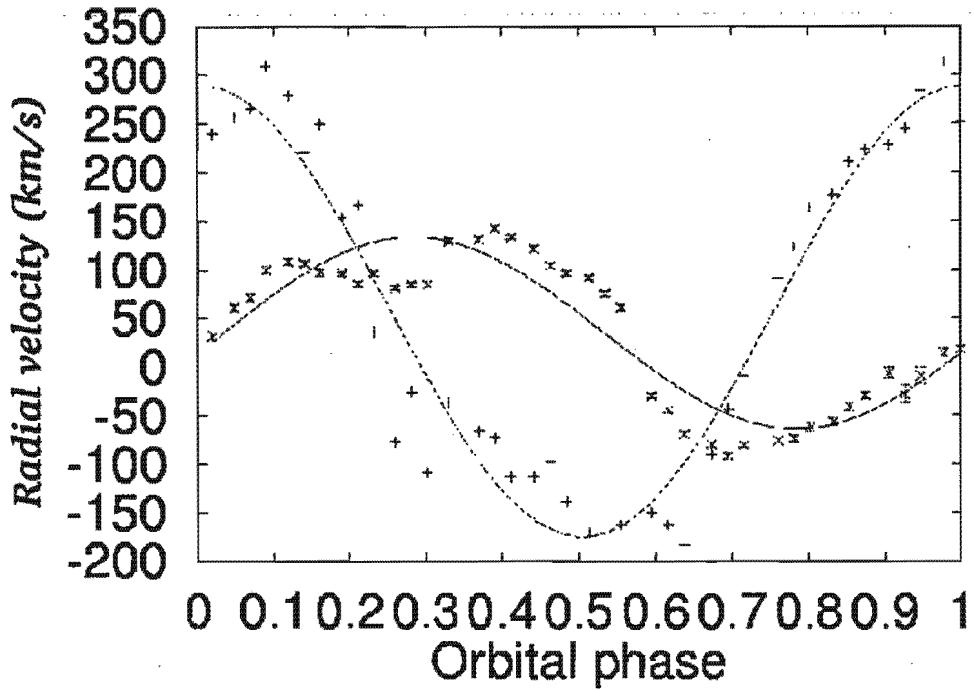
Figure 7.20: Radial velocity for Hα (RX J1313-32) separations 200 & 1200 km s^{-1}. The two velocity components share the same velocity space at phase $\phi = 0.2$ & 0.7.
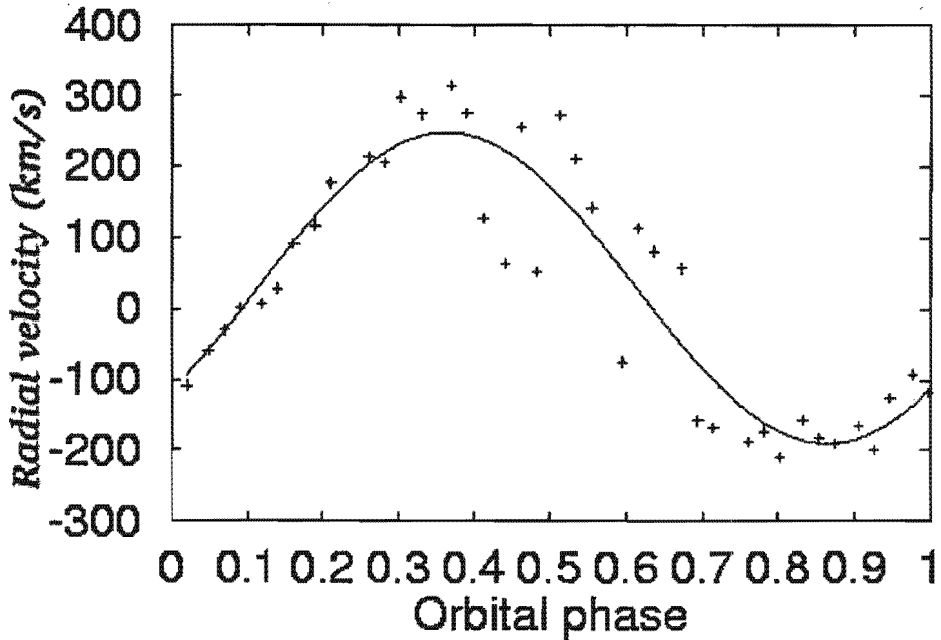
Figure 7.21: Radial velocity curve for RXJ 1313-32 secondary star computed via Fourier cross correlation using a dM3.5 star (Gl 273).
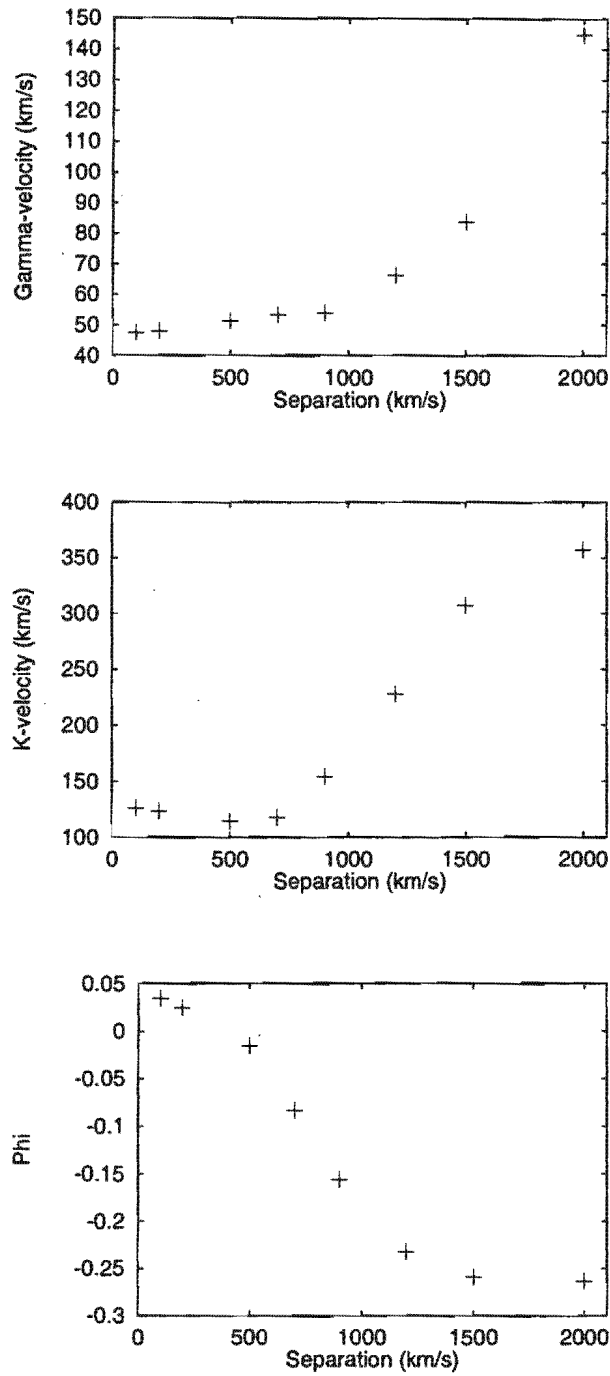
Figure 7.22: Plotted are the parameters from the Gaussian convolution radial velocity fits for Hα (RX J1313-32). γ, K and ϕ are plotted verses separation.

Table 7.7: List of M-stars observed for use as templates.

Star	Spectral type
GL 205	M1.5V
GL 250B	M2.5V
GL 352B	M3V
GL 273	M3.5V
GL 234AB	M4.5V

Table 7.8: Radial velocity parameters from fits to Fourier cross-correlation data and the CaII triplet

Line	γ-velocity	K-velocity	Phase offset
	km s^{-1}	km s^{-1}	
M-star (FXCOR)	29.16	219.29	0.11
CaII λ8498 Å	8.50	94.02	0.05
CaII λ8542 Å	6.84	78.53	0.04
CaII λ8662 Å	5.39	68.62	0.03

velocity curves were phase folded and the amplitude (K-velocity), systemic velocity (γ-velocity) and phase offset (ϕ_0) determined as for the Hα line. Figs. 7.21 & 7.23 show the radial velocity curves computed via Fourier cross-correlation and from Gaussian fits to the CaII lines with the fit parameters listed in Table 7.8. The K-velocity for the radial velocity curve computed via cross-correlation ($K = 219$ km s^{-1}) is high compared with the K-velocities determined for the Gaussians fits to the CaII triplet. This is most likely due to the FXCOR routine weighing the Hα emission line more than the TiO bands and thus effectively computes the radial velocity for the Hα line. I attempted cross-correlation with a mask applied to the Hα region, but the routine had difficulty cross-correlating the spectra. The results from the Fourier cross-correlation method are thus not considered to reflect the radial velocity of the secondary cross-correlation but I have included the results for completeness. The radial velocity determined for the CaII λ8498 Å is considered to be a more accurate reflection of the secondary star radial velocity, this is also supported by the phasing of the CaII λ8498 Å ($\phi \sim 0.05$) which is in agreement with the expected phase of the secondary. Not much importance is placed on the CaII λ8542,8662 Å lines, since these lines are blended. I also attempted to determine the radial velocities of the Na line only, but this result gave considerable scatter.

7.3.5 Doppler tomography

Doppler maps were constructed for RX J1313-32 using the Fourier filtered back-projection method described in Section 4.3.1. Fig. 7.24 shows the trailed spectrograms for RX J1313-32 calculated for Hα (from the Jan 1999 data) and Hβ, HeII λ4686 & Hγ (all from the Aug 1999 data) while the resulting tomograms are displayed in Fig. 7.25. The Aug 1999 data did not give full a phase coverage ($\phi \sim 0.1 - 0.65$) or good phase resolution ($\Delta\phi \sim 0.045$), but it is possible to construct a Doppler tomogram from half an orbit (see Section 4.3). The trailed spectrograms and Doppler tomograms for Hβ, HeII λ4686 &
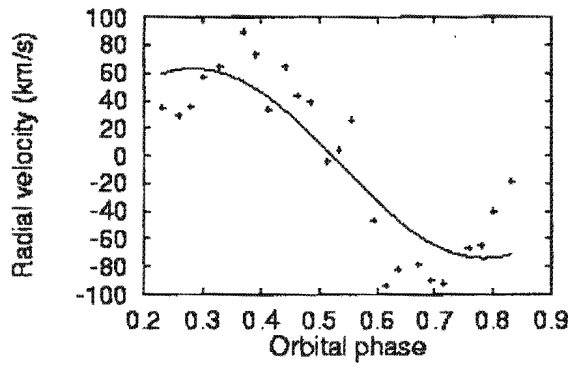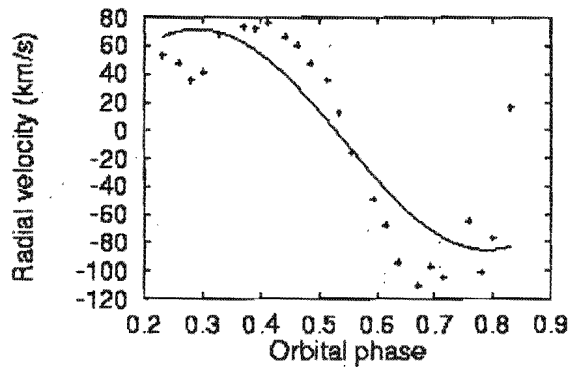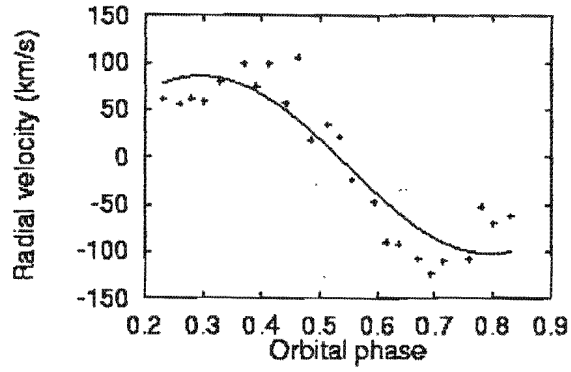
Figure 7.23: Radial velocity curves for Gaussian fits to the CaII triplet at $\lambda\lambda$8498,8542 &
8662 Å (from top to bottom).

Hγ clearly shows multicomponent emission with different intensity and radial velocity emission. The ray-like features seen extending from the origin to higher velocities in the Doppler maps of Hβ, HeII λ4686 & Hγ are spurious and due to the coarse phase resolution of the data. The Hα emission line trailed spectrogram and tomogram do not show the the radial velocity and intensity variations as clearly, since these data were taken at low spectral resolution (~ 5 Å).

Two structures are clearly evident in tomograms computed from the data of Aug 1999. A primary emission region is evident as a compact zone close to/at the expected location of the secondary star, and also a "cometary" tail like component with motion toward the white dwarf primary, which is material leaving the secondary in a stream. Calculated Roche lobes for $K_1 = 82$ and $K_2 = 135$ km s^{-1} giving a mass ratio $q = 0.6$ are overplotted in the tomograms and can be used to compare features in the different emission line Doppler maps. A value of $K_2 = 135$ km s^{-1} has been used considering the fits to the CaII lines and taking the orbital inclination to be $i = 40°$ as estimated by Thomas et al. (1999) who also estimate a mass ratio $q = 0.6$. The Roche lobe and ballistic trajectory for these parameters traces the bright spot and cometary tail features reasonably well, which indicates that $q = 0.6$ is reasonable for the mass ratio. Doppler maps and trailed spectrograms for low inclination systems are usually smeared due to the low projected radial velocities and the different line component are not easily resolved. The trailed spectrograms for RX J1313-32 show line velocities approaching -1000 km s^{-1} and one can easily resolve the stream and secondary emission in the Doppler maps. This indicates that the the orbital inclination ($i = 40°$) estimated by Thomas et al. (1999) is too low.

The stream also shows some structure, but this could be due the influence of out of plane velocities which tend to smear the Doppler images. There also seems to be another compact structure attached to the bright spot, but not much can be said about this considering the poor phase resolution of our data.

7.3.6 Search for cyclotron emission

Since the secondary star dominates the red spectral region it was necessary to remove the secondary features to facilitate the search for cyclotron features. After subtraction of the secondary spectrum the remaining light should consist predominantly of the following components: photospheric radiation from the magnetized white dwarf, radiation from the accretion stream (and reprocessed radiation from near the accretion stream), and cyclotron radiation beamed from the accretion region.

Fig. 7.27 shows the decomposition of RX J1313-32's spectrum into the M-dwarf (GL 273) template and the residual emission. The subtraction of the template from the bright phase spectra proved to be less successful than that of the faint phase and show a hump at Hα in Fig. 7.28. The hump is most prominent at phases centering $\phi \sim 0.25$ & 0.75, as can be seen in the trailed spectrogram shown in Fig. 7.26.

A possible explanation as to why the removal of the M3.5V star from the bright phase is not as successful is that as the system rotates from the faint phase to the bright phase the irradiated face of the secondary becomes increasingly more visible. This effect would introduce earlier M-star features in the brighter phases as compared with the spectral features in the faint phase. However, subtraction of earlier type M-dwarf spectra also did not prove successful in removing the hump at 6600 Å.

Thomas et al. (1999) reported seeing cyclotron humps at $\lambda\lambda$ 5100 & 6600 Å in their
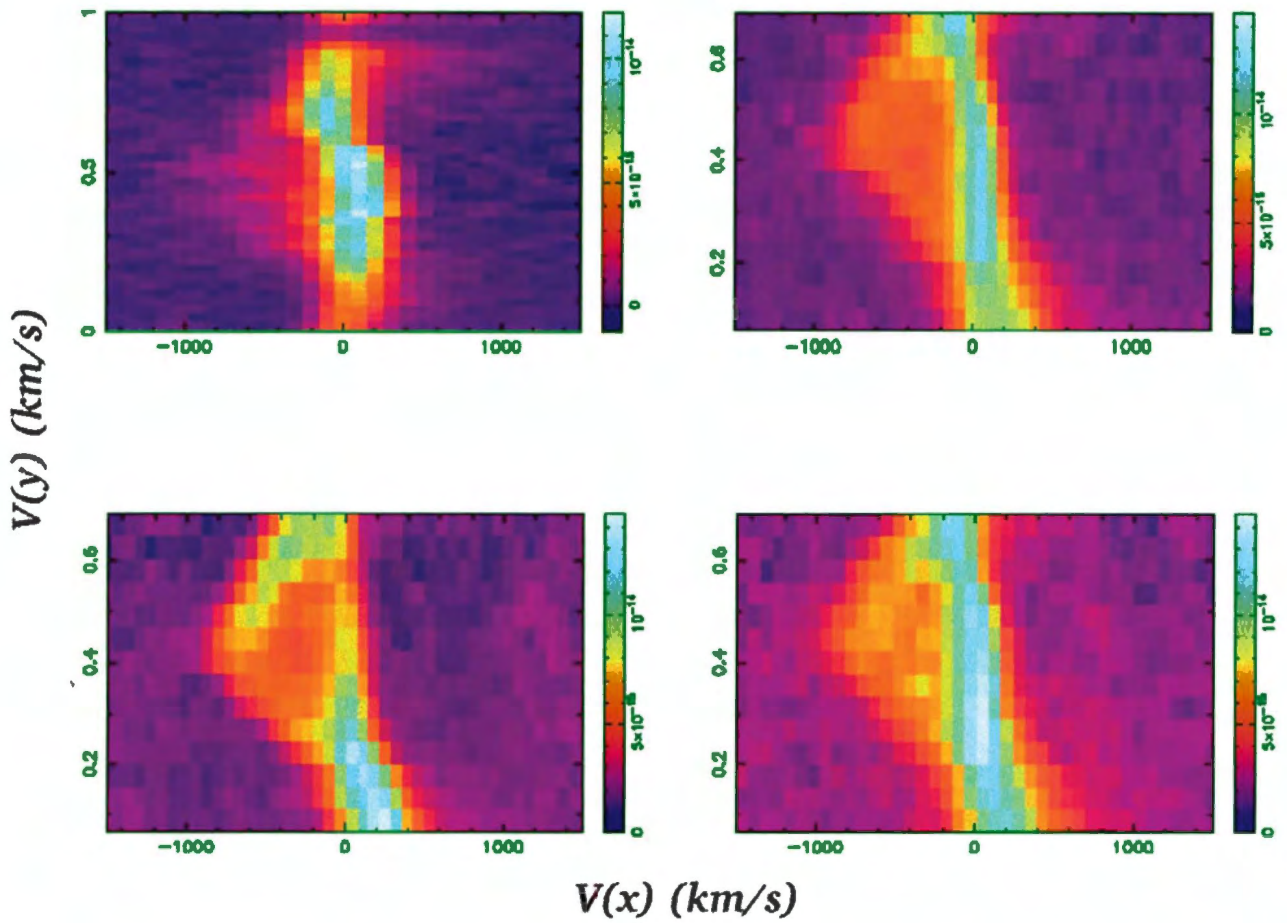
Figure 7.24: RXJ 1313-32 trailed spectrograms for Hα & Hβ (from left to right) are plotted in the top column and HeII λ4686 & Hγ in the bottom column.
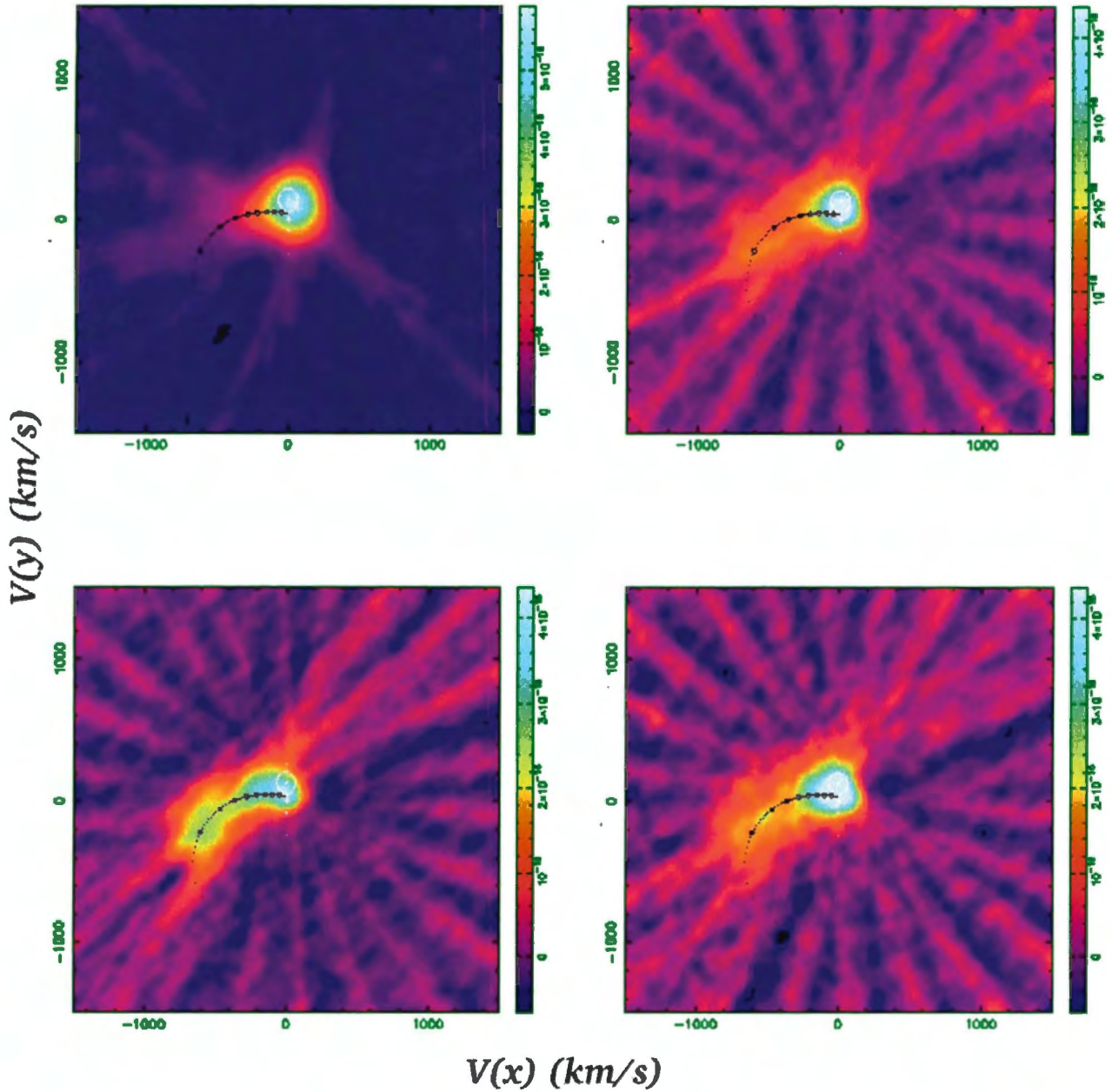
Figure 7.25: RX J1313-32 Doppler tomograms for Hα & Hβ (from left to right) are plotted in the top row and HeII λ4686 & Hγ in the bottom row. Calculated Roche lobes and ballistic trajectory for a mass ratio = $M_2/M_1 = 0.6$ ($K_1 = 82$, $K_2 = 135$ km s^{-1}) are also overplotted. The tomograms for Hβ, He 4686 & Hγ are on plotted on the same intensity scale.
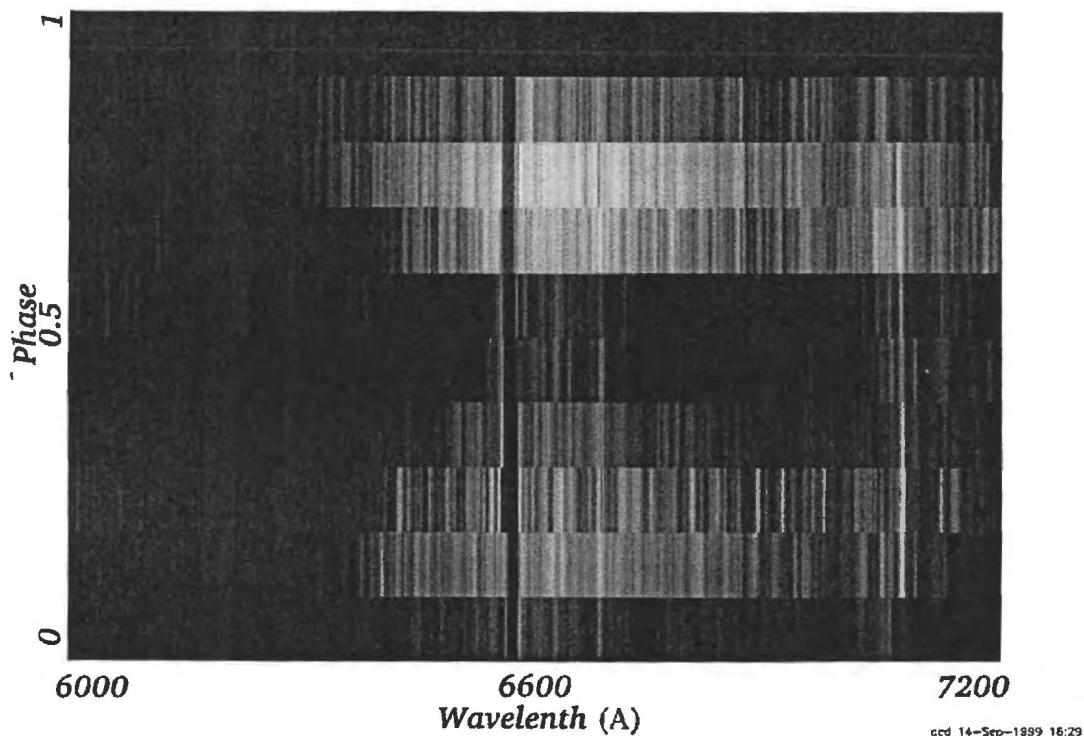
Figure 7.26: Trailed spectrogram for the hump at 6600 Å in RX J1313-32. The Hα emission line has been removed beforehand.

spectropolarimetric data. No hump was visible at 5100 Å in our August 1999 blue data, but the data have a high spectral resolution and does not give full orbital coverage. Low resolution blue data are needed to search for cyclotron humps at 5100 Å, but the fact that the subtraction of earlier M-star spectra did not remove the hump at 6600 Å could possibly confirm that it is a cyclotron harmonic as suggested by Thomas et al. (1999).

7.3.7 Discussion and conclusion

RX J1313.2-3259 is a new Polar with an orbital period of ∼250 min, which makes it the fourth longest orbital period system. Long orbital period systems are important for investigating conditions and mechanisms that maintain synchronism. Its secondary, which dominates the red spectral range, has been determined to be a dM3.5 star. Knowing the spectral type makes it possible to determine the distance to the system.

The Doppler maps are typical for Polars and show a compact bright spot centred where we would expected to find emission from the secondary star and a cometary tail like feature which is associated with emission from the accretion stream. Doppler maps could be used to verify the white dwarf and secondary mass as determined by Thomas et al. (1999) by comparing the maps with the calculated Roche lobe and ballistic stream positions (see Section 4.3.2), but data with high spectral and phase resolution ($\Delta\phi \leq 0.025$) are needed to do these further Doppler tomographical studies of this system.

A hump detected at $\lambda6600$ Å could possibly be a cyclotron harmonic. Future observations involving low resolution blue and red spectroscopy are planned which would facilitate the search for cyclotron harmonics and hence determination of the magnetic
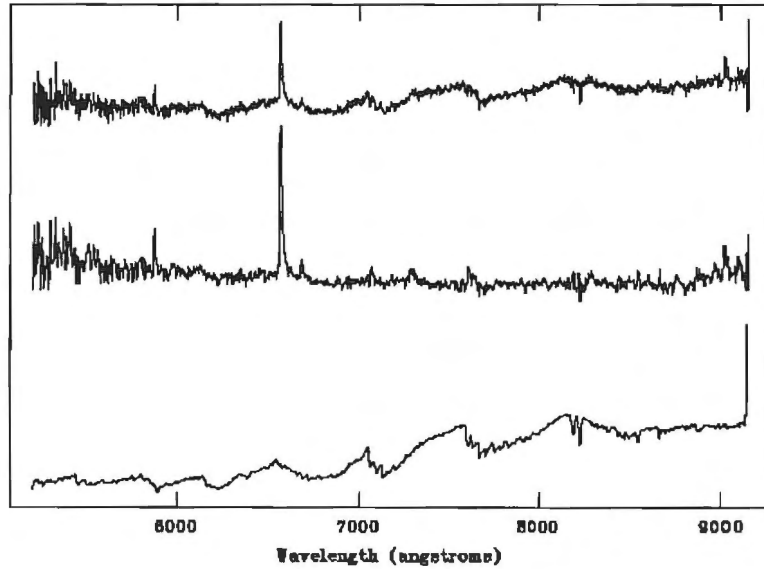
Figure 7.27: Decomposition of a mean faint phase RX J1313-32 spectrum into M-dwarf template and residual component. The upper trace is mean faint phase spectrum, the lower trace is a spectrum of GL 273 (M3.5). The middle spectrum is the observed spectrum minus the scaled M-dwarf spectrum. The vertical scale is arbitrary, and the spectra are offset to avoid overlap.
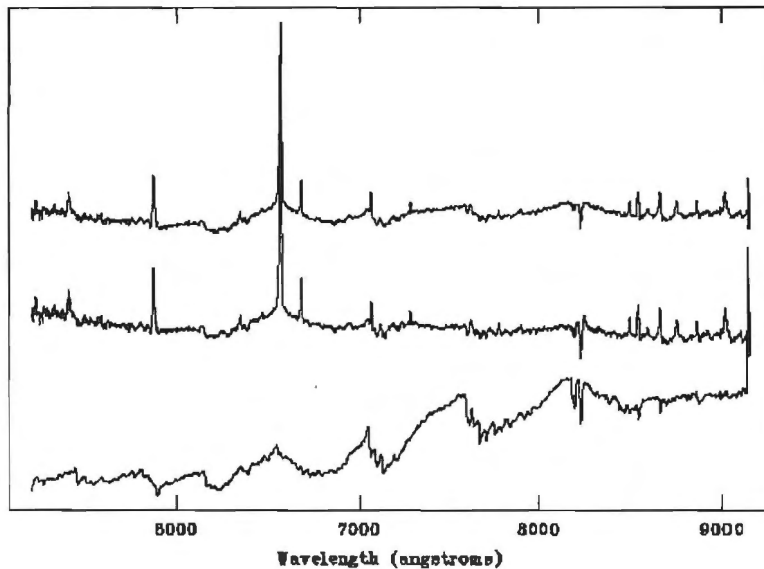
Figure 7.28: The same as for Fig. 7.27, but here the upper trace is a mean bright phase spectrum.

field characteristics. In addition to the spectroscopy we have already obtained a good polarimetric data set (from photoelectric and CCD polarimetry), from which it will be possible to determine magnetic field characteristics (the polarimetry does not form part of this thesis).

7.4 RX J1141.3-6410

7.4.1 Introduction

RX J1141.3-6410 was selected by Motch et al. (1996) for further study in their Galactic plane sample on the basis of its soft X-ray spectrum. They identified it with a V ∼ 16.5 star with strong HeII λ4686 emission lines in its spectra, and this, together with the X-ray hardness ratio, led them to suggest that the star is a Polar. Cieslinski & Stiener (1997) established a photometric period of 3.15 hr, later Rodrigues, Cieslinski, & Stiener (1998) obtained follow up polarization (circular only) and spectroscopy confirming its membership of the class. Buckley et al. (1999) subsequently carried out detailed polarimetric observations (circular and linear) in two wavebands and spectroscopic observations to investigate its nature in more detail. In the following sections I present only the results of the spectroscopic data obtained at the SAAO. For more information on this system see Buckley et al. (1999).

7.4.2 Observations

A sequence of 15 spectra, giving a coverage of ∼1.2 orbital cycles, were obtained on 29 March 1998 at the SAAO (for more details see Table 6.2 & 7.1). The reductions followed the process are described in Section 6.3.

7.4.3 Results

The mean RX J1141-64 spectrum shown in Fig. 7.29 is a rich emission line spectrum dominated by Hα together with HeI, HeII and lines of the Paschen series, which is typical for a magnetic CV. The CaII triplet at 8498, 8542 & 8662 Å is also present.

The main purpose for these observations was to extend the spectral coverage into the near-IR in order to investigate the behavior of the cyclotron flux. In earlier data (Buckley et al. 1999) covering the region 5500-8200 Å, there was an indication of an up-turn in the flux towards longer wavelengths, indicative of cyclotron emission. No cyclotron humps were detected in the spectra, however the trailed spectrogram in Fig. 7.30 shows that there are changes in the spectral slope over the orbital period, indicative of cyclotron emission. In particular the cyclotron spectra rises and peaks at ∼8200 Å with increasing intensity during the bright phase. Some spectra show evidence of a roll-over to lower flux at longer wavelength.
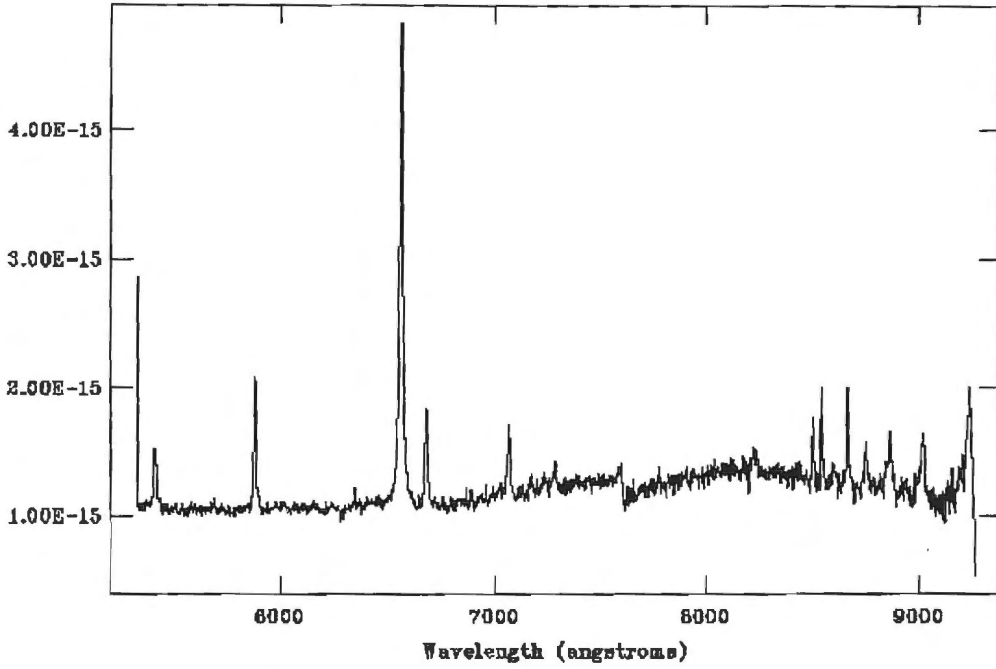
Figure 7.29: The mean spectrum of RX J1141.3-6410 obtained March 1998.
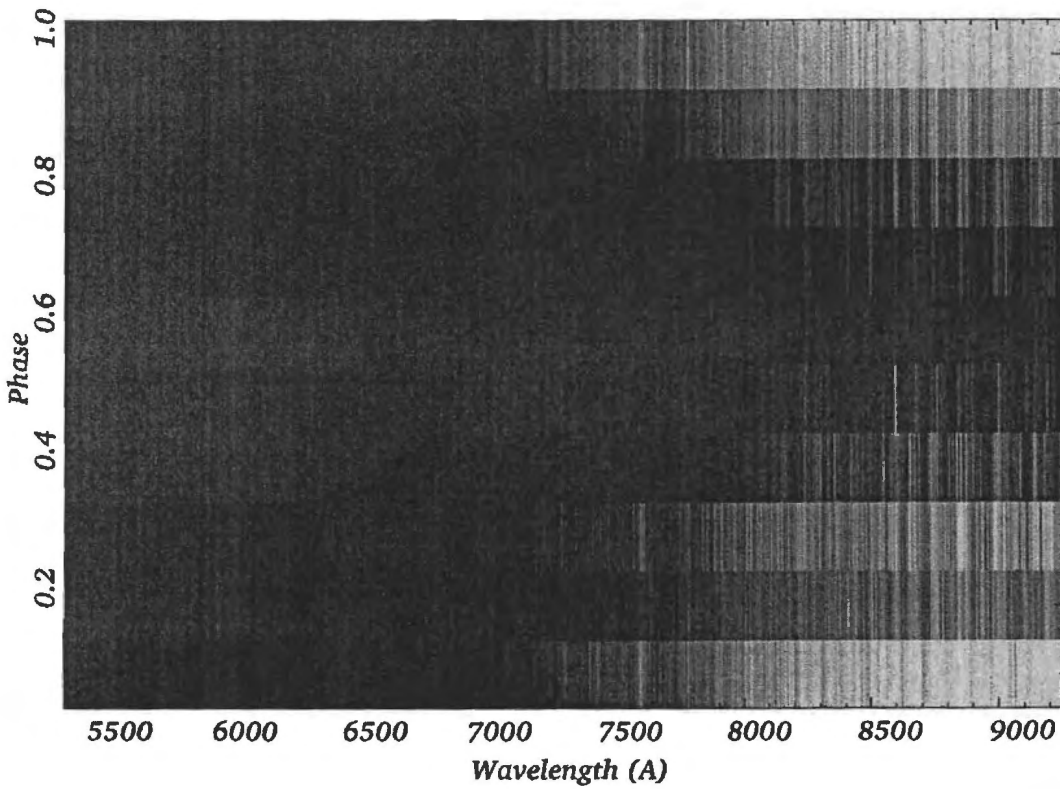
Figure 7.30: RX J1141.3-6410 trailed spectra with emission lines removed.

106

7.5 Miscellaneous mCV systems

In addition to the systems presented in the previous sections, a number of other new mCVs were also observed. Due to a variety of reasons (e.g. bad weather, objects were too faint, data acquisition software problems, etc.) it was not possible to obtain extensive observations, particularly time resolved spectroscopy. Table 7.9 provides a list of the objects observed, while a more detailed observing log is supplied in Table 7.1.

While all these objects were selected for observations because they are all new mCV systems, RX J0501-03 and RX J0515+01 are particularly interesting cases. RX J0501-03 is a new $V_{mag} \sim 17$ eclipsing Polar discovered by the RASS. A period of $P \sim 2.85$ hrs places this system at the upper edge of the period gap for CVs (Burwitz et al. 1998). RX J0515+01 is an eclipsing Polar with the longest known period ($P \sim 8$ hrs) for a Polar (Shafter et al. 1995b). As mentioned in Section 7.3, long period systems are important in order to investigate the conditions and mechanisms that maintain synchronism.

RX J0501-03 and RX J0512-72 were only observed in the red and were too faint to obtain very useful spectra. RX J0153-59 and RX J0515+01 were in a high accretion state and their spectra show strong emission lines of the H-Balmer series together with HeI and HeII lines. The HeII λ4686 emission line is prominent in both of these systems. RX J1610+03 (RBS 1563) also shows H-Balmer (Hα & Hβ) and HeI emission. Strong TiO bands are also clearly visible at λ 6195, 6322, 6651 & 7051 Å. Fig. 7.31 show the mean spectra for the five objects, while a list of emission line equivalent width measurements (for the systems with stronger emission) are given in Table 7.10. No obvious cyclotron humps are visible in these spectra. RX J0515+01 does not show the cyclotron lines at 5900 & 8500 Å, as seen by Shafter et al. (1995b) in their data. There appears to be a hump at 4500 Å, but this feature is also seen in the Shafter et al. (1995b) eclipse spectra and is most likely a secondary star feature.

Table 7.9: A list of new and interesting objects observed.

Object	α_{2000} h m s	δ_{2000} ° ' "	λ range Å	Res. Å
RX J1610+03	16 10 08	03 52 33	4680-9263	5
RX J0153-59	01 54 01	-59 47 39	3568-5493	2
			5200-9140	5
RX J0501-03	05 01 46	-03 59 32	5200-9140	5
RX J0512-72	05 12 13	-72 41 39	5200-9140	5
RX J0515+01	05 15 40	01 04 32	3630-5555	2
			5200-9140	5

Table 7.10: Equivalent width measurements for various emission lines.

Object	E.W.			
	Hα	Hβ	HeII λ4686	Hγ
RX J1610+03	72	65	-	-
RX J0153-59	124	109	84	100
RX J0515+01	28	20	24	21

Figure 7.31: Mean spectra for RXJ J1610+03, RX J0153-59, RX J0501-03, RX J0512-72, RX J0515+01 (blue) and RX J0515+01 (red).

7.6 RBS 0324

7.6.1 Introduction

RBS 0324 was selected as a candidate mCV from the ROSAT Bright Survey (e.g. Fischer et al. 1998). The optical counterpart has been identi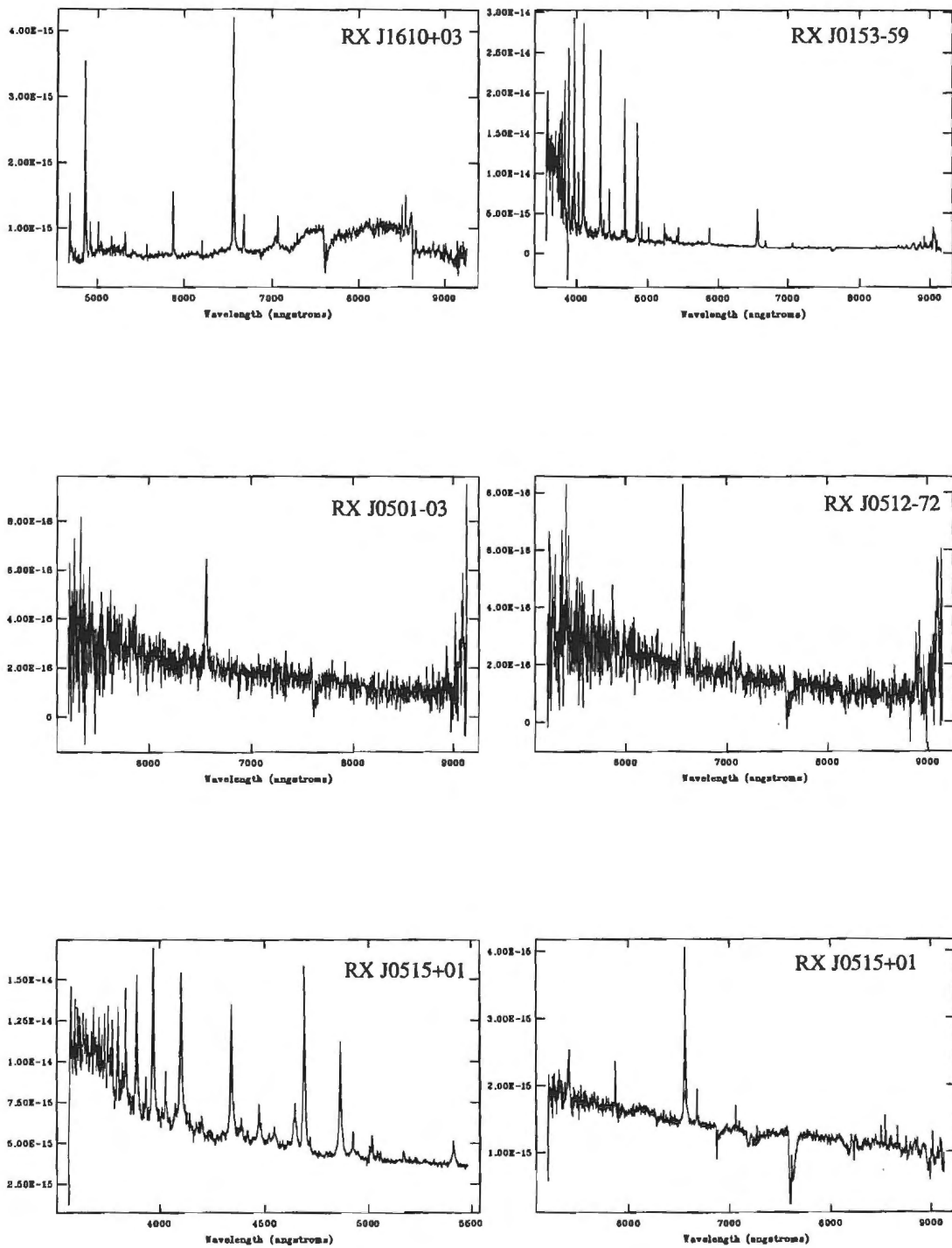fied as a $V_{mag} \sim 16.7$ star. I present optical photometry and spectroscopy which indicates that RBS 0324 is a new Polar.

7.6.2 Observations

7.6.2.1 CCD photometry

White light photometric observations of RBS 0324 were obtained on 2 nights in January 1999 on the 1.0-m Elizabeth telescope at Sutherland using the Tek8 CCD camera, using a Tektronics CCD with 512×512 pixels and a pixel size of 27 μm. The observations were made over a time span HJD 2451191.328630 - 2451191.446810 on 12 January 1999 and HJD 2451193.307950 - 2451193.491810 on 14 January 1999. A 2×2 on-chip binning scheme was applied for both nights. All CCD frames were bias-subtracted and flat fielded and differential photometry was derived using DoPhot (Mateo & Schechter 1989).The stability of the photometry was checked from the stability of flux differences of the comparison stars (a selection of non-variable bright stars in the field).

7.6.2.2 Spectroscopy

Time resolved (a sequence of 14 spectra) low resolution blue spectroscopy of RBS 0324 was obtained on 21 January 1999. These observations gives total phase coverage, assuming period as detailed below. Low resolution red spectroscopy and higher resolution blue spectroscopy were attempted over several observing runs (see Table 6.1), but the system was in a Low-state and thus too faint to obtain data with good signal-to-noise ratio. See Tables 6.2 & 7.1 for a full observing record. The reduction procedure followed that described in Section 6.3.

7.6.3 Results

7.6.3.1 CCD photometry

RBS 0324 was found to display changes of the overall brightness level over the observed time span, as demonstrated in the light curves shown in Fig. 7.32. The most obvious feature of the light curves is a quasi-sinusoidal variation with a full orbital amplitude of $\sim$ 1.7 mag. The modulation in the data is most probably due to cyclotron beaming (see Section 7.6.3) and the shape of the light curve could most likely be explained by the shape, size and location of the accretion region.

Based on the combined data for the 2 nights, a full least-squares periodogram analysis yields a period of P = 0.126245 days and a least-squares sine fit to the data was used to determine the optical maximum to yield an ephemeris :

$$HJD_{(maximum)} = 2451191.3117(18) + 0.126245(62) \times E \qquad (7.1)$$

where the last numbers in the brackets represent the uncertainties in the last digits. Fig. 7.33 shows the phase folded data using the period P = 0.126245 days.
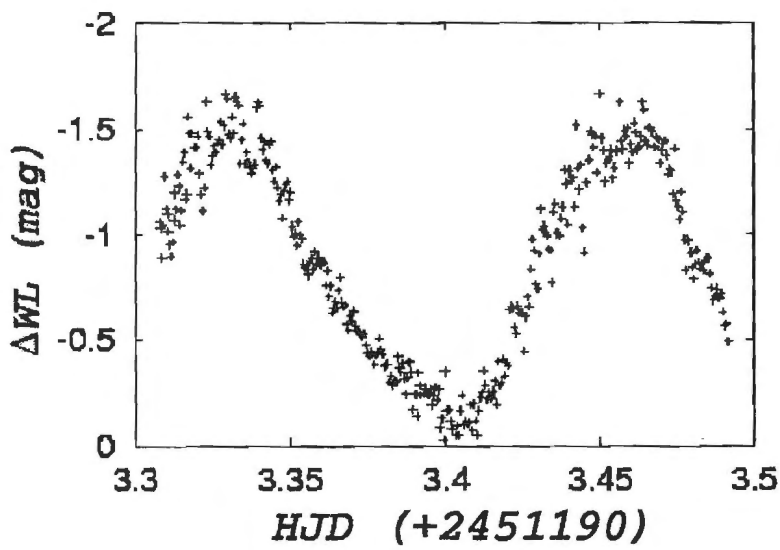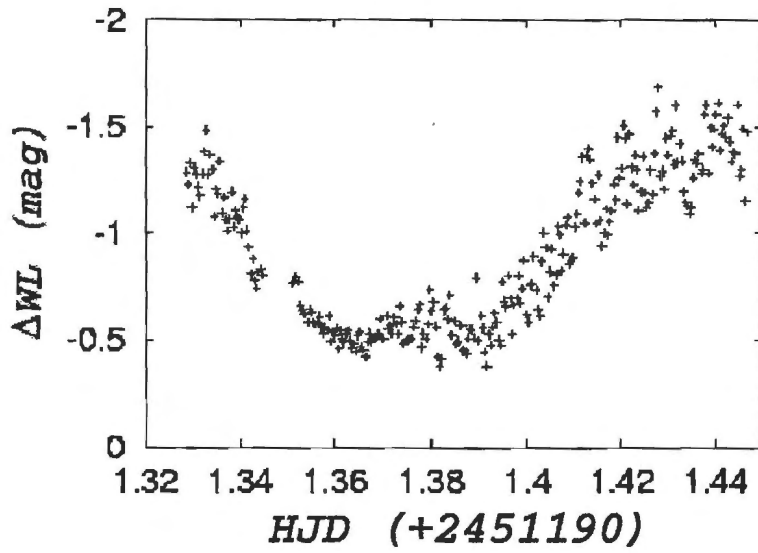
Figure 7.32: White light CCD photometry for RBS 0324 obtained on 12 January 1999 (upper plot) and 14 January 1999 (lower plot).
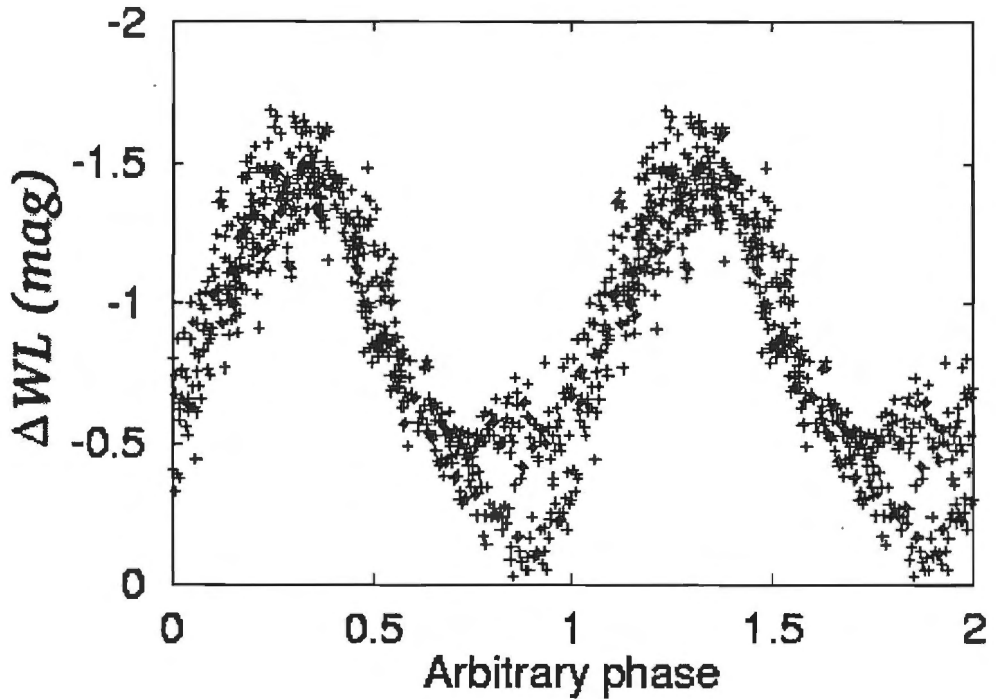
Figure 7.33: Combined differential photometry for RBS 0324 obtained on 12 & 14 January 1999 plotted as a function of arbitrary phase (P = 0.126245 days). The data are plotted twice for clarity.

7.6.3.2 Spectroscopy

A mean low resolution bright phase spectrum of RBS 0324 is shown in Fig. 7.35 and a mean faint phase spectrum shown in Fig. 7.34. The spectrum of RBS 0324 shows the typical emission line (strong Balmer, HeI and HeII) found in Polars. Gaussian fits to Hβ and HeII λ4686 emission lines yield equivalent widths EW(Hβ) = 33 Å & EW(HeII λ4686) = 20 Å and a ratio EW(HeII λ4686)/EW(Hβ) = 0.66 which is typical for a magnetic CV (see Section 6.4.1). The continuum in the faint phase spectra is essentially flat while the bright phase data show a broad hump in the continuum. The appearance of the hump is explained as the contribution of cyclotron radiation from the accretion region. A mean faint phase spectrum has been subtracted from the spectroscopic data and is represented in Fig. 7.36 as a greyscale trailed spectrogram. Here it can be seen that the cyclotron hump is centred at phase $\phi = 0$, which is the optical maximum. The optical maximum is thus interpreted is being due to cyclotron beaming.

Radial velocities were determined using a Gaussian convolution scheme using seven Gaussian "filters" with separations of 2000, 1500, 1200, 900, 700, 500 and 200 km s^{-1}, and corresponding Gaussian sigmas of 400, 250, 200, 200, 200, 200 and 200 km s^{-1}. Each radial velocity curve was phased using the ephemeris given in (7.1) and the amplitude (K-velocity), zero-level (γ-velocity) and phase offset (ϕ_0) was determined by fitting Equation 4.1, by using a nonlinear least-squares algorithm. Figs. 7.37, 7.38 & 7.39 shows the velocity curves for the Hα, Hβ and HeII λ4686 lines, together with their best-fit sinusoids, while the fit parameters are listed in Tables 7.11, 7.12 & 7.13

From the tables and radial velocity plots it can be seen that the K-velocity increases

111
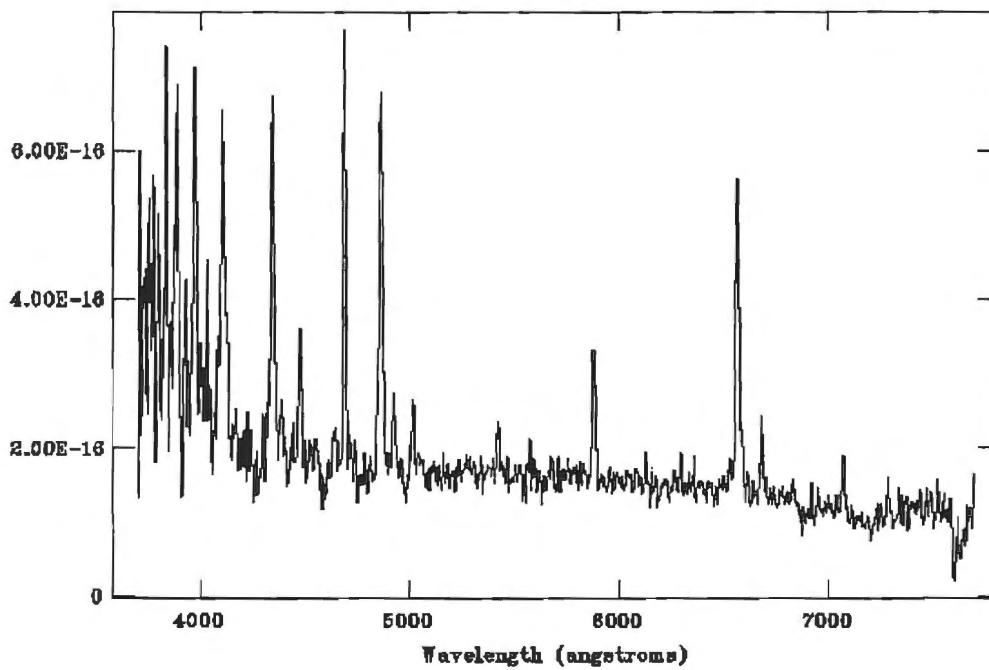
Figure 7.34: A mean faint phase spectrum for RBS 0324 on 21 January 1999.
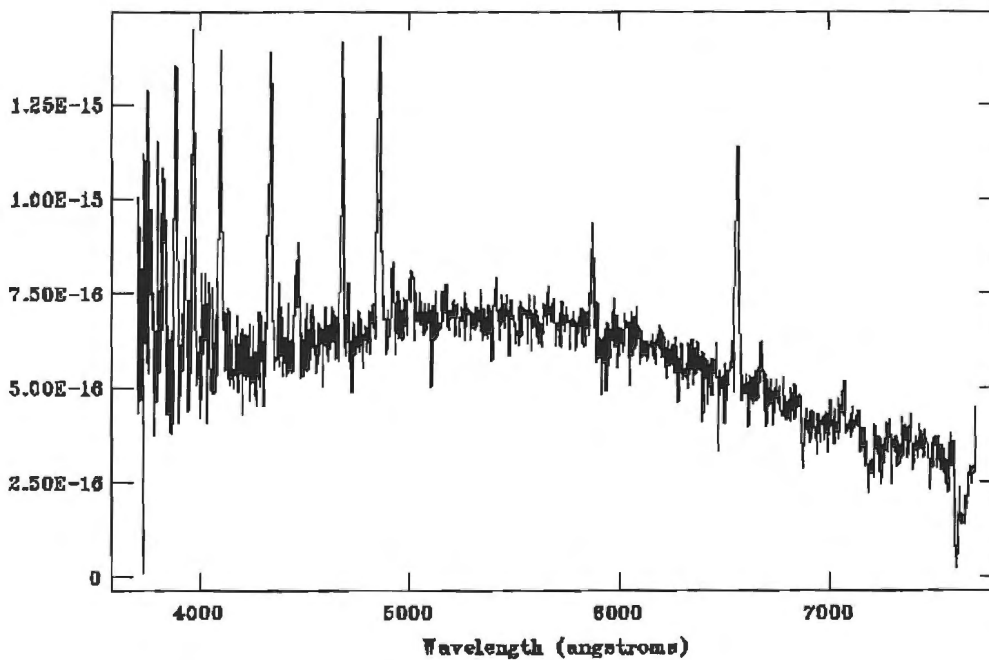
Figure 7.35: A mean bright phase spectrum for RBS 0324 on 21 January 1999.

112
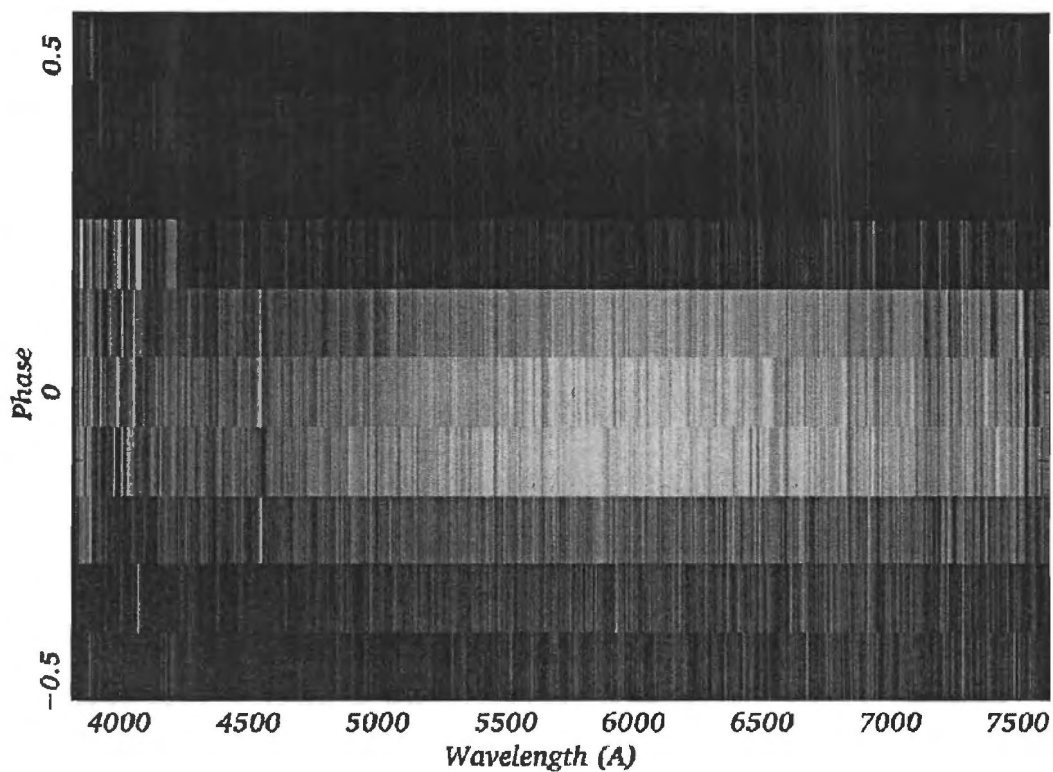
Figure 7.36: A greyscale trailed spectrogram for RBS 0324, with a mean faint phase spectrum subtracted from the data. The phase dependent movement of the cyclotron hump (centred about $\phi = 0$) can be clearly seen.

Table 7.11: Variation in Hα radial velocity parameters for RBS 0324.

sep km s^{-1}	FWHM km s^{-1}	γ-velocity km s^{-1}	K-velocity km s^{-1}	Phase offset
200	200	249.45	109.61	0.36
500	200	257.40	148.20	0.29
700	200	248.03	185.64	0.26
900	200	233.36	227.72	0.24
1200	200	222.53	253.74	0.20
1500	250	204.03	256.78	0.17
2000	400	213.55	377.19	0.12
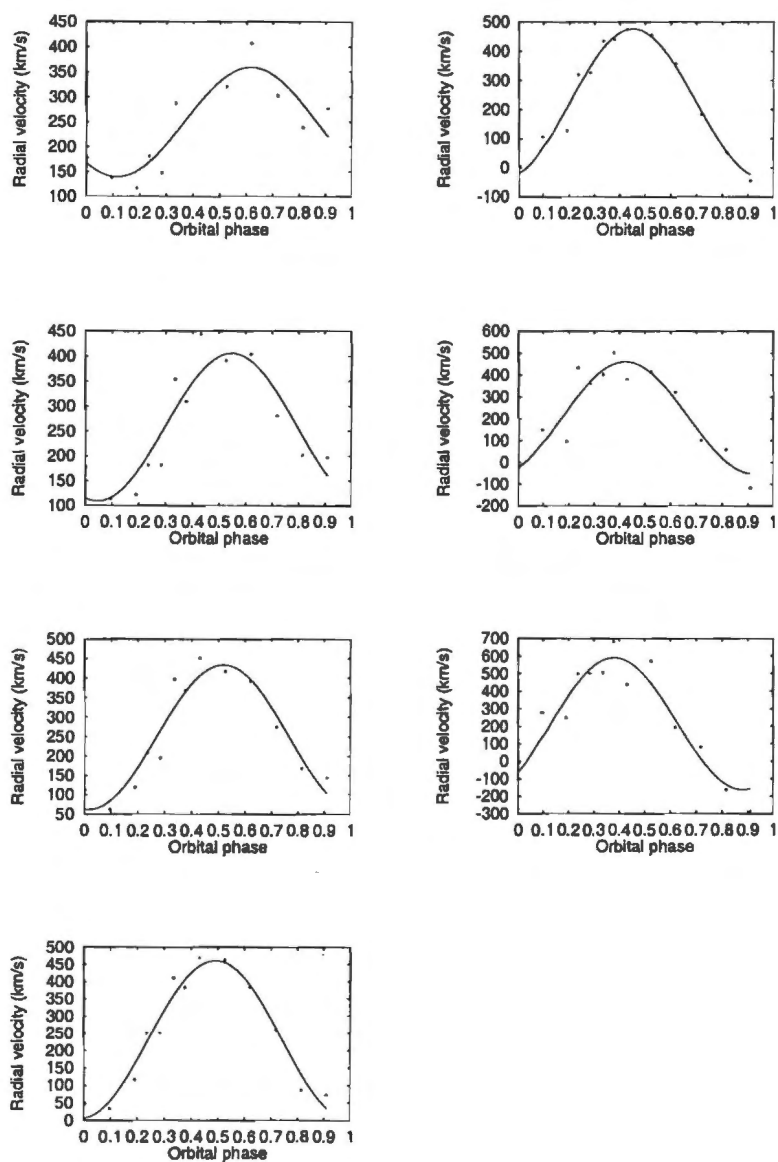
Figure 7.37: RBS 0324 RV curves for Hα with Gaussian separations of 200, 500, 700 and 900 km s⁻¹ is plotted in the first column (from top to bottom) and 1200, 1500 and 2000 km s⁻¹ is plotted in the second column.
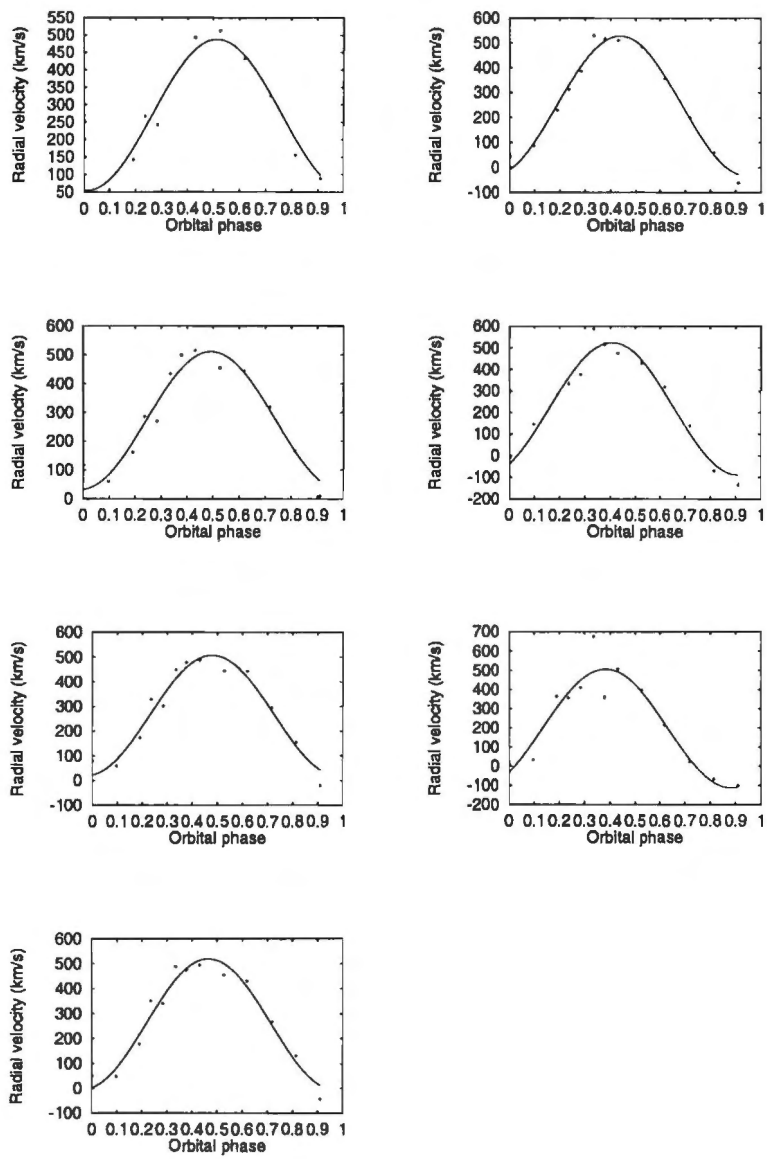
Figure 7.38: Same as for Fig. 7.37, but for Hβ.
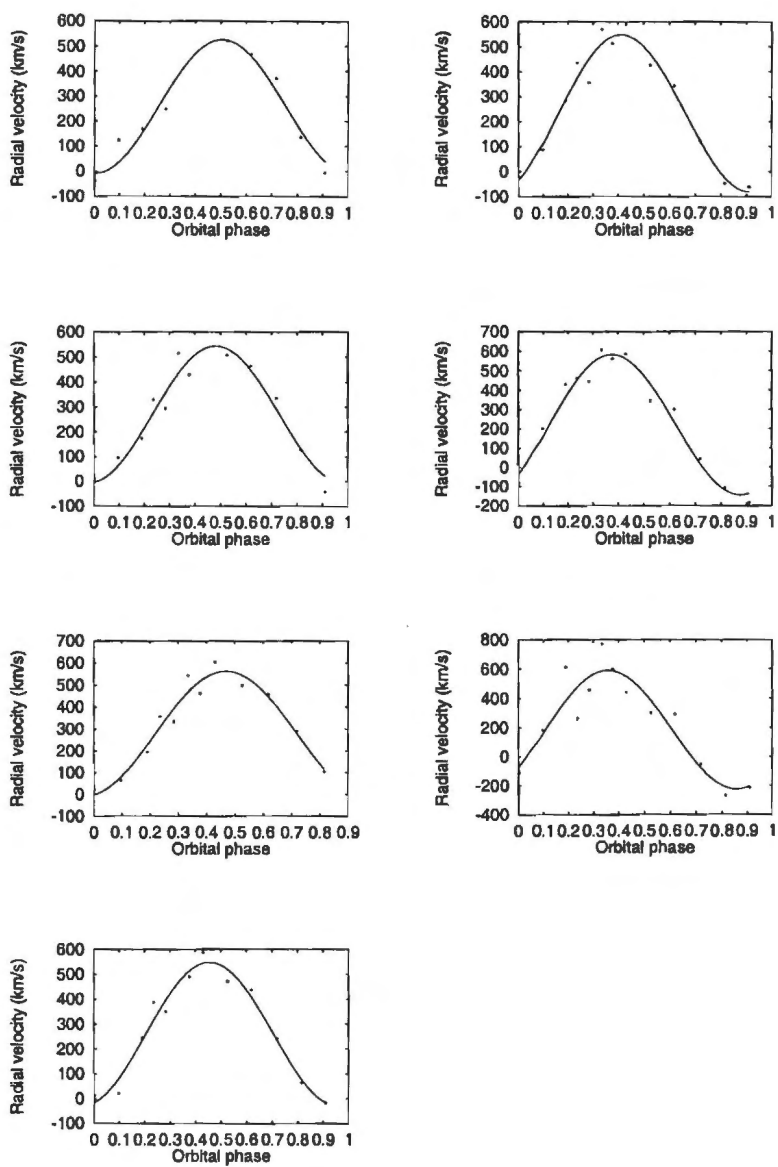
Figure 7.39: Same as for Fig. 7.37, but for HeII $\lambda 4686$.

Table 7.12: Variation in Hβ radial velocity parameters for RBS 0324.

sep km s^{-1}	FWHM km s^{-1}	γ-velocity km s^{-1}	K-velocity km s^{-1}	Phase offset
200	200	270.91	216.58	0.26
500	200	271.54	239.16	0.24
700	200	263.19	243.21	0.23
900	200	257.65	261.18	0.24
1200	200	248.19	279.46	0.19
1500	250	217.48	306.16	0.16
2000	400	195.85	309.12	0.13

Table 7.13: Variation in HeII λ4686 radial velocity parameters for RBS 0324.

sep km s^{-1}	FWHM km s^{-1}	γ-velocity km s^{-1}	K-velocity km s^{-1}	Phase offset
200	200	259.35	267.18	0.25
500	200	269.07	274.81	0.23
700	200	278.11	285.07	0.22
900	200	260.14	287.11	0.21
1200	200	233.28	314.72	0.16
1500	250	219.09	363.38	0.12
2000	400	183.18	407.65	0.10

into the wings up to a value ~ 400 km s^{-1} (for HeII λ4686). There is also a shift as a function of Gaussian separation, with the phase offsets decreasing from ~ 0.26 for the line centers to ~ 0.1 for the line wings. The decreasing phase offsets indicate that the broader line components lead the narrower components in phase, which is what is expected from a curved accretion stream (see Fig. 4.1). These offsets are with respect to the optical maximum, thus the optical maximum leads the narrower component in phase by ~ 0.26 The broader components, which usually arises from the magnetically channeled part of the accretion stream, more or less coincides in phase with the optical maximum, which is further proof that the optical maximum is due to cyclotron radiation from the accretion region. In addition there is also a trend of decreasing γ-velocity as we move into the line wings, which could be due to out of plane movement toward the observer. The γ-velocities ($\gtrsim 200$ km s^{-1}) are also very high.

7.6.4   Discussion and conclusion

The data presented in the previous section suggest that RBS 0324 is a Polar. The strongest proof is the presence of a broad cyclotron hump in the continuum of the bright phase spectra. The hump coincides with the optical maximum, which suggests that the modulation in the light curve is due to cyclotron beaming. Further evidence that this system is a Polar is from a single polarimetric measurement which indicates that this system is polarized; however, the polarimetry does not form part of this thesis.

The orbital period ($P \sim 3.03$ hr) puts this system just above the period gap for

CVs. Fits to the radial velocity measurement seem to agree with the photometric period. However, the spectroscopic data presented in this thesis are not of sufficient quality (i.e. phase or spectral resolution) to constrain a particular spectroscopic period. We attempted to obtain spectra during the August 1998 and February 1999 observing runs, but system was in a low accretion state and thus too faint to observe. Better spectral and phase resolved spectra are needed to search for evidence of asynchronism which could be achieved if the photometric period is regarded as the white dwarf spin period and the the spectral period is regarded as the true orbital period. Radial velocity and intensity variations of the different emission line velocity components could also be compared with the photometric features to determine the system geometry (inclination, location of accretion region, etc).

Future spectroscopic and polarimetric observations, which could help constrain parameters such as the magnetic field strength and location and shape of the accretion region, are planned to investigate this system further.

7.7 Non-magnetic systems

During our spectroscopy observing run from 18-24 August 1998, we selected six stars from the RBS list that were observable at that time. Out of these seven objects only one showed evidence of being a magnetic CV (viz. RBS 0324 see section 7.6), three stars are most probably disc CVs (viz. RBS 0372, RBS 0490 & RBS 1969) and two stars (RBS 0541 & RBS 1955) were too faint to observe. More information on these systems are given in Table 7.14. In this section I report on the three non-magnetic systems observed.

7.7.1 Observations

RBS 0372, RBS 0490 & RBS 1969 were observed during the August 1998 run. Most of the spectra were obtained using grating No.6, giving a wavelength range extending from 3600 to 5600 Å at a resolution of ~2 Å. Some red spectroscopy of RBS 1969 was also obtained using grating No.8 giving a wavelength range 6300-8600 Å at resolution of ~4 Å. Low resolution red spectroscopy of RBS 0541, RBS 1563 & RBS 1955 were also attempted, but the systems were too faint. In addition spectra of RBS 1969 was obtained in January 1999. A detailed observing log for these three objects is listed in Tables 6.2 & 7.1. The reductions followed the procedure described in Section 6.3

7.7.2 Results

RBS 0372, RBS 0490 & RBS 1969 show emission lines of H, HeI and weak HeII $\lambda4686$ together with Balmer continuum in emission (see Figs. 7.40 to 7.43) which is typical spectral features for dwarf novae in quiescence. In addition RBS 0372 & RBS 1969 (Figs. 7.42 & 7.42) show double peaked emission lines typical of high inclination disc systems. Gaussian fits were made to the $H\beta$ and HeII $\lambda4686$ emission lines and the parameters recorded in Table 7.15. All three systems show very weak HeII $\lambda4686$ with the ratio EW(HeII)/EW($H\beta$) ≤ 0.25. According to "Silber's rule" (see Section 6.4.1) this indicates that these systems are non-magnetic in nature.

7.7.3 Conclusion

Data on the three RBS systems RBS 0372, RBS 0490 and RBS 1969 were presented in the previous section. From the strength of the HeII $\lambda4686$ emission line and equivalent widths of the $H\beta$ and HeII $\lambda4686$ lines it was concluded that these systems are non-magnetic. Hard X-rays have been detected from most bright (nearby) dwarf novae at quiescence (Warner 1995). The RBS systems are all high-galactic-latitude X-ray sources, which means low absorption, so that nearby dwarf novae in quiescence could be detected by ROSAT. RBS 0372, RBS 0490 and RBS 1969 are thus most likely dwarf novae in quiescence.

Table 7.14: List of ROSAT bright source objects observed.

Object	α_{2000} h m s	δ_{2000} ° ' "	V_{mag}	Magnetic
RBS 0324	02 30 52.9	-68 42 03	~ 16.7	Yes
RBS 0372	02 55 38.2	-22 46 55	~ 17.6	No
RBS 0490	03 54 10.4	-16 52 44	~ 17.0	No
RBS 0541	04 25 55.8	-19 45 34	~ 16.5	??
RBS 1955	23 09 49.6	+21 35 23	~ 16.1	??
RBS 1969	23 15 32.3	-30 48 55	~ 16.6	No

Table 7.15: List of parameters from Gaussian fits to Hβ & HeII 4686

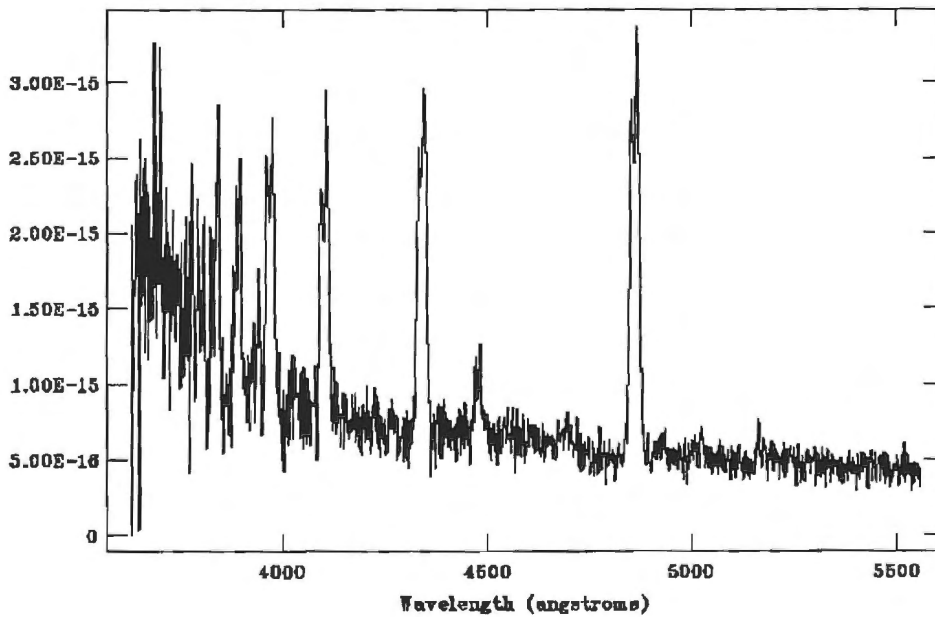| Object	FWHM Å	E.W. Å	Flux mJy	FWHM Å	E.W. Å	Flux mJy	E.W.(HeII 4686)/ E.W.(Hβ)
		Hβ			HeII 4686		
RBS 0372	24	138	7E-14	58	18	8.5e-15	0.13
RBS 0490	16	227	1.3E-14	52	55	1.8E-14	0.25
RBS 1969	36	71	7.5E-14	79	13	1.5E-14	0.18

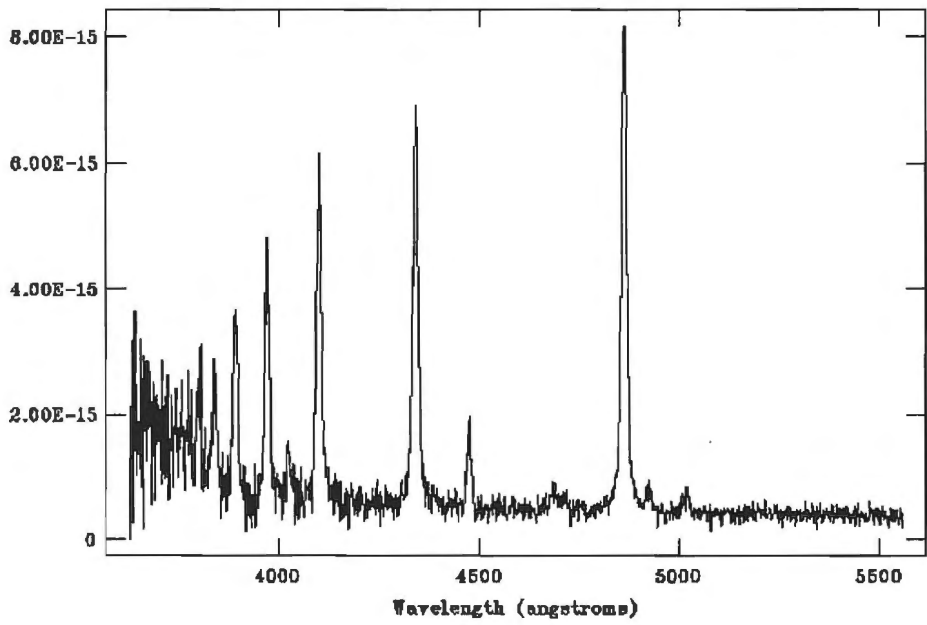Figure 7.40: Mean combined spectrum (grating No.6) of RBS 0372

Figure 7.41: Mean combined spectrum (grating No.6) of RBS 0490
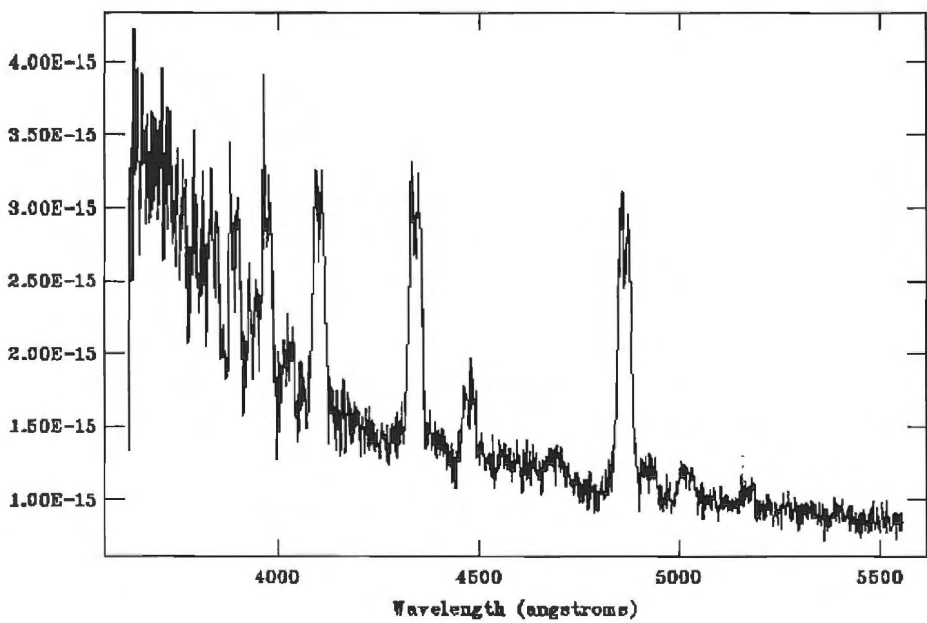

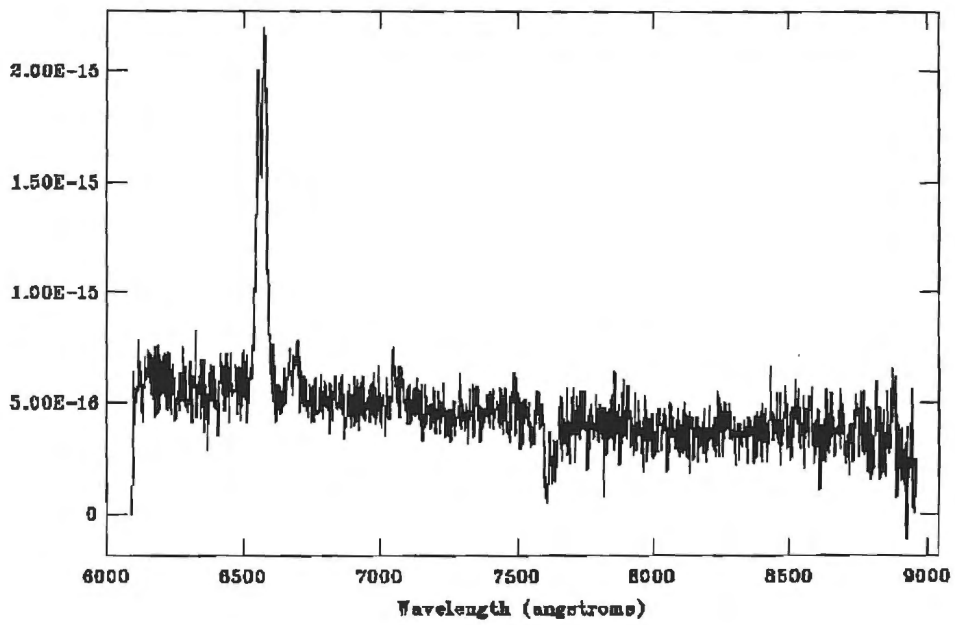Figure 7.42: Mean combined spectrum (grating No.6) of RBS 1969

Figure 7.43: Mean combined spectrum (grating No.8) of RBS 1969

Chapter 8

Summary and Outlook

In this chapter I summarize the results obtained for individual objects and provide a brief outlook on advances expected in the field of magnetic cataclysmic variables at the SAAO.

8.1   Summary

HU Aqr: HU Aqr is the brightest eclipsing Polar, and is an excellent candidate for Doppler tomography. The Doppler maps shows a compact bright spot and cometary tail like feature which is associated with the heated face of the secondary and the accretion stream respectively. In addition, a third faint feature is associated with the magnetically channeled accretion stream. The two cyclotron humps detected indicate a magnetic field strength of $B = 39$ MG.

QS Tel: QS Tel exhibit two sets of cyclotron lines originating from two accretion regions on the white dwarf. Lines originating from the second pole is more evident than in previous studies. Magnetic field strength determination indicate fields of $B \simeq 65$ & 45 MG.

RX J1313-32: The secondary star, which dominates the red spectral range, has been estimated to be a dM3.5 star. The spectra show all the emission lines associated with a Polar and these are multicomponent in nature. The Doppler maps show a compact bright spot and cometary tail like feature which is associated with the heated face of the secondary and the accretion stream respectively. A hump in the continuum at ~ 6000 Å could possibly be a cyclotron line.

RX J1141-64: Shows spectral slope changes over the orbital period indicative of cyclotron emission at long wavelengths.

Miscellaneous mCV systems: The spectra of the new systems RX J1610+03, RX J0153-59, RX J0501-03, RX J0512-72 and RX J0515+01 are presented, but these shows no indication of cyclotron humps.

RBS 0324: This is the only confirmed mCV of the four RBS sources observed with reasonable signal-to-noise. The photometric period has been determined to be $P = 3.03$ hr. The spectra show multicomponent emission lines usually associated with Polars. The spectra show a broad cyclotron hump which coincides with optical maximum.

RBS 0372, RBS 0490 & RBS 1969: These objects are most likely dwarf novae in quiescence. The non-magnetic nature of these objects was inferred from the weak HeII $\lambda 4868$ emission lines. The spectra of RBS 0372 & RBS 1969 show double peaked emission lines which indicate that these objects are high inclination disc systems.

8.2 Outlook

Observational progress in the field of magnetic CVs at the SAAO is expected with the development of a new spectrograph camera and two channel photoelectric polarimeter. A new spectrograph camera is expected to be 50% more efficient compared with the existing camera. The advent of the new camera will allow the opportunity to obtain higher signal-to-noise and phase resolved spectroscopic data which are needed for Doppler tomographical studies. The improved sensitivity will also aid in the search for cyclotron features, especially in the fainter systems.

The two channel polarimeter will enable us to get two wavebands simultaneously, which will in effect double our efficiency (compared with the old single channel UCT polarimeter) for observing magnetic CVs. This is important because it will give us a better idea of the cyclotron continuum slope. The upgraded Durham imaging-polarimeter is expected to arrive at the SAAO in the first quarter of next year (Jan-April 2000) and will enable us to observe many more of the fainter systems.

The construction of the Southern African Large Telescope (SALT) is set to commence in the year 2000. SALT will be the southern hemisphere twin of the Hobby-Eberly Telescope (HET) in Texas. This 10-meter class telescope will allow more detailed spectroscopic studies of magnetic CVs at higher time and spectral resolution. This will enable a search for, e.g., activity and conditions in the secondary stars and accretion material by means of Doppler imaging. Spectroscopy with time resolution down to seconds is needed to unravel physical parameters (e.g., temperature and field structure) of the white dwarf (Burwitz 1997).

Bibliography

Bailey J., Cropper M., 1991, MNRAS, 253, 27

Bailey J., Ferrario L., Wickramasinghe D., 1991, MNRAS, 251, 37P

Bailey J., Ferrario L., Wickramasinghe D., Buckley D., Hough J., 1995, MNRAS, 272, 579

Barrett P., Chanmugam G., 1984, ApJ, 278, 298

Barrett P., Chanmugam G., 1985, ApJ, 298, 743

Bekefi G., 1966, Radiation Processes in Plasma Physics. John Wiley and Sons

Bessell M., 1999, private communication

Beuermann K., 1996. in Agrawal P.C., Visvanathan P.K. ed, Perspectives in high energy Astronomy and Astrophysics, University Press, p. 100

Beuermann K., Burwitz V., 1990, A&A, 238, 173

Beuermann K., Thomas H.-C., 1993, Adv. in Space Res., 13, (12)115

Biermann P. et al., 1985, ApJ, 293, 303

Buckley D., Cropper M., van der Heyden K., Potter S., Wickramasinghe D., 1999, MNRAS, in prep

Buckley D., O'Donoghue D., Hassall B., Kellet B., Mason K., Sekiguchi K., Wheatley M., Chen A., 1993, MNRAS, 262, 93

Buckley D., Sekiguchi K., Motch C., O'Donoghue D., Chen A.-L., Schwarzenberg-Czerny A., Pitsch W., Harrop-Allin M., 1995, MNRAS, 275, 1028

Burwitz V., 1997, Ph.D. thesis, Georg-August-Universitat zu Gottingen

Burwitz V., Reinsch K., Beuermann K., Thomas H.-C., 1998. in Hellier C., Mukai K. ed, Annapolis workshop on magnetic cataclysmic variables, A.S.P. Conf. Ser. 157, p. 127

Burwitz V., Reinsch K., Schwope A., Beuermann K., Thomas H.-C., Greiner J., 1996, A&A, 305, 319

Cieslinski D., Stiener J., 1997, MNRAS, 291, 321

Cowley A., Crampton D., 1977, ApJ, 212, L121

Craig N., Howell S., Sirk M., Malini R., 1996, ApJ, 457, L91

Crampton D., Hutchings J., Cowley A., 1980, ApJ, 240, 871

Cropper M., 1988, MNRAS, 231, 597

Cropper M., 1990, Sp. Sci. Rev., 54, 195

Cropper M., Mason K., Mukai K., 1990, MNRAS, 243, 565

Cropper M. et al., 1990, MNRAS, 245, 760

Ferrario L., Bailey J., Wickramasinghe D., 1993, MNRAS, 262, 285

Ferrario L., Bailey J., Wickramasinghe D., 1996, MNRAS, 282, 218

Ferrario L., Wickramasinghe D., 1990, ApJ, 357, 582

Ferrario L., Wickramasinghe D., Bailey J., Buckley D., Hough J., 1994, MNRAS, 268, 128

Ferrario L., Wickramasinghe D., Bailey J., Hough J., Tuohy I., 1992, MNRAS, 256, 252

Ferrario L., Wickramasinghe D., Bailey J., Tuohy I., Hough J., 1989, ApJ, 337, 832

Fischer J.-U., Hasinger G., Schwope A., Brunner H., Boller T., Trümper J., Voges W., Neizvestny S., 1998, Astron. Nachr., 319, 347

Greiner J., Schwarz R., Wenzel W., 1998, MNRAS, 296, 437

Hakala P., Watson M., Vilhu O., Hassall B., Kellett B., Mason K., Piirola V., 1993, MNRAS, 263, 61

Hirshfield J., Baldwin D., Brown S., 1961, Phys. Fluids, 4, 198

Horne K., 1991. in Shafter A. ed.,12th North American Conference on Cataclysmic Variables and related objects, San Diego Univ. Press, p. 23

Kaitchuck R., Schlegel E., Honeycutt R., Horne K., Marsh T., White J., Mansperger C., 1994, ApJS, 93, 519

Kirkpatrick J., Henry T., McCarthy D., 1991, ApJS, 77, 417

Landstreet J., 1992, A&AR, 4, 35

Marsh T., Horne K., 1988, MNRAS, 235, 269

Mateo M., Schechter P., 1989. in Grosbol P.J., Murtagh F. ed, Data analysis workshop, European Southern Observatory, p. 69

McCarthy P., Clarke J., Bower S., 1986, ApJ, 311, 873

Meggit S., Wickramasinghe D., 1982, MNRAS, 198, 71

Montgomery D., Tidman D., 1964, Plasma Kinetic Theory. McGraw-Hill

Motch C., Harberl F., Guillout P., Pakull M., Reinsch K., Krauter J., 1996, A&A, 307, 459

Mukai K., 1988, MNRAS, 232, 175

Mukai K., 1999, private communication, see also

   http://lheawww.gsfc.nasa.gov/users/mukai/iphome/issues/heii.html

O'Donoghue D., 1999, private communication

O'Donoghue D., Mason K., Chen A., Hassall B., Watson G., 1993, MNRAS, 265, 545

O'Donoghue D., Smit J., 1999, private communication

Osborne J., Beardmore A., Wheatley P., Hakala P., Watson M., K.O. Mason B. H., King A., 1994, MNRAS, 270, 650

Pasquini L., Belloni T., Abbot T., 1994, A&A, 290, L17

Patterson J., 1994, PASP, 106, 209

Piirola V., Hakala P., Coyne G., 1993, ApJ, 410, L107

Ramaty R., 1969, ApJ, 158, 753

Reinsch K., Burwitz V., Beuermann K., Schwope A., Thomas H.-C., 1994, A&A, 291, L27

Rodrigues C., Cieslinski D., Stiener J., 1998, A&A, 335, 979

Rosen S., Mason K., Cordova F., 1987, MNRAS, 224, 987

Russ J., 1992, Image Processing Handbook. Ann Arbor:CRR Press

Schmidt G.-D., Stockman H., Margon B., 1981, ApJ, 243, L157

Schneider D., Young P., 1980a, ApJ, 240, 871

Schneider D., Young P., 1980b, ApJ, 238, 946

Schwartz R. et al., 1998, ApJ, 338, 465

Schwope A., 1995, Rev. Mod. Ast., 8, 125

Schwope A., Beuermann K., 1997, Astron. Nachr., 318, 111

Schwope A., Beuermann K., Jordan S., 1995, A&A, 301, 447

Schwope A., Beuermann K., Thomas H.-C., 1990, A&A, 230, 120

Schwope A., Catalan M., Beuermann K., Metzner A., Smith R., Steeghs D., 2000, MN-RAS, 313, 533

Schwope A., Mantel K.-H., Horne K., 1997, A&A, 319, 849

Schwope A., Schwarz R., Greiner J., 1999, A&A, 348, 861

Schwope A., Schwarz R., Staude A., Heerlien C., Horne K., Steeghs D., 1998. in Hellier C., Mukai K. ed, Annapolis workshop on magnetic cataclysmic variables, A.S.P. Conf. Ser. 157, p. 71

Schwope A., Thomas H.-C., Beuermann K., 1993, A&A, 271, L25

Schwope A., Thomas H.-C., Beuermann K., Burwitz V., Jordan S., Haefner R., 1995, ApJ, 293, 746

Shafter A., Reinsch K., Beuermann K., Misselt K., Buckley D., Burwitz V., Schwope A., 1995a, ApJ, 443, 319

Shafter A., Reinsch K., Beuermann K., Misselt K., Buckley D., Burwitz V., Schwope A., 1995b. in Buckley D.A.H., Warner B. ed, Cape workshop on magnetic cataclysmic variables, A.S.P. Conf. Ser. 85, p. 269

Shi-hui Y., 1994, Astrophysics and Space Library, Vol. 198, Magnetic Fields of Celestial Bodies. Kluwer Academic Publishers

Silber A., 1992, Ph.D. thesis, MIT

Stobie R., Okeke P., Buckley D., O'Donoghue D., 1997, MNRAS, 283, L127

Tamor S., 1978, Nucl. Fusion, 18, 229

Tapia S., 1977, Int. Astr. Union Cir, no. 3054

Thomas H.-C., Beuermann K., Burwitz V., Reinsch K., Schwope A., 1999, A&A, submitted

Thomas H.-C., Reinsch K., 1996, A&A, 315, L1

Visvanathan N., Wickramasinghe D., 1979, Nature, 281, 47

Warner B., 1995, Cataclysmic Variables Stars. Cambridge University Press

West S., Berriman G., Schmidt G., 1987, ApJ, 322, L35

Wickramasighe D., Ferrario L., Bailey J., 1989, ApJ, 342, L35

Wickramasinghe D., 1988. in Coyne G.V. *et al* ed., Polarized Radiation of Circumstellar Origin, Vatican Observatory, p. 199

Wickramasinghe D., Ferrario L., 1988, ApJ, 334, 412

Wickramasinghe D., Meggit S., 1982, MNRAS, 198, 975

Wickramasinghe D., Visvanathan N., Tuohy I., 1984, ApJ, 286, 328

Wu K., Wickramasinghe D., 1993, MNRAS, 260, 141